Retrospective Theses and Dissertations

Iowa State University Capstones, Theses and Dissertations

2002

Edge based finite element simulation of eddy current phenomenon and its application to defect characterization

Yue Li
Iowa State University

Follow this and additional works at: https://lib.dr.iastate.edu/rtd

Part of the Electrical and Electronics Commons

INFORMATION TO USERS

This manuscript has been reproduced from the microfilm master. UMI films the text directly from the original or copy submitted. Thus, some thesis and dissertation copies are in typewriter face, while others may be from any type of computer printer.

The quality of this reproduction is dependent upon the quality of the copy submitted. Broken or indistinct print, colored or poor quality illustrations and photographs, print bleedthrough, substandard margins, and improper alignment can adversely affect reproduction.

In the unlikely event that the author did not send UMI a complete manuscript and there are missing pages, these will be noted. Also, if unauthorized copyright material had to be removed, a note will indicate the deletion.

Oversize materials (e.g., maps, drawings, charts) are reproduced by sectioning the original, beginning at the upper left-hand corner and continuing from left to right in equal sections with small overlaps.

Edge based finite element simulation of eddy current phenomenon and its application to defect characterization

by

Yue Li

A dissertation submitted to the graduate faculty

in partial fulfillment of the requirements for the degree of

DOCTOR OF PHILOSOPHY

Major: Electrical Engineering (Electromagnetics)

Program of Study Committee:
Satish Udpa, Major Professor
Lalita Udpa
Balasubramaniam Shanker
William Meeker
Joseph Gray
Yushi Sun

Iowa State University

Ames, Iowa

2002

Graduate College
Iowa State University

This is to certify that the doctoral dissertation of

Yue Li

has met the dissertation requirements of Iowa State University

Signature was redacted for privacy.

Major Professor

Signature was redacted for privacy.

For the Major Program

TABLE OF CONTENTS

LIST OF FIGURES

LIST OF TABLES

ABSTRACT

Edge based finite elements are finite elements whose degrees of freedom are assigned to edges of finite elements rather than nodes. Compared with conventional node based counterparts, they offer many useful properties. For example, they enforce tangential continuity only on inter-element boundaries but no normal continuity; they allow a vector field separated as the sum of the gradient of a scalar function and the remaining part. This dissertation presents a magnetic vector potential formulation implemented with edge elements to simulate eddy current phenomenon. The additional degree of freedom associated with the magnetic vector potential is fixed with the help of tree and co-tree separation from graph theory. The validity of the method is verified using well-known benchmark problems.

A phenomenological signal inversion scheme is proposed to characterize defect profiles from eddy current probe signals The method relies on the edge element based forward model to predict probe responses and a minimization algorithm to minimize an objective function representing the squared error between the modal prediction and the observed signal. A gradient-based minimization algorithm is first investigated. The long computation time associated with the gradient calculation is reduced using the adjoint equation based method. However, gradient-based methods tend to converge to a poorer local minimum. A genetic algorithm and a simulated annealing algorithm are employed to improve performance. The performance of these stochastic methods in the context of the defect characterization problem is studied. The preliminary results show the effectiveness of the stochastic methods.

CHAPTER 1 INTRODUCTION

1.1 NDT/NDE Techniques

NDT/NDE techniques are widely used in a number of industrial areas to control product quality, prevent catastrophic failure, improve reliability and regulate manufacturing processes. NDT/NDE plays a crucial role in everyday life, because it is necessary to assure safety and reliability. Components and structures that are typically inspected include aircraft, gas pipeline, bridge, power plant, etc.

The American Society for Nondestructive Testing (ASNT) defines Nondestructive testing (NDT) as the examination of an object or material with technology that does not affect its future usefulness. Thus, NDT can be used without destroying or damaging a product or material. Since it allows inspection without interfering with a product's final use, NDT provides an excellent balance between quality control and cost-effectiveness. The term Nondestructive evaluation (NDE) usually connotes a more quantitative aspect of the subject. For example, NDE techniques are used not only to detect the presence of a flaw or defect, but also to determine the location, size, or even shape of the defect. NDE may also be used to characterize material properties. Since the terms NDT and NDE are so close to each other, these two terms are used interchangeably in this dissertation unless otherwise stated.

NDT techniques usually involve the introduction of some form of physical energy, such as X-rays, ultrasonic waves, or electromagnetic fields, into the test specimen. The nature of the interaction between the energy and the test specimen is a function of several variables including the type of the energy, material properties, defects and inhomogeneities in the material and so on. The interaction is then sampled through a transducer and the

response of the transducer is analyzed to characterize the material properties of the specimen. Common NDT techniques include radiography testing (RT), ultrasonic testing (UT), electromagnetic testing (ET), and acoustic emission testing (AE) etc [1]. Specific NDT methods that can be used in an application depend on the physical properties of the material and the nature of the information being sought. A thorough knowledge of each NDT technique is required to ensure the correct selection of the appropriate method for a given application. This dissertation is limited to a description and treatment of eddy current methods only.

1.2 Eddy Current Testing

Eddy current testing (ECT) is an electromagnetic technique that can only be used for testing conducting materials. It originates from Michael Faraday's discovery of electromagnetic induction in 1831. According to Faraday's law, a time varying magnetic field induces an electromotive force in a conducting material. Even though the force is very weak, large currents flow inside the metal when the metal has a high conductivity. The induced currents tend to flow in loops, called eddy currents. Eddy currents generate a time varying magnetic field in turn and the generated magnetic field interacts with the original field. To distinguish between them, the original time varying magnetic field is termed the primary field while the magnetic field established by the induced current is often termed the secondary field. The direction of eddy currents depends on the direction of the time varying primary field. According to Lenz's law, the secondary field generated by eddy currents opposes the primary magnetic field changes.

The eddy current phenomenon is easily observed when a coil carrying an AC current is brought in proximity to the surface of a metal specimen, as shown in Figure 1.1. The time varying magnetic field established by the coil causes circulating eddy currents in the metal. The direction of the induced eddy currents is opposite to the current flow in the coil in accordance with Lenz's law. The secondary magnetic field induced by eddy currents interacts with the primary field and thus alters the impedance of the coil. Changes in the material properties of the metal cause changes in the magnitude and phase of the induced eddy currents and hence the coil impedance. As an example, assume that there is a crack in the surface of the metal underneath the coil. The crack interrupts the eddy current flow, thus decreasing the loading of the coil and increasing its effective impedance. By measuring the impedance of the coil, we can detect changes in the material property. This is the basis of eddy current testing.

Eddy currents are affected by factors depending on the test specimen and experimental conditions. Specimen dependent factors include its electrical conductivity, magnetic permeability, thickness, material property discontinuities etc. Experimental factors that affect the response include the shape and size of the excitation coil, operating frequency, and proximity of the coil to the specimen or lift-off.

An important issue that must be taken into account in eddy current testing is the depth of penetration. The eddy current density is greatest on the surface of the conducting specimen and decays with depth as shown in Fig 1.2. This phenomenon is described by the standard depth of penetration or skin depth, at which the eddy current density reduces to 36.8% of its surface value. For a plane wave on a planar surface, the standard depth of penetration is given by the formula [2][3]
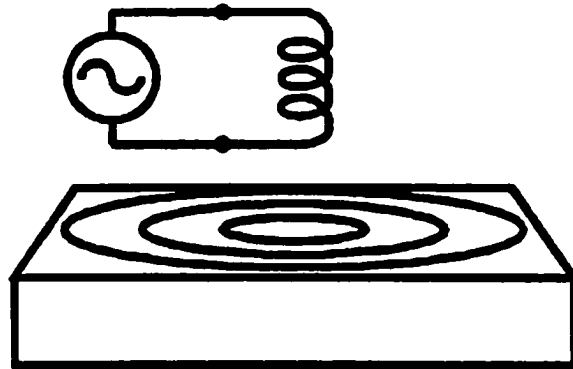
Fig 1.1 An alternating current bearing coil over a block of metal
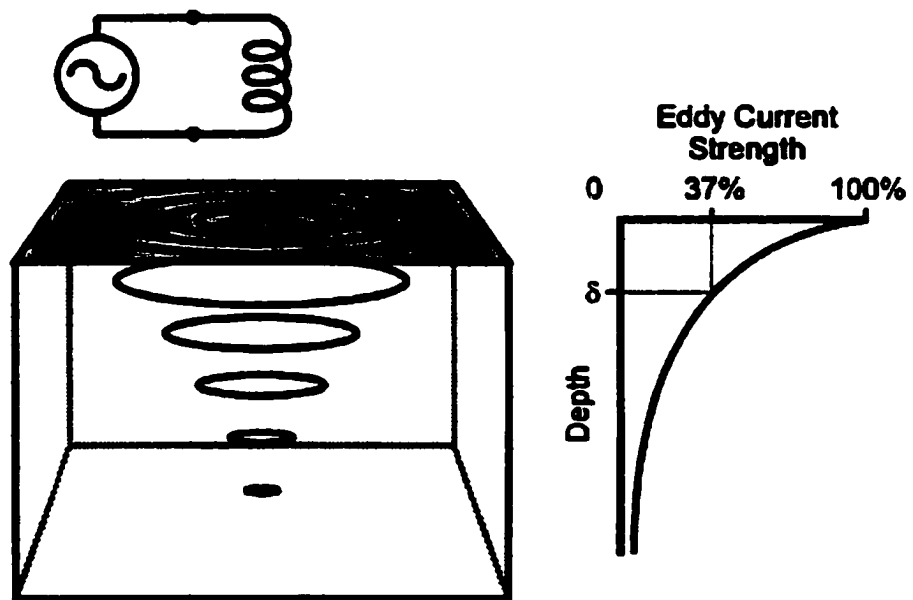
Fig 1.2 The skin depth effect of eddy currents

$$\delta = \sqrt{\frac{1}{\pi f \mu \sigma}}$$

From this it can be seen that the skin depth δ decreases with an increase in the operating

frequency f , conductivity σ and permeability μ. Defects located beyond the skin depth

have very little effect on the eddy current and its magnetic field. Because of the skin effect

phenomenon, eddy current testing is limited to detecting surface or subsurface flaws and

corrosion.

The eddy current phenomenon is described using Maxwell's equations

mathematically. By solving the Maxwell's equations, we can determine the magnitude and

phase of eddy currents, the distribution of magnetic fields and coil impedances. The solution

methods generally fall into two categories: analytical methods and numerical methods. The

analytical analysis of eddy currents can be found in the works of Lameraner and Stall [4];

Stoli [5]; Tegopoulos and Kriezis [6]. However, analytical solutions are usually limited to

geometries possessing some forms of symmetry. Their usefulness is, therefore, very limited

in practice. A significant amount of effort has been devoted to the development of numerical

solution methods since the advent of computers. Various numerical techniques, such as

finite difference method (FDM), finite element method (FEM), and boundary element

method (BEM) have achieved great success in solving electromagnetic problems. The FDM

was of great use in the early age of computers. Stoll [5], Muller [7], Wiak and Zakrzewski

[8] applied FDM to eddy current problems and extended the life of FDM to 1980s. Due to

the lack of flexibility in dealing with irregular geometries, the popularity of FDM has

declined in the last few decades. Since 1970s, FEM has dominated the numerical modeling

of eddy current problems. Chari [9], Carpenter [10], Silvester and Ferrari [11] are among the

earliest to apply FEM techniques to eddy current modeling. Numerous papers have been

published since then. The names of researchers in this area should be supplemented by

Bossavit and Verite [12], Salon and Peng [13], Preston and Reece [14], Rodger, Leonard,

Eastham [15,16], Trowbridge [17], Simkin [17,18], Emson [18], Biro [19], Ren [20,21],

Wong and Cendes [22,23], Albanese and Rubinacci [24], Kameari [25,26], Nakata [27,28],

and many others. Besides FEM, the BEM has also gained great importance and much

attention since 1970's. References concerning BEM and eddy currents can be found in the

works of Salon and Schneider [29], Kost [30], Rucker and Richter [31], Tsuboi and Misaki

[32], and so on. The main advantage of the BEM is that the dimension of a problem can be

reduced from three to two for a 3-D problem or from two to one for a 2-D problem. The

disadvantage is that, unlike the FEM, the resulting matrices are full and usually

nonsymmetrical. The FEM and BEM are often combined to form a hybrid formulation,

which greatly reduces the computation effort [12,33].

Among the numerical techniques, the FEM appears to be the most popular one for

eddy current computations [34]. The FEM has evolved from structural analysis. Its basic

ideas date back to 1940's and can be found in the works of Hrenikoff [35], Courant [36],

McHenry [37], and Levy [38]. The phrase "finite elements" was the contribution of Clough

[39] in 1960. The basic idea is to divide the solution domain into large numbers of small

regions, called finite elements, and interpolate the unknown field with a set of predefined

linearly independent basis functions. Then, an approximation of the unknown field is

expressed by a set of interpolation coefficients. These coefficients are obtained by solving a

linear system through the finite element formulation. The finite element method has become

an important and powerful analysis tool for addressing eddy current problems. It is also

widely used in such diverse areas as mechanical structure analysis, fluid mechanics, heat flow, and other areas of computational electromagnetics.

Much work has been done in studying eddy current testing techniques both qualitatively and quantitatively. Detailed analysis of the underlying theories of eddy current testing can be found in the works of Burrows [40], Dodd and Deeds [41], Lord and Palanisamy [42]. The application of FEM in the study of eddy current NDT was pioneered by the work of Palanisamy and Lord [43,44], Nehl and Demerdash [45]. FEM and other numerical techniques made the quantitative studies of eddy current NDT in practical applications possible. Now eddy current methods are widely used particularly in the aircraft and nuclear industry. They are employed for detecting surface and subsurface cracks and corrosion in aircraft structure, jet engine disks, turbine rotor blades and so on.

1.3 Forward and Inverse Problems

Two kinds of problems are of interest in NDE applications. These problems are referred to as the forward problem and the inverse problem. The forward problem deals with the prediction of a transducer's response given an excitation source and the material properties of the test specimen. In contrast, inverse problems are concerned with the estimation of the material properties of the specimen based on the measured transducer responses. All NDE problems in reality are inverse in nature, but a good forward model helps, among other things, in understanding the underlying physics and improving the system design. The forward problem in eddy current NDE involves, in essence, the solution of Maxwell's equations. Both analytical methods and a variety of numerical techniques can be used to address the forward problem.

Rapid developments in computing facilities and technology have also made model based inverse problem solution methods attractive to scientists and engineers. Many inverse problem methodologies have been developed and applied to solve real life problems. In eddy current NDE applications, the inverse problem is related to the task of characterizing the size, shape and location of defects based on the information contained in coil impedance signals. Most of the approaches in industry use a combination of signal processing and pattern recognition methods to establish a relationship between a set of parameters characterizing defects and specific features of the signals. Artificial neural networks (ANN) are used widely to determine the relationship [46-52]. An ANN can be viewed as a mapping from an input vector to an output vector. The mapping may be highly nonlinear and is determined by weights in the network. An ANN learns the desired mapping through given data patterns (input-output pairs), which may come from actual measurements or the solution of the corresponding forward problem. Fig 1.3 shows a typical ANN. In eddy current signal inversion, the input to the network is the eddy current probe signal and the output is the set of defect parameters. An FEM forward model can be used to generate the signal patterns for training the network. This allows the exploitation of the analytical capability of the FEM and the mapping capability of the ANN. An ANN builds a functional relationship between the input and output data sets. However, the underlying physics of the real problem is ignored by the network. In Fig 1.3, the input-output data patterns may be eddy current signals, ultrasonic signals or something else. The ANN is blind to the input source and is merely capable of extracting a relationship between the input and output signals. The approach is therefore purely non-phenomenological in nature. It requires large amount of training data, which is not always available in practical applications. Applications of non-

phenomenological methods in NDE signal inversion can be found in the works of Hoole [46], Udpa et al [47], Badics et al. [48], Popa and Miya [49], Sikora et al. [50], Rubinacci et al. [51], Ioan and Duca [52], and so on.

Unlike non-phenomenological approaches, phenomenological or model-based approaches embed the underlying physics into the signal inversion process. Such an approach usually involves a forward model and an error minimization algorithm. Fig 1.4 shows a typical scheme for characterizing defect profiles from measured NDE signals. The model takes a set of measured signals as input. It begins with an initial guess of the desired defect profile or a set of potential profiles. A forward model is employed to simulate the physical process and predict the response of the NDE system. An objective function is defined to describe the difference between the predicted signal and the measured signal. By iteratively updating the defect profile, a minimum value of the objective function, may be reached. A lot of methods may be used in minimizing the objective function. The minimization approaches can be generally cast into two categories: the deterministic approach and the stochastic approach. Popular examples of the deterministic approach include the conjugate gradient and quasi-Newton methods. These methods require the evaluation of the gradient as well as the value of the objective function. When multiple parameters are involved, the computation effort associated with the gradient computation can be very high. Typical stochastic approaches are the simulated annealing method and genetic algorithms. These methods do not require the gradient information as prior information. A major difference between the two kinds of methods is that the behavior of the deterministic approach highly depends on the local property of the function being minimized. It tends to converge to a poorer local minimum and produce a result that depends on the initial trial
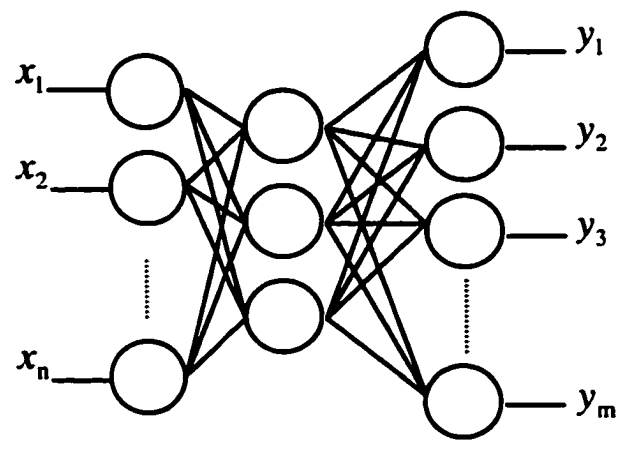
Fig 1.3 An artificial neural network
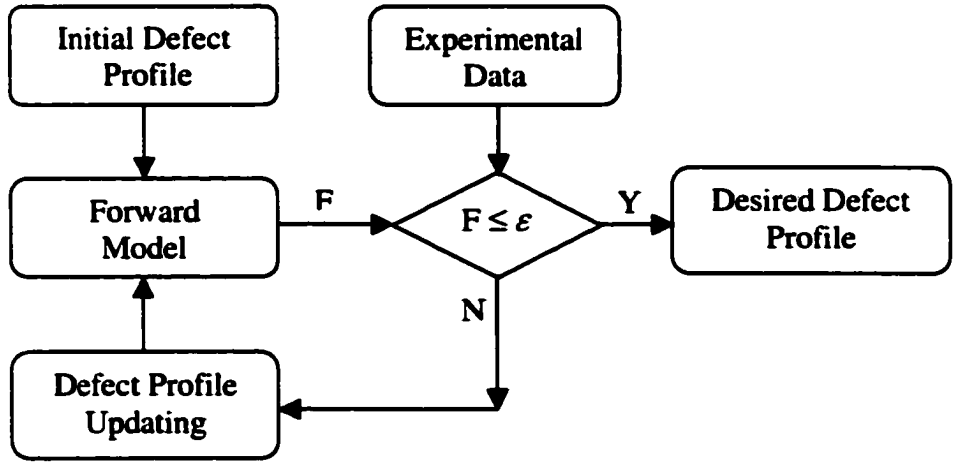
Fig 1.4 An iterative signal inversion scheme

solution. So, such kind of method is also termed a local technique. On the contrary, a stochastic optimization method does not rely on the local property of the function being optimized and its result does not depend on the starting point. It even works well for nondifferentiable or discontinuous functions. Such a global technique is especially useful in finding a global minimum among numerous poorer local minima. Applications of phenomenological methods to NDE signal inversion can be found in the works of Oristaglio and Worthington [53], Salon and Istfan [54], Hoole et al. [55], Norton and Bowler [56,57], Neittaanmaki et al. [58], Udpa [59,60], Albanese and Rubinacci [61], and so on.

1.4 Objectives of This Research

Conventional node-based finite element methods are intrinsically suitable for analyzing scalar fields. When applying them to electromagnetic field computations, the unknown vector field, such as electric field intensity, magnetic flux density or magnetic vector potential, has to be decomposed into its three Cartesian components. Due to the very nature of nodal interpolation, all three components of the vector field are continuous across element boundaries. When dealing with material interfaces, it violates the boundary conditions in electromagnetics, which enforces the continuity of either tangential or normal components. To relax the continuity requirements of node based finite elements, the edge based finite element method was proposed. Instead of assigning degrees of freedom to element nodes, edges are used to interpolate the unknown vector field. The basis functions associated with edges are vector functions. Thus edge elements are vector oriented. In addition to the relaxed continuity requirement, edge elements offer many other useful properties [62]. They have been widely accepted by many researchers in the computational

electromagnetics community [24]. In this research, an edge-based finite element forward

model is developed and its effectiveness is verified with a well-known benchmark problem.

The model is employed to simulate the eddy current phenomenon and predict the eddy

current testing signals obtained in the nondestructive inspection of heat exchanger tubes.

The edge based finite element forward model is then embedded in a model based

NDE signal inversion scheme. Both the gradient search approach and stochastic approaches

are investigated for characterizing defect profiles from eddy current signals. The main

difficulty in applying a gradient based minimization algorithm to signal inversion lies in the

fact that the method for gradient computation calls for solving the governing linear system

once for each of the partial derivatives. This makes the computation time prohibitively long

in multi-dimensional minimization. An adjoint equation based method is used to address the

problem [56,64]. By introducing a set of Lagrangian multipliers, all the derivatives required

by the minimization algorithm could be found by solving the linear system only once, no

matter how many parameters are involved. This significantly reduces the computation time.

However, the gradient search method is a local technique. It produces a solution that

depends highly on the initial staring point. In order to avoid some of these problems,

stochastic methods are used to find a global minimum of the objective function. A simulated

annealing and a genetic algorithm are used in characterizing defects in heat exchanger tubes.

The stochastic algorithms do not require the gradient of the objective function to work, but

the function itself has to be evaluated repeatedly. They usually have a heavier computation

burden than gradient search methods. A comparison of performance of the gradient search

and stochastic methods for NDE signal inversion is presented.

1.5 Literature Review

Numerous papers have been published on eddy current flaw detection. Space considerations preclude a full review of all related work here. Only those that are closely related to this research are reviewed in this section.

This research employs an edge based finite element model to simulate the eddy current NDT phenomenon. Edge elements were first proposed in 1980 by Nedlec [65] and have been gradually accepted by the computational electromagnetics community [24]. Bossavit [66] provides a justification for the use of edge elements in electromagnetic field computations. Webb [62] discusses the basic properties of edge elements and their advantages over node based counterparts. Kameari [67] presents an implementation of edge elements based on $\bar{A}$-V and $\bar{A}$-V-Ψ formulation. The equivalence of the two formulations to $\bar{A}$ formulation implemented with edge elements is shown. The problem of uniqueness is overcome with the help of tree and co-tree separation from graph theory. The same gauge method is also used in Albanese and Rubinacci's work [68,69].

Neittaanmaki et al [58] gives a comprehensive review of inverse solution methods and presents several examples of their use in electromagnetic component design. The text covers several topics relating to the computer implementation of these algorithms. Since all inverse problems are ill-posed in nature, regularization schemes, necessary to ensure the existence, uniqueness and stability of the solution, are introduced. Isakov [70] also discusses the uniqueness and stability issues encountered in solving inverse problems.

Oristaglio and Worthington [53], and Hoole et al [55] were among the earliest to propose inverse methods using a numerical forward model and an error minimization algorithm. Oristaglio and Worthington solve a 2D inverse problem using an optimization

tool based on gradient information in combination with a FEM forward model. Hoole introduces an inverse problem method for the identification of cracks, sources, materials, and their geometry in inaccessible locations through the geometric differentiation of finite element matrices. A general approach, which employs a finite element forward model and a gradient based minimization algorithm, is presented. Two problems are reported. First, multiple minima are possible with the objective function. Second, they show an over described crack may result in nonconvergence of the minimization algorithms.

Numerous approaches to defect characterization have been proposed in recent years. Yan et al [59] applies the signal inversion scheme shown in Fig 1.4 to 2-D defect characterization problems involving analysis of magnetic flux leakage signals. Ng [63] and Liu et al [60] extend the method to eddy current signal inversion. A $\bar{A}$ formulation node based finite element model and a conjugate gradient minimization algorithm are employed. The method is applied for predicting the defect profiles in heat exchanger tubes. The defect profile is described as a 8-node quadrilateral element. An axisymmetric geometry is assumed and a finite difference approximation is used to calculate the gradient of the objective function. This approach consumes significant computation resources for calculating gradients and suffers from problems due to round off errors. Albanese et al [61] propose a model for characterizing crack shapes using an integral computation model implemented with edge elements. A genetic algorithm is employed to minimize the error function. In this model, the crack shape is described as a binary bitmap, i.e. element facets within the defect zone either belong to the crack or not. Kojima et al [71] and Fukutomi et al [72] use the trust region method to determine crack shapes. The crack shape is represented as a spline function.

1.6 Scope of The Dissertation

This dissertation presents a thorough discussion, from theory to computational

aspects, on the numerical simulation of eddy current problems based on magnetic vector

potential formulation, implemented with edge based finite elements. This dissertation also

investigates the application of gradient based minimization methods and stochastic

minimization algorithms to eddy current NDE signal inversion.

The dissertation consists of 7 chapters. The first three chapters introduce the

necessary theoretical background. Chapter 1 introduces the background relating to eddy

current testing and simulation. Chapter 2 gives a brief review on basic electromagnetic

theory. Only topics that are closely related to eddy current computation are included.

Chapter 3 introduces conventional node based finite elements. Topics include various

aspects of the implementation of a typical finite element analysis, such as common finite

element types, basis functions, Galerkin's approach and weak form, assembly, and linear

solvers. Chapter 4 to 6 covers the main topics of the dissertation work. Chapter 4 deals with

the implementation of $\bar{A}$ formulation using edge based finite elements. A gauge condition

based on tree and co-tree separation is introduced to fix the arbitrariness associated with $\bar{A}$.

The model is verified with both magnetostatic and eddy current problems. Chapter 5

introduces a gradient based approach for eddy current NDE signal inversion. An adjoint

equation based method is presented to evaluate the gradient of the objective function. The

limitation of the gradient search methods is also discussed. Chapter 6 presents stochastic

methods to find a "near" global minimum of the objective function. A genetic algorithm and

a simulated annealing algorithm are discussed. Chapter 7 contains concluding remarks and

discusses future work.

CHAPTER 2 BASIC ELECTROMAGNETICS FOR EDDY CURRENT COMPUTATION

2.1 Introduction

This chapter begins with a brief review of Maxwell's equations and related topics,

and then discusses three formulations for eddy current computations. Only those topics that

are closely related to this research are included. For a more detailed introduction on

electromagnetic theory, interested readers may refer to [2] and [3].

2.2 Maxwell's Equations

The variables that are used to describe electromagnetic fields are the following five

vectors and one scalar:

$\bar{E}$ electric field intensity (volt/meter)

$\bar{H}$ magnetic field intensity (ampere/meter)

$\bar{D}$ electric flux density (coulomb/meter^3)

$\bar{B}$ magnetic flux density (tesla)

$\bar{J}$ electric current density (ampere/meter^2)

ρ electric charge density (coulomb/metre^3)

These variables may be both functions of space coordinates x, y, z and time t. They are

related by the well-known Maxwell's equations, which are the basis of electromagnetic

theory. The differential form is expressed as follows:

$$\nabla \times \bar{E} = -\frac{\partial \bar{B}}{\partial t} \tag{2.1}$$

$$\nabla \times \bar{H} = \bar{J} + \frac{\partial \bar{D}}{\partial t} \tag{2.2}$$

$$\nabla \cdot \bar{D} = \rho \tag{2.3}$$

$$\nabla \cdot \bar{B} = 0 \tag{2.4}$$

An important equation, the continuity equation, is derived from equations (2.2) and (2.3),

$$\nabla \cdot \bar{J} + \frac{\partial \rho}{\partial t} = 0 \tag{2.5}$$

It says the net flow of electric current out of a small volume equals the time rate of decrease in electric charges.

2.3 Constitutive Relations

The following constitutive relations describing the material properties of a medium are usually added to the Maxwell's equations,

$$\bar{D} = \varepsilon \bar{E} \tag{2.6}$$

$$\bar{B} = \mu \bar{H} \tag{2.7}$$

$$\bar{J} = \sigma \bar{E} \tag{2.8}$$

where ε (farads/meter) is the electric permittivity of a medium, μ (henries/meter) is the magnetic permeability and σ (siemens/meter) is the electrical conductivity. The above constitutive relations apply to isotropic, linear and nondispersive materials. In the general case, a material may be both anisotropic and nonlinear. These property parameters should be tensors, expressed as matrices mathematically and their values depend on the field values. In this report, we consider isotropic and linear materials only. The hysteresis of ferromagnetic material is also ignored. Consequently, the three parameters are considered as scalar constants for a particular material.

2.4 Boundary Conditions

The Maxwell's equations should be satisfied everywhere in space, including the interface joining different materials. Applying equations (2.1) – (2.4) to the material interface shown in Fig 2.1 gives the boundary conditions: equations (2.9)-(2.12),
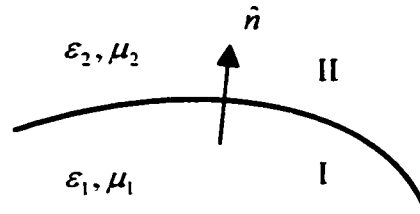
Fig 2.1 A boundary between two materials

$$\left(\bar{E}_{II} - \bar{E}_{I}\right) \times \hat{n} = 0 \qquad (2.9)$$

$$\left(\bar{H}_{II} - \bar{H}_{I}\right) \times \hat{n} = \bar{J}_{s} \qquad (2.10)$$

$$\left(\bar{B}_{II} - \bar{B}_{I}\right) \cdot \hat{n} = 0 \qquad (2.11)$$

$$\left(\bar{D}_{II} - \bar{D}_{I}\right) \cdot \hat{n} = \rho_{s} \qquad (2.12)$$

where $\hat{n}$ is defined as the unit vector normal to the interface and pointing from medium I to medium II. This implies that only the tangential component of the electric field intensity $\bar{E}$ and the normal component of the magnetic flux density $\bar{B}$ are always continuous on inter-material boundaries. The discontinuity of the tangential component of $\bar{H}$ and the normal component of $\bar{D}$ are characterized by the surface current $\bar{J}_s$ and the surface charge ρ_s.

2.5 Time-Harmonic Fields

Time-harmonic analysis plays an important role in various engineering applications. A time-harmonic quantity refers to a variable which varies sinusoidally with time. In the case that we are interested in the steady state reached when a system is excited sinusoidally, the variables describing the system can be considered as time-harmonic quantities. A time-harmonic quantity can be expressed in exponential form

$$\bar{E}(t) = \bar{E}_p \exp(j\omega t).$$

Then, the partial differential operator $\partial/\partial t$ acting on a time-harmonic quantity is simply $j\omega$. So, for time-harmonic fields, the Maxwell-Faraday's law (2.1) and Maxwell-Ampere's law (2.2) become

$$\nabla \times \bar{E} = -j\omega \bar{B} \qquad (2.13)$$
$$\nabla \times \bar{H} = \bar{J} + j\omega \bar{D} \qquad (2.14)$$

In this way, a time domain problem can be considered in the frequency domain.

2.6 Quasistatic Approximation

As can be seen from equations (2.2) or (2.14), there exist two kinds of currents: conduction current and displacement current. The conduction current is proportional to the electric field intensity, as stated by Ohm's law,

$$\bar{J} = \sigma \bar{E} \qquad (2.15)$$

The displacement current is defined as the time varying rate of electric flux density.

$$\bar{J}_d = \frac{\partial \bar{D}}{\partial t} = j\omega \varepsilon \bar{E} \qquad (2.16)$$

In many circumstances, the time varying rate is low enough such that $\sigma \gg \omega\varepsilon$. In such a case, the displacement current can be neglected and the quasistatic approximation is said to apply to the Maxwell-Ampere's law, i.e.

$$\nabla \times \bar{H} = \bar{J} \tag{2.17}$$

This equation implies (see equation (2.20))

$$\nabla \cdot \bar{J} = 0 \tag{2.18}$$

Consequently, in steady state, electric current density is divergence free, since there is no accumulation of net charges.

2.7 Potential Functions

The Maxwell's equations consist of a group of four equations coupled by multiple variables. It can be very difficult to deal with. Potential functions are usually introduced to reduce the number of equations and variables. The following two vector identities are often used to define the potential functions.

$$\nabla \times \nabla V \equiv 0 \tag{2.19}$$
$$\nabla \cdot \nabla \times \bar{A} \equiv 0 \tag{2.20}$$

They states that the gradient of an arbitrary scalar function is irrotational and the curl of an arbitrary vector function is solenoidal provided these functions are sufficiently differentiable.

Magnetic Vector Potential. From equation (2.4) and (2.20), the magnetic flux density $\bar{B}$ can be expressed as the curl of a vector function.

$$\bar{B} = \nabla \times \bar{A} \tag{2.21}$$

The vector function $\bar{A}$ is termed the magnetic vector potential.

Electric Scalar Potential. Substituting equation (2.21) into (2.1) results in the following equation:

$$\nabla \times \left(\bar{E} + \frac{\partial \bar{A}}{\partial t} \right) = 0$$

Invoking equation (2.19), the electric field intensity can be expressed as follows:

$$\bar{E} = -\frac{\partial \bar{A}}{\partial t} - \nabla V \tag{2.22}$$

where V is an scalar function, termed the electric scalar potential.

Electric Vector Potential. In a truly steady state case, $\nabla \cdot \bar{J} = 0$ (see section 2.6). A potential function $\bar{T}$, therefore, can be introduced to represent current density.

$$\bar{J} = \nabla \times \bar{T} \tag{2.23}$$

$\bar{T}$ is termed the electric vector potential.

Magnetic Scalar Potential. Consider equation (2.17). In a current free region, the magnetic field intensity $\bar{H}$ becomes curl free. Thus, a scalar function can be used to represent $\bar{H}$.

$$\bar{H} = -\nabla \Phi \tag{2.24}$$

Φ is termed the magnetic scalar potential.

Except the electric scalar potential, all other three potential functions do not possess any physical sense. They are introduced just to facilitate the analysis of electromagnetic fields.

2.8 Eddy Current Formulations

In eddy current problems, the time fluctuation rate is low enough for the quasistatic condition to apply. Figure 2.2 shows a typical configuration of eddy current problems. The solution domain Ω is divided into a conducting region Ω_1 and a nonconducting region Ω_2, which may include the excitation current source J_s.

Invoking equations (2.15) and (2.22), equation (2.17) becomes

$$\nabla \times \frac{1}{\mu} \nabla \times \bar{A} + \sigma \frac{\partial \bar{A}}{\partial t} + \sigma \nabla V = 0 \qquad \text{in} \Omega_1 \qquad (2.25)$$

$$\nabla \times \frac{1}{\mu} \nabla \times \bar{A} = \bar{J}_s \qquad \text{in} \Omega_2 \qquad (2.26)$$

Then an eddy current problem is described by the magnetic vector potential and electric scalar potential through the above two equations. Equation (2.21) specifies the curl of the magnetic vector potential as the magnetic flux density. Helmholtz theorem states that a vector field is uniquely determined only if both its curl and divergence are specified. Therefore, the divergence of the magnetic vector potential must be specified to fix the additional degrees of freedom associated with $\bar{A}$. This value may be specified freely without affecting the physical problem. In many circumstances, the divergence free condition is often imposed, i.e.

$$\nabla \cdot \bar{A} = 0 \qquad (2.27)$$

This is the well-known Coulomb gauge. Interested readers may refer to [73] for other forms of gauge conditions, such as the diffusion gauge and Lorentz gauge.

Suppose the magnetic permeability is piecewise constant. Using the following vector identity
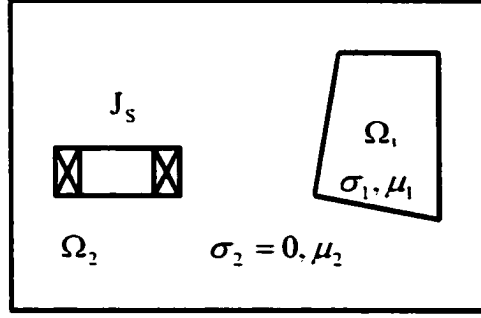
Fig 2.2 A configuration for eddy current problems

$$\nabla \times \nabla \times \bar{A} = \nabla(\nabla \cdot \bar{A}) - \nabla^2 \bar{A} \tag{2.28}$$

and the Coulomb gauge, equations (2.25) and (2.26) reduce to,

$$-\nabla^2 \bar{A} + \sigma \frac{\partial \bar{A}}{\partial t} + \sigma \nabla V = 0 \qquad \text{in} \, \Omega_1 \tag{2.29}$$

$$-\nabla^2 \bar{A} = \bar{J}_s \qquad \text{in} \, \Omega_2 \tag{2.30}$$

where ∇^2 is the vector Laplacian operator

$$\nabla^2 \bar{A} = \hat{x} \nabla^2 A_x + \hat{y} \nabla^2 A_y + \hat{z} \nabla^2 A_z$$

$\bar{A}$-V **Formulation.** In $\bar{A}$-V formulation, the magnetic vector potential $\bar{A}$ and

electric scalar potential V are used to represent the electromagnetic field in the conducting

region Ω_1. while in the nonconducting region Ω_2, only $\bar{A}$ is used. It is also called $\bar{A}$-V-$\bar{A}$

formulation in literature [17]. The eddy current density is expressed as

$$\bar{J} = -\sigma \left(\frac{\partial \bar{A}}{\partial t} + \nabla V \right)$$

In equation (2.25), the divergence free condition of the eddy current density (see section 2.6)

is automatically satisfied. However introducing Coulomb gauge in equation (2.29) violates

the condition. It must, therefore, be enforced explicitly. Thus,

$$\nabla \cdot \sigma \left(\frac{\partial \bar{A}}{\partial t} + \nabla V \right) = 0 \qquad \text{in } \Omega_1 \qquad (2.31)$$

Interface conditions must also be enforced at the interface Γ_{12} between Ω_1 and Ω_2. since eddy currents are restricted in conducting region only, at the interface Γ_{12},

$$\bar{J} \cdot \hat{n} = \sigma \left(-\frac{\partial \bar{A}}{\partial t} - \nabla V \right) \cdot \hat{n} = 0 \qquad (2.32)$$

Equations (2.31) and (2.32), together with (2.29) and (2.30), form the A-V formulation of eddy current computation. It is listed below:

$$-\nabla^2 \bar{A} + \sigma \frac{\partial \bar{A}}{\partial t} + \sigma \nabla V = 0 \qquad \text{in } \Omega_1$$

$$\nabla \cdot \sigma \left(\frac{\partial \bar{A}}{\partial t} + \nabla V \right) = 0 \qquad \text{in } \Omega_1$$

$$-\nabla^2 \bar{A} = \bar{J}_s \qquad \text{in } \Omega_2 \qquad (2.33)$$

$$\bar{J} \cdot \hat{n} = \sigma \left(-\frac{\partial \bar{A}}{\partial t} - \nabla V \right) \cdot \hat{n} = 0 \qquad \text{on } \Gamma_{12}$$

$\bar{A}$ **Formulation or Modified** $\bar{A}$ **Formulation.** It's possible to define a modified magnetic vector potential $\bar{A}^*$ [18] as

$$\bar{A}^* = \bar{A} + \int \nabla V dt \qquad (2.34)$$

Obviously,

$$\nabla \times \bar{A}^* = \nabla \times \bar{A} = \bar{B}$$

Equations (2.25) and (2.26) can be expressed solely in terms of $\bar{A}^*$

$$\nabla \times \frac{1}{\mu} \nabla \times \bar{A}^* + \sigma \frac{\partial \bar{A}^*}{\partial t} = 0 \qquad \text{in } \Omega_1 \qquad (2.35)$$

$$\nabla \times \frac{1}{\mu} \nabla \times \bar{A}^* = \bar{J}_s \qquad \text{in } \Omega_2 \qquad (2.36)$$

Similarly, Coulomb gauge can be imposed to render a unique solution for $\bar{A}^{*}$. Comparing

equations (2.25) and (2.26) with (2.35) and (2.36), it seems as if the electric scalar potential

V is eliminated. This formulation is also known as A formulation and the $*$ sign is often

omitted. Equations (2.35) and (2.36) can be combined into one equation

$$\nabla \times \frac{1}{\mu} \nabla \times \bar{A} + \sigma \frac{\partial \bar{A}}{\partial t} = \bar{J}_s \qquad \text{in } \Omega \qquad (2.37)$$

In Ω_1, $\bar{J}_s = 0$ and in Ω_2, $\sigma = 0$. With $\bar{A}$ formulation, eddy current density is expressed in

terms of $\bar{A}$.

$$\bar{J} = -\sigma \frac{\partial \bar{A}}{\partial t} \qquad (2.38)$$

Obviously, $\bar{J}$ is solenoidal since the Coulomb gauge is imposed.

$\bar{A}$-V-Ψ **Formulation.** In the $\bar{A}$-V and $\bar{A}$ formulations, a vector potential is

employed in the nonconducting region Ω_2. In reality, a scalar potential is sufficient. This

reduces the number of unknowns from three scalars to one. Suppose $\bar{H}_s$ is the magnetic

field generated by the current source $\bar{J}_s$.

$$\nabla \times \bar{H}_s = \bar{J}_s$$

$\bar{H}_s$ can be determined from Biot-Savart's law.

$$\bar{H}_s = \iiint_V \frac{\bar{J} dv \times \hat{a}_R}{4\pi R^2} \qquad (2.39)$$

The magnetic filed intensity $\bar{H}$ satisfies the following equation

$$\nabla \times \left(\bar{H} - \bar{H}_s \right) = 0$$

Consequently, a scalar potential function can be introduced in the current carrying region Ω_2.

$$\bar{H} = \bar{H}_s - \nabla\Psi \qquad (2.40)$$

where ψ is called reduced magnetic scalar potential function in literature and the potential function Φ introduced in last section is termed total magnetic scalar potential [16,18,25]. Substituting equation (2.40) into (2.4) results in the following equation:

$$\nabla \cdot \mu(\bar{H}_s - \nabla\Psi) = 0 \qquad \text{in} \, \Omega_2 \qquad (2.41)$$

At the interface Γ_{12}, the normal continuity of magnetic flux density and the continuity of current density must be enforced, i.e.

$$(\nabla \times \bar{A}) \cdot \hat{n} = \frac{1}{\mu}(\bar{H}_s - \nabla\Psi) \cdot \hat{n} \qquad (2.42)$$

$$\sigma\left(\frac{\partial \bar{A}}{\partial t} + \nabla V\right) \cdot \hat{n} = 0 \qquad (2.43)$$

Equations (2.29), (2.31) and (2.41), together with interface conditions (2.42) and (2.43) constitute the $\bar{A}$-V-ψ formulation, which is listed below,

$$-\nabla^2\bar{A} + \sigma\frac{\partial \bar{A}}{\partial t} + \sigma\nabla V = 0 \qquad \text{in} \, \Omega_1$$

$$\nabla \cdot \sigma\left(\frac{\partial \bar{A}}{\partial t} + \nabla V\right) = 0 \qquad \text{in} \, \Omega_1$$

$$\nabla \cdot \mu(\bar{H}_s - \nabla\Psi) = 0 \qquad \text{in} \, \Omega_2 \qquad (2.44)$$

$$(\nabla \times \bar{A}) \cdot \hat{n} = \frac{1}{\mu}(\bar{H}_s - \nabla\Psi) \cdot \hat{n} \qquad \text{on} \, \Gamma_{12}$$

$$\sigma\left(\frac{\partial \bar{A}}{\partial t} + \nabla V\right) \cdot \hat{n} = 0 \qquad \text{on} \, \Gamma_{12}$$

In conducting region Ω_1, $\bar{A}$ and V can be combined into $\bar{A}^*$ to form a $\bar{A}^*$-ψ formulation [18].

The Electric vector potential $\bar{T}$ has also been used in eddy current computations. The $\bar{T}$-ψ formulation can be derived similarly [14].

A differential equation must be accompanied by appropriate boundary conditions to render a unique solution. Boundary conditions must be added to the above formulations to form a complete problem description. Boundary conditions will be introduced in the next chapter.

CHARTER 3 BASICS ON FINITE ELEMENT METHOD

3.1 Introduction

The finite element method (FEM) is a numerical technique for obtaining approximate

solutions to various partial differential equations in science and engineering. The need for

numerical methods lies in the fact that exact analytical solutions to many real problems are

prohibitively difficult to find because the geometry or some other features of these problems

are too irregular. Several numerical techniques have been developed in the past few decades,

such as finite difference method and finite element method. Among these, the FEM is

probably the most widely used method in almost every engineering area. This chapter gives

a brief review of the basic idea underlying the FEM. Interested readers may refer to [73] and

[74] for a more detailed coverage.

3.2 Finite Elements and Basis Functions

FEM involves the discretization of the solution domain into a large number of small

regions, called finite elements or simply elements. The unknown function is interpolated

with a set of predefined, linearly independent basis functions and these basis functions are

defined over the finite elements. The discretized solution domain consists of elements, nodes

and line segments, called a finite element mesh. There are many different types of finite

elements. Several commonly used element types and basis functions are introduced in this

section.

1-D Line Element. In one-dimensional problems, the solution domain is discretized

into a number of line segments, each of which is called a 1-D line element. A 1-D line

element has two nodes: the end nodes of the line segments. As an example, Fig 3.1 is a 1-D

mesh, where the solution domain $a \le x \le b$ is divided into four elements. Adjacent elements

connect to each other at the nodes. Every node has a local number, which is numbered

within an element, and a global number, which is numbered in the entire mesh. In Fig 3.1,

there are five global nodes in the mesh. Their global numbers are 1, 2, 3, 4, and 5. In each

element, the local numbers of the two nodes are 1 and 2. The relation between local

numbering and global numbering is built into a table, called connectivity table, shown in

Table 3.1. For example, Table 3.1 shows that node 1 of element 3 has a global number 3 and

node 2 has a global number 4.

A basis function is associated with each node of an element.

$$N_1(x) = \frac{u_2 - x}{u_2 - u_1}$$

$$N_2(x) = \frac{x - u_1}{u_2 - u_1} \tag{3.1}$$

Fig 3.2 shows a plot of the two basis functions associated with the two nodes of a 1-D

line element. These two basis functions, $N_1(x)$ and $N_2(x)$ are defined within an element

and thus termed local basis functions. They have an important property:

$$N_1(u_1) = 1; \quad N_1(u_2) = 0; \quad N_2(u_1) = 0; \quad N_2(u_2) = 1$$

Within an element, an arbitrary function $f(x)$ can be interpolated with the two basis

functions as

$$f(x) = f_1 N_1(x) + f_2 N_2(x).$$

Thus, $f(x)$ is approximated by a linear function, as shown in Fig 3.3. The global basis

functions, which are defined in the entire mesh, are easily obtained by combining each local
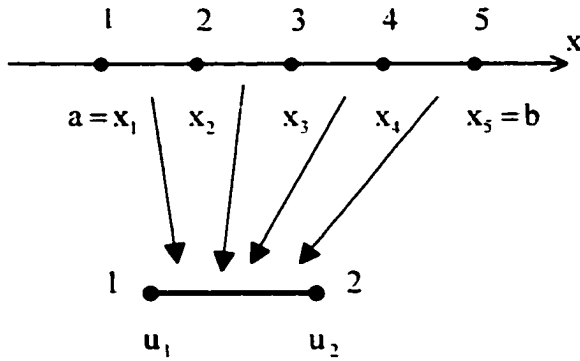
Fig 3.1 A 1-D mesh consisting
of line elements

Table 3.1 Connectivity table
for the 1-D mesh in Fig 3.1

Element Number	Node 1	Node 2
1	1	2
2	2	3
3	3	4
4	4	5
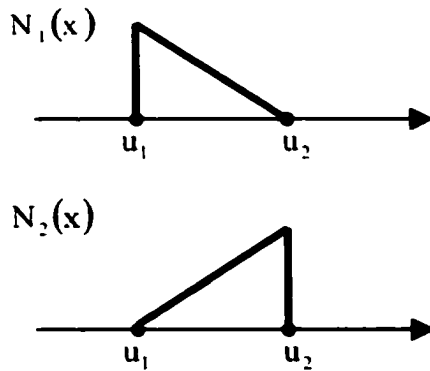
Fig 3.2 Elemental basis functions
for a 1-D line element
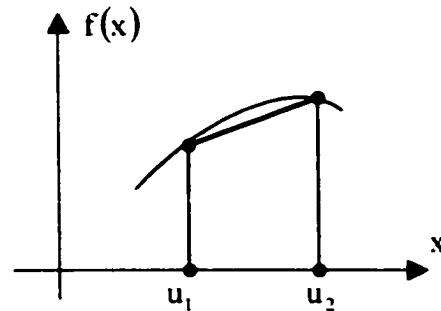
Fig 3.3 Linear approximation of function
f(x) within a line element

basis function associated with a global node. Fig 3.4 shows a plot of the five global basis

functions associated with the five nodes in figure 3.1. The relation between global and local

basis functions is easily seen from the function plots. Each global basis function $n_i(x)$

extends to neighboring elements and has the same property as local basis functions.

$$n_i(x_j) = \begin{cases} 1 & j = i \\ 0 & j \neq i \end{cases}$$

Similarly, combining the approximation of function $f(x)$ in each element shown in Fig 3.3

gives an approximation of $f(x)$ in the entire solution domain, as shown in Fig 3.5. Function
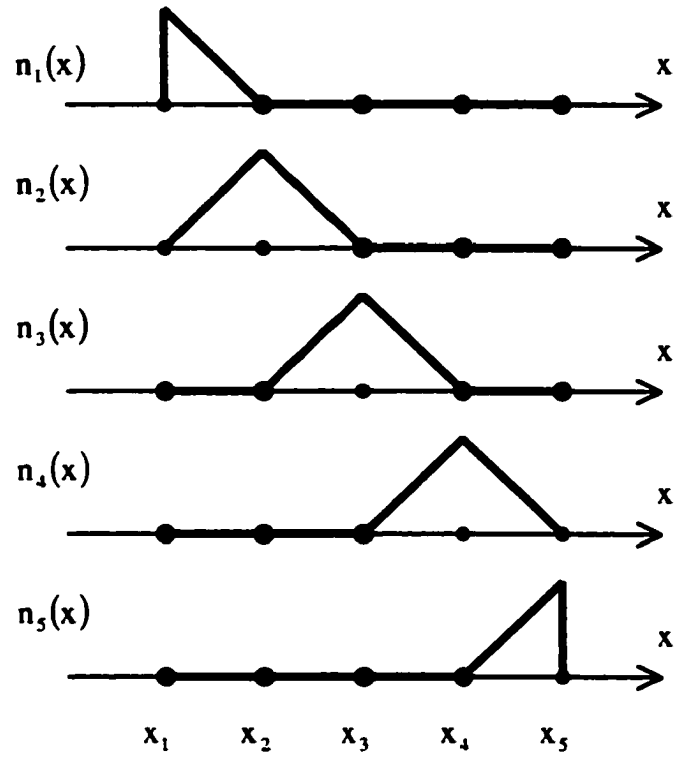
Fig 3.4 Global basis functions for the mesh in Fig 3.1
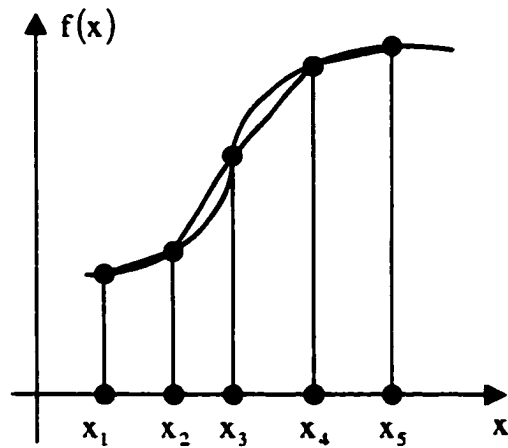
Fig 3.5 Piecewise linear approximation of f(x) on the domain shown in Fig 3.1

$f(x)$ is then expressed as:

$$f(x) = f_1 n_1(x) + f_2 n_2(x) + f_3 n_3(x) + f_4 n_4(x) + f_5 n_5(x).$$

Therefore, given a set of basis functions, an arbitrary function $f(x)$ is uniquely determined

by a set of coefficients f_1, f_2, f_3, f_4, and f_5, and function $f(x)$ is approximated by

piecewise linear line segments. It's easy to verify that these coefficients are actually the

values of the function $f(x)$ at every node. As the number of elements increases, the

piecewise linear approximation becomes closer and closer to the original function.

2-D Triangular Element. A three-node triangular element is commonly used to

discretize the geometry of a two dimensional problem. Fig 3.6 shows a triangular element.

The basis functions associated with node 1, 2, and 3 are given below:

$$N_1(x, y) = \frac{1}{2\Delta}(a_1 + b_1 x + c_1 y)$$

$$N_2(x, y) = \frac{1}{2\Delta}(a_2 + b_2 x + c_2 y)$$

$$N_3(x, y) = \frac{1}{2\Delta}(a_3 + b_3 x + c_3 y) \tag{3.2}$$

where

$$2\Delta = \begin{vmatrix} 1 & x_1 & y_1 \\ 1 & x_2 & y_2 \\ 1 & x_3 & y_3 \end{vmatrix}$$

$$a_1 = x_2 y_3 - x_3 y_2 \qquad b_1 = y_2 - y_3 \qquad c_1 = x_3 - x_2.$$

The other coefficients are obtained by cyclically permuting the subscripts. Δ is the area of

the triangular element. In Fig 3.6, the three nodes are numbered counterclockwise. If

ordered clockwise, a minus sign should be added to Δ. The above basis functions are local

basis functions. The concept of local numbering, global numbering and connectivity table all

apply to 2-D triangular elements and other element types. The global level basis functions
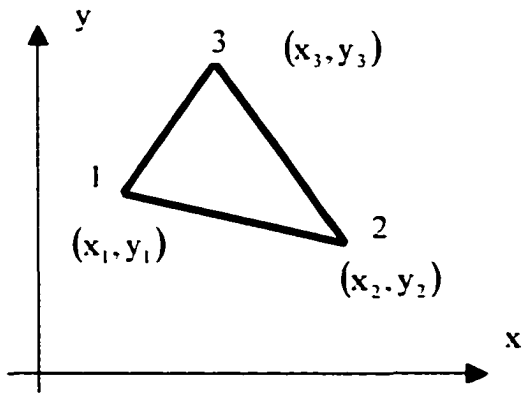
Fig 3.6 A triangular element
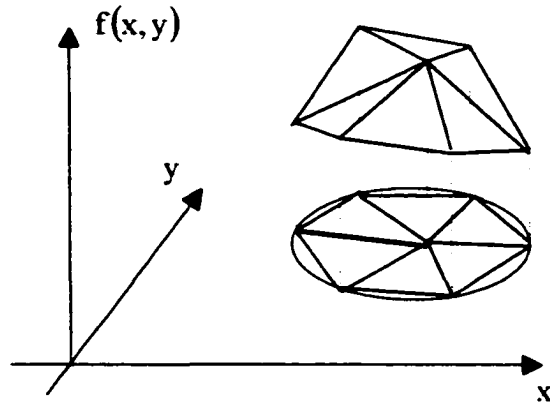
Fig 3.7 Piecewise plane approximation of a 2-D function over a triangular mesh

are obtained similarly as in 1-D line element. With 2-D triangular elements. an arbitrary 2-dimensional function $f(x,y)$ is approximated as piecewise planes over a triangular mesh. as shown in Fig 3.7.

3-D Tetrahedral Element. A four nodes tetrahedron is shown in Fig 3.8. It's a common 3-D element type. The local basis functions are:

$$N_j(x,y,z) = \frac{1}{6V}(a_j + b_j x + c_j y + d_j z), \qquad j = 1,2,3,4 \tag{3.3}$$

where

$$6V = \begin{vmatrix} 1 & x_1 & y_1 & z_1 \\ 1 & x_2 & y_2 & z_2 \\ 1 & x_3 & y_3 & z_3 \\ 1 & x_4 & y_4 & z_4 \end{vmatrix}$$

and

$$a_1 = \begin{vmatrix} x_2 & y_2 & z_2 \\ x_3 & y_3 & z_3 \\ x_4 & y_4 & z_4 \end{vmatrix}, \qquad b_1 = -\begin{vmatrix} 1 & y_2 & z_2 \\ 1 & y_3 & z_3 \\ 1 & y_4 & z_4 \end{vmatrix} \qquad c_1 = -\begin{vmatrix} x_2 & 1 & z_2 \\ x_3 & 1 & z_3 \\ x_4 & 1 & z_4 \end{vmatrix}, \qquad d_1 = -\begin{vmatrix} x_2 & y_2 & 1 \\ x_3 & y_3 & 1 \\ x_4 & y_4 & 1 \end{vmatrix}$$
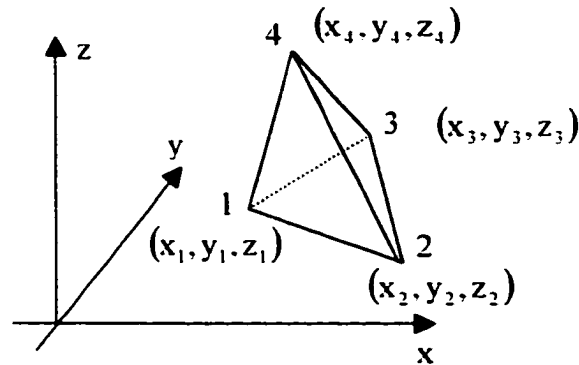
Fig 3.8 A tetrahedral element

The other coefficients are obtained through a cyclic permutation of the subscripts 1, 2, 3, and 4. V is the volume of the tetrahedron formed by nodes 1, 2, 3, and 4. The tetrahedron is defined such that nodes 1, 2, and 3 are numbered counterclockwise when viewed from node 4.

Summarizing the above discussion, the solution domain of a finite element analysis is discretized into finite elements. A basis function is associated with each node of the finite element mesh. An arbitrary function defined over the solution domain is then approximated by an interpolation with the basis functions. The unknown function is uniquely determined by the set of interpolation coefficients. The values of these coefficients are the values of the function at the nodes of the finite element mesh. The purpose of a finite element analysis is to find these coefficients. We'll see later that these interpolation coefficients can be found by solving a linear system.

The above three types of finite elements and their basis functions have the following common properties:

1. There exists a basis function for each node of the element and these basis functions form a linearly independent set. The local basis function is defined

within an element. The global basis function extends to all elements which share

the common node.

2. $\quad N_i(x_j) = \begin{cases} 1 & j = i \\ 0 & j \neq i \end{cases} \qquad i, j = 1, 2, \ldots M$ (3.4)

$\quad n_i(x_j) = \begin{cases} 1 & j = i \\ 0 & j \neq i \end{cases} \qquad i, j = 1, 2, \ldots NNP$ (3.5)

where N_i is the local basis function and n_i is the global basis function; M is the

number of nodes in an element and NNP is the total number of nodes in the mesh.

The value of N_i or n_i changes linearly from node i to node j.

3. Basis functions are continuous on inter-element boundaries.

4. An arbitrary scalar function f in an element can be interpolated with the local

basis functions as

$$f = \sum_{j=1}^{M} f_j N_j$$ (3.6)

An arbitrary function over the discretized solution domain can be expressed in

terms of the global basis functions.

$$f = \sum_{j=1}^{NNP} f_j n_j$$ (3.7)

These properties are also the basic principles for constructing the finite elements and their

basis functions. The three types of finite elements introduced in this section possess linear

basis functions and the basis functions are continuous across elements. Thus, they are termed

first order elements. In some applications, besides the continuity of the unknown function,

the first order or even higher order derivatives are required to be continuous across element

interface. In such cases, higher order elements are constructed. However they greatly

increase the storage and computation time and therefore seldom used. Interested readers may

refer to [75] for other types of elements and basis functions.

3.3 The Weak Form and Galerkin's Approach

A differential equation must be accompanied by appropriate boundary conditions to

render a unique solution. Consider the following boundary value problem, described by

Poisson's equation:

$$\nabla^2 u = f(x, y, z) \qquad \text{in } \Omega \qquad (3.8)$$

$$u = g \qquad \text{on } S_1 \qquad (3.9)$$

$$\frac{\partial u}{\partial n} + \alpha u = h \qquad \text{on } S_2 \qquad (3.10)$$

where $S_1 \cup S_2 = \partial \Omega$ and $S_1 \cap S_2 = 0$. Ω is the solution domain and $\partial \Omega$ is its boundary,

which is divided into S_1 and S_2. Equation (3.9) specifies the value of the unknown field on

boundary S_1. This kind of boundary conditions is known as Dirichlet condition. If $\alpha = 0$,

equation (3.10) reduces to

$$\frac{\partial u}{\partial n} = h \qquad \text{on } S_2 \qquad (3.11)$$

This kind of boundary condition specifies the value of the derivative of the unknown function

and is known as Neumann condition. Equation (3.10) includes both the unknown function

and its derivative. It is called Cauchy condition or mixed condition. The problem described

by equations (3.8)-(3.10) is termed a classical problem. Its analytical solution is called a

classical solution.

To ease the treatment of boundary conditions, first consider the following

homogeneous Dirichlet condtion on S_1 :

$$u = 0 \qquad\qquad \text{on } S_1 \qquad\qquad\qquad (3.12)$$

The finite element method does not solve the classical problem directly, but rather solve the

corresponding weak problem. That means it seeks a solution which satisfies equation (3.8) in

a weak sense or in an average sense. The weak problem corresponding to the above classical

problem is stated as follows:

Obtain a solution u which satisfies the weak form:

$$\iiint_\Omega \nabla^2 u \cdot w \, dV = \iiint_\Omega f(x,y,z) \cdot w \, dV \qquad\qquad (3.13)$$

In the above equation, $u \in F$ is a trial solution and $w \in F$ is an arbitrary test function. F is a

functional space which is sufficiently smooth, square integrable and satisfies the

homogeneous Dirichlet boundary condition (3.12). Invoking Green's formula, equation

(3.13) becomes

$$\iiint_\Omega \nabla u \cdot \nabla w \, dV = \iint_{S_1} w \frac{\partial u}{\partial n} \, dS + \iint_{S_2} w \frac{\partial u}{\partial n} \, dS - \iiint_\Omega f(x,y,z) \cdot w \, dV \qquad (3.14)$$

Because the test function w satisfies the homogeneous Dirichlet condition on S_1 , the first

surface integral on the right hand side vanishes. Substituting Cauchy condition into the

above equation, equation (3.14) reduces to

$$\iiint_\Omega \nabla u \cdot \nabla w \, dV = \iint_{S_2} w(h - \alpha u) \, dS - \iiint_\Omega f(x,y,z) \cdot w \, dV \qquad (3.15)$$

Since the Dirichlet condition is imposed on the functional space F, it is also called an

essential boundary condition. Since the Neumann condition and the Cauchy condition are

satisfied by the weak form naturally, they are called natural boundary conditions. It is easy

to verify that any classical solution satisfies equation (3.15) and vice versa.

To find an approximate solution to the weak problem, the FEM begins by discretizing

the solution domain into finite elements and restricting the functional space F to be a finite

dimensional space F^h. The discretized weak problem seeks a solution u^h which satisfies the

following discretized weak form,

$$\iiint_{\Omega^h} \nabla u^h \cdot \nabla w^h dV = \iint_{S_2^h} w^h (h - \alpha u^h) dS - \iiint_{\Omega^h} f(x,y,z) \cdot w^h dV \tag{3.16}$$

where Ω^h and S_2^h are the discretized solution domain and its Cauchy boundary. Suppose the

cardinality of F^h is N and n_j, $j = 1, 2, ...N$, is a set of basis of F^h. Then a trial function u^h

can be expressed as,

$$u^h = \sum_{j=1}^{N} u_j n_j \tag{3.17}$$

Since the test function w^h is an arbitrary function from the functional space F^h, it is enough

to require that equation (3.16) is satisfied for every basis of F^h. Substituting equation (3.17)

into equation (3.16) and letting $w^h = n_i$ for $i = 1, 2, ...N$ results in the following equation:

$$\sum_{j=1}^{n} \left(\iiint_{\Omega^h} \nabla n_i \cdot \nabla n_j dV + \iint_{S_2^h} n_i \alpha n_j dS \right) u_j = \iint_{S_2^h} h n_i dS - \iiint_{\Omega^h} f n_i dV,$$
$$i = 1, 2, ...N \tag{3.18}$$

This is a linear system. Expressing it in a matrix form,

$$[A] \cdot [u] = [b] \tag{3.19}$$

Equation (3.19) is the finite element equation. The coefficient matrix $[A]_{n \times n} = [a_{ij}]$ is called

the stiffness matrix and the right hand side $[b]_{n \times 1} = [b_i]$ is called the load vector. $[u]_{n \times 1} = [u_i]$

is the unknown vector, which is the set of interpolation coefficients in equation (3.17). So, the solution of (3.19) gives a set of interpolation coefficients, which gives an approximate solution of the unknown function.

From the last section, we know that basis functions of a finite element mesh form a linearly independent set. Consequently the finite dimensional function space F^h can be chosen to be the space spanned by the global basis functions of a finite element mesh. Then the basis functions in equations (3.17) and (3.18) are chosen to be the global basis functions of finite elements. Its dimension is the number of global nodes. The above method is called Galerkin's approach, also known as the method of weighted residuals. The reason is easily seen from equation (3.13). Rearranging terms, the equation becomes,

$$\iiint_{\Omega} \left(\nabla^2 u - f(x,y,z) \right) \cdot w \, dV = 0$$

Here, $\nabla^2 u - f$ is the residual of the original classical problem and w can be viewed as a weight function. Then, the weak problem requires that the average weighted residual to be zero.

The above finite element formulation requires the trial and test function satisfy the homogeneous Dirichlet condition (3.12) on S_1. In the general case, an inhomogeneous Dirichlet condition, such as equation (3.9), needs to be imposed. This cannot be done by restricting the functional space F directly. Suppose $u_1 \in F$ and $u_2 \in F$. Then $u_1 + u_2 \notin F$. In this case, F is not a linear space at all. The inhomogeneous Dirichlet condition can be imposed in two different ways. First, let v=u-g. One choice of g can be

$$g = \sum_{j=1}^{M_1} g_j n_j$$

where M_l is the number of nodes on S_l and n_j is the corresponding basis function.

Obviously, v satisfies the homogeneous Dirichlet condition. Consequently v can be found by the above finite element formulation. Then,

$$u = v + \sum_{j=1}^{M_l} g_j n_j$$

This method is difficult to handle. The second approach simply ignores the Dirichlet condition and deletes the first surface integral in equation (3.14). The Dirichlet conditions, $u_j = g_j$, $j = 1,2,...M_l$, are imposed on the final linear equation (3.19). It can be shown that these two methods are equivalent [76]. The second method is usually implemented in FEM codes because of its simplicity.

The finite element equation (3.18) can also be derived from a variational approach, also known as the Ritz method [73-76]. It begins with a functional, which is usually the stored energy in electromagnetic fields. Then it selects a function from a trial function family as a solution by minimizing the functional with respect to a set of adjustable parameters. Therefore, the Ritz method seeks a solution which renders the functional stationary. The Ritz method results in the same finite element equation as Galerkin's method.

To facilitate the implementation of finite element method, the finite element equation (3.18) is usually formed at the element level first. The discretized solution domain Ω^h consists of a number of finite elements, i.e.

$$\Omega^h = \sum_{k=1}^{NEL} \Omega_k^e$$

where NEL is the number of elements in the finite element mesh. Equation (3.18) can also

be expressed as

$$\sum_{k=1}^{NEL}\left[\sum_{j=1}^{n}\left(\iiint_{\Omega_k^e}\nabla N_i\cdot\nabla N_j dV+\iint_{S_{2k}^e}N_i\alpha N_j dS\right)u_j^e\right]=\sum_{k=1}^{NEL}\left[\iint_{S_{2k}^e}hN_i dS-\iiint_{\Omega_k^e}fN_i dV\right]$$

$$i=1,2,...NNPE \qquad\qquad (3.20)$$

where NNPE is the number of nodes in one element and N_i is the local basis function. Here,

the global basis function n_i is disassembled into local basis functions. It is easy to verify

that equation (3.20) is equivalent to (3.18). The element level linear system is formed by the

following formulas:

$$[A^e]\cdot[u^e]=[b^e] \qquad\qquad (3.21)$$

$$a_{ij}^e=\iiint_{\Omega_k^e}\nabla N_i\cdot\nabla N_j dV+\iint_{S_{2k}^e}N_i\alpha N_j dS \qquad\qquad (3.22)$$

$$b_i^e=\iint_{S_{2k}^e}hN_i dS-\iiint_{\Omega_k^e}fN_i dV \qquad\qquad (3.23)$$

$$i,j=1,2,...NNPE,\ \ k=1,2,...N_{el}$$

The global finite element equation (3.19) is then obtained by assembling each of the element

equations. The connectivity table, introduced in last section, contains the relation between

local numbering and global numbering of nodes. It is used here to add the coefficients in

elemental matrices into the corresponding positions in global matrices. Such a process is

called assembly. Once the global linear system is obtained, the next step is to solve the linear

system.

3.4 The Linear Solver

The linear equation solver plays a critical role in the performance of a finite element

code, since solving the linear system consumes most of the computation time and the

stiffness matrix consumes most of the storage space. Generally, two different kinds of linear

solvers are available: the direct solver and the iterative solver. Different storage schemes are

used for the two kinds of solvers.

Direct Solver. A direct solver provides a solution after a finite number of arithmetic

operations. In the absence of rounding error, a direct solver gives an accurate solution. In

many cases, the stiffness matrix is usually a symmetric and positive definite matrix, the

Cholesky's method, a symmetric variant of Gaussian elimination, is very popular for solving

the finite element equations. Given a linear system,

$$[A] \cdot [x] = [b] \tag{3.24}$$

First, the coefficient matrix is factorized into the product of a lower triangular matrix with

positive diagonal elements and its transpose. Equation (3.24) becomes

$$[L] \cdot [L]^T \cdot [x] = [b] \tag{3.25}$$

Next, backsubstitution is performed on the following two triangular systems to obtain $[x]$.

$$[L] \cdot [y] = [b] \tag{3.26}$$
$$[L]^T \cdot [x] = [y] \tag{3.27}$$

Backsubstitution is usually very fast and most of the computation time is spent on the

triangular factorization.

Since the stiffness matrix from finite element formulation is usually highly sparse,

exploiting the huge number of zero elements reduces the storage significantly. The band

method and its closely related variant called the envelope method are two of the most popular

techniques [77]. These two methods assume that most of the nonzero elements are distributed in the vicinity of the main diagonal as shown in Fig 3.9. Since symmetric matrices are considered, only the lower triangular part is shown. Fig 3.9 (a) shows the banded storage scheme, which assumes that all the nonzero elements are within a small band centered at the main diagonal. The actual storage needed is characterized by the bandwidth of the matrix, which is defined as

$$ bw = max\{|i - j|, a_{ij} \neq 0\}, \qquad i, j = 1, 2, ... n $$

where n is the dimension of the coefficient matrix. Fig 3.9 (b) shows the envelope storage scheme, which allows the bandwidth different for each row. The envelope size, which is defined as the number of elements within the envelope, is used to describe the storage requirement of this method. The triangular factorization usually suffers from fill-in, which refers to that $[L]$ has nonzero elements in positions which are zeros in the lower triangular part of $[A]$. Fortunately, the fill-in's only happen within the bandwidth or envelope. This fact allows all the zeros outside the bandwidth or envelope to be discarded. Then, only elements within the bandwidth or envelope are stored. The band method works well if the bandwidth doesn't vary too much with rows. Generally, the envelope method is more effective in exploiting the sparsity.

The global numbering of nodes has an impact on the bandwidth or envelope size. From the point view of storage only, the numbering which results in the minimum bandwidth or envelope size is the best choice. The reverse Cuthill-McKee (RCM) ordering algorithm is the most widely used bandwidth or envelope size reduction algorithm. See [77] for details.

(a)   (b)
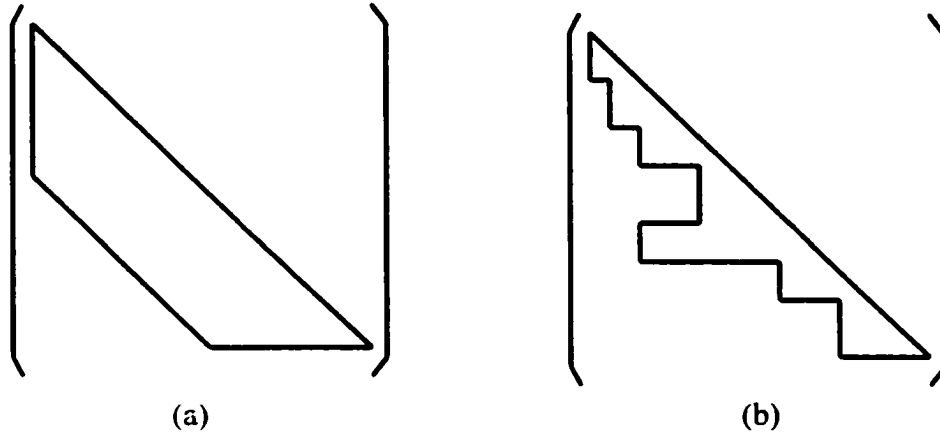
Fig 3.9 Banded storage and envelope storage scheme

Iterative Solver. An iterative solver begins from an initial approximation of the

solution $\left[x^0\right]$ and seeks a sequence $\left[x^k\right]$, such that $\lim_{k\to\infty}\left[x^k\right]=\left[x\right]$. Split the coefficient matrix

into two matrices: M and N.

$$[A]=[M]-[N]$$

Substituting it into equation (3.24), a solution may be reached by the following iterative

equation:

$$\left[x^{k+1}\right]=[B]\cdot[x]+[c]$$
$$[B]=[M]^{-1}[N], \qquad [c]=[M]^{-1}[b] \tag{3.28}$$

Where [B] is termed the iterative matrix. Iterative solvers mainly involve matrix vector

multiplication. Since zero elements contribute nothing in matrix vector multiplication, all the

zero elements in the sparse matrix can be discarded. So, in an iterative solver, only nonzero

elements are stored and usually in an array. Additional arrays are needed for the purpose of

indexing the nonzero elements. Even so, the storage requirement of an iterative solver is far

less than that of a direct solver, especially for a large linear system. But iterative solvers are

likely to suffer from slow convergence. The robustness may be improved by

preconditioning. Various iterative algorithms have been developed in recent years. See [78] for reference.

It is hard to determine which kind of solver is better for addressing a particular problem since it depends on the specific situation. If a very large linear system is being solved, the storage capacity of the computing facility may be the first consideration. An iterative solver is the best choice due to its low storage requirements. However in some situations, many linear systems with the same coefficient matrix must be solved. A direct solver may be better, because the coefficient matrix needs to be factorized only once.

3.5 General Procedures for Finite Element Method

Generally, a typical finite element analysis is divided into the following steps: generating the finite element mesh, selecting a set of basis functions, evaluating the elemental equation, assembling the global linear system, solving the linear system, and processing the results.

Discretize the solution domain. Also known as mesh generation, this is the first step in a finite element analysis. An appropriate type of finite element is chosen to discretize the solution domain. One or more unknown variables, or degrees of freedom, are assigned to the nodes in the mesh. The nodes are numbered both locally and globally. A connectivity table is built to maintain the correspondence between local numbering and global numbering scheme.

Select basis functions. This is usually done in combination with step 1 when the type of element is chosen. For a particular element type, first order or higher order basis functions are chosen according to the continuity requirement of the solution.

Evaluate the stiffness matrix and load vector in element level. Once the mesh and

a set of basis functions are established, we are ready to evaluate the element level stiffness

matrix and load vector. For example, equations (3.22) and (3.23) are the corresponding

formulas for the example in the last section. Such formulas usually involve the evaluation of

integrals. Closed form analytical integration is possible for 1-D line element, 2-D triangular

element and 3-D tetrahedral element [75,76]. However, for other element types, such as 2-D

quadrilateral element and 3-D hexahedral element, numerical integration techniques have to

be employed. The Gauss-Cotes quadrature is often used in such cases [79].

Assemble the element properties to obtain the global linear system. After the

element equation is formed for each element, they are assembled to form the global linear

system. The connectivity table built in step 1 is used to add coefficients in elemental

stiffness matrix and load vector into the corresponding positions in their global counterparts.

Solve the global linear system. A linear solver is invoked to solve the global linear

system to obtain the unknown vector, which is the value of the unknown variable at every

node. Currently available linear solvers fall into two general classes: direct and iterative. To

choose a particular solver, a number of factors must be considered, such as, the property of

the stiffness matrix, the storage and computation time etc.

Perform additional computations and interpret the numerical results. Additional

calculations are often needed. For example, it is often desired to calculate electromagnetic

field variables from potential functions.

CHAPTER 4 NUMERICAL SIMULATION OF EDDY CURRENT PROBLEMS USING EDGE BASED FINITE ELEMENTS

4.1 Introduction

Three formulations are introduced in section 2.8 for eddy current computations.

Consider the simplest $\bar{A}$ formulation in frequency domain

$$-\nabla^2\bar{A} + j\omega\sigma\bar{A} = \bar{J}_S \qquad (4.1)$$

In a finite element analysis, the unknown field is interpolated with a set of basis functions.

All the basis functions introduced so far are scalar functions while equation (4.1) is a vector

equation. How does one interpolate a vector field with scalar basis functions? One natural

choice is to decompose the vector field into its three Cartesian components. Then the

original vector differential equation is equivalent to the following three scalar equations:

$$-\nabla^2 A_x + j\omega\sigma A_x = J_{sx} \qquad (4.2)$$
$$-\nabla^2 A_y + j\omega\sigma A_y = J_{sy} \qquad (4.3)$$
$$-\nabla^2 A_z + j\omega\sigma A_z = J_{sz} \qquad (4.4)$$

The three scalar components, A_x, A_y, and A_z, can be represented by scalar basis functions

as discussed before. Since the scalar basis functions and thus the unknowns in the finite

element equation are assigned to nodes of the finite element mesh, the conventional finite

element method introduced in last chapter is known as node based finite elements or node

elements. Such finite elements are suitable for analyzing scalar fields. When used in

analyzing a vector field, it has to be decomposed into its three Cartesian components.

However, vectors have physical meanings. They are not just triplets of numbers. By

dividing a vector into its scalar components, node based finite elements fail to take this into

account. For example, in electromagnetics, the boundary conditions usually take the form of

restricting either tangential or normal components. By the very nature of nodal interpolation, all the scalar components of a vector are continuous on the inter-element boundaries. This violates the boundary conditions if the element boundary happens to be the interface between materials with different electromagnetic properties. Better problem formulations, such as $\bar{A}$-V and $\bar{A}$-V-Ψ formulation, may solve the problem partially, but at the price of introducing additional variables, which increases the complexity and makes the computation inefficient. This situation forces us to turn to vector finite elements.

An alternative to the conventional node based finite elements is the edge based finite element or edge elements. Edge elements are just special kinds of finite elements whose degrees of freedoms are assigned to edges of elements rather than nodes. The basis functions are associated with edges of finite elements too, and more importantly, the basis functions are vector functions. An arbitrary vector field can be interpolated with the set of vector basis functions directly. It is no longer necessary to decompose it into its scalar components any more. So unlike node based finite elements, edge elements are vector oriented. Edge elements have a few useful properties. For example, they enforce tangential continuity on vectors but not normal continuity. They allow a vector field to be separated into the sum of the gradient of a scalar function and the remaining part. They can easily deal with field singularities and more. In the next few sections, several of them will be discussed. Interested readers may refer to [62] for additional details.

4.2 Edge Based Finite Elements

To explain the basic principles of edge elements, consider a 2-D quadrilateral element shown in Fig 4.1 as an example. An arbitrary 2-D quadrilateral element in x-y plane is

defined as the map from a unit square in the transformed domain: u-v plane. The mapping is given as follows,

$$x = \sum_{j=1}^{4} x_j N_j(u, v)$$

$$y = \sum_{j=1}^{4} y_j N_j(u, v) \tag{4.5}$$

where N_j, $j = 1, 2, 3,$ and 4, are the basis functions associated with the four nodes

respectively. They are given by the following equations:

$$N_1(u, v) = (1 - u)(1 - v)$$
$$N_2(u, v) = u(1 - v)$$
$$N_3(u, v) = uv \tag{4.6}$$
$$N_4(u, v) = (1 - u)v$$

It is easy to verify that these basis functions satisfy the properties of the basis functions

discussed in section 3.2. Equations (4.5) and (4.6) define the geometry of an arbitrary

quadrilateral element. These four basis functions can also be used to represent any scalar

functions. To distinguish them from the vector basis functions introduced later, they are

termed scalar basis functions or node basis functions.

A set of four vector basis functions is assigned to the four edges of the element to

represent a vector field. They are expressed as follows:

$$\bar{N}_1^e = (1 - v)\nabla u$$
$$\bar{N}_2^e = u\nabla v$$
$$\bar{N}_3^e = v\nabla u \tag{4.7}$$
$$\bar{N}_4^e = (1 - u)\nabla v$$

Here, $\bar{N}_j^e$, $j = 1, 2, 3,$ and 4, is the vector basis function associated with edge j, termed vector

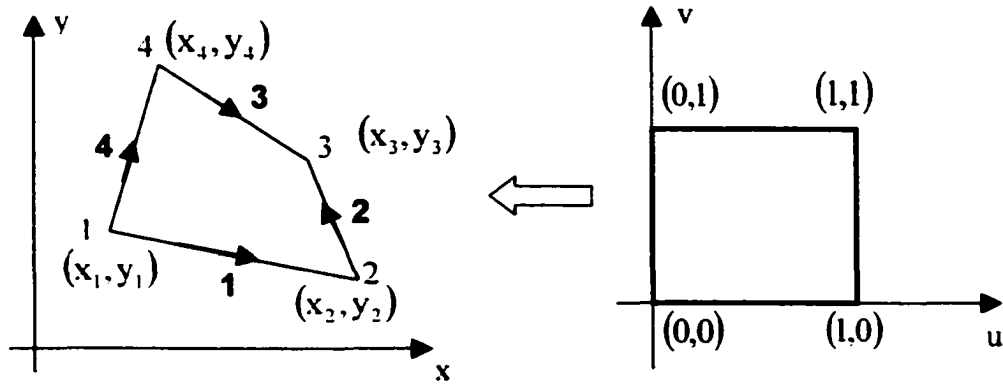basis function or edge basis function. The arrow on edge j in Fig 4.1 refers to the direction of

Fig 4.1 A 2-D quadrilateral element

tangential component of $\bar{N}_j^e$ along edge j. An arbitrary vector field $\bar{A}$ within the element is

then interpolated as

$$\bar{A} = \sum_{j=1}^{4} A_j \bar{N}_j^e(u, v)$$ (4.8)

Fig 4.2 shows plots of the four edge basis functions. The length and direction of an

arrow represent the magnitude and direction of the edge basis function respectively. Both the

magnitude and direction are functions of space coordinates. We can see that the set of edge

basis functions possess an important property: $\bar{N}_j^e$ has tangential component only along edge

j and has no tangential components along any of the other three edges. This property is

expressed in the following equation

$$\int_{E_i} \bar{N}_j^e \cdot d\bar{l} = \begin{cases} 1 & j = i \\ 0 & j \neq i \end{cases}$$ (4.9)

This implies that the line integral of $\bar{N}_j^e$ along edge j is 1 and the integral is zero along any of

the other edges. This property is also one of the basic principles that is employed to

construct an edge element and its vector basis functions. It is this property that makes the
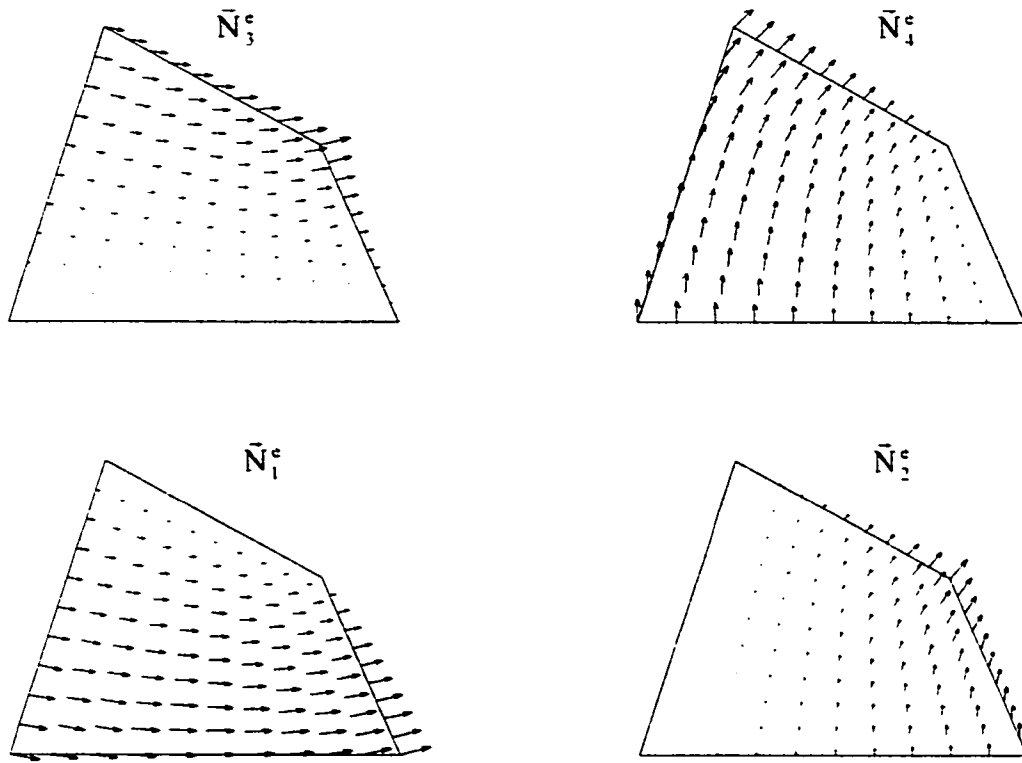
Fig 4.2 The edge basis functions for a quadrilateral element

edge elements enforce only tangential continuity across elements. Furthermore, this property

implies an important fact concerning edge elements. The interpolation coefficient A_j in

equation (4.8) controls the tangential component of the vector field $\bar{A}$ along edge j.

$$\int_{E_i} \bar{A} \cdot d\bar{l} = \sum_J \int_{E_i} A_j \bar{N}_j^e \cdot d\bar{l} = A_i \int_{E_i} \bar{N}_i^e \cdot d\bar{l} = A_i \qquad (4.10)$$

The above equation implies that the value of the interpolation coefficient A_i is the line

integral of the vector field $\bar{A}$ along edge i. The purpose of an edge based finite element

analysis is to find out these interpolation coefficients. Because of the above properties, edge

elements enforce only tangential continuity across the element boundaries but allow the

normal component free to jump. The relaxation in continuity is consistent with the boundary conditions in electromagnetics. Welij [80] presented a formulation on eddy current computation in terms of magnetic field intensity $\bar{H}$ directly. By nature of the edge basis functions, the continuity of the tangential components of $\bar{H}$ is imposed while the normal component is allow to jump at inter-element boundaries. Hence, edge elements impose the boundary conditions in a natural way.

In this research, 3-D hexahedral elements, shown in Fig 4.3, are employed to simulate 3-dimensional static and quasistatic electromagnetic field problems. Similar to 2-D quadrilateral elements, an arbitrary hexahedral element in x-y-z space is defined as the map from a unit cubic element in the transformed domain: u-v-w space. Equation (4.11) gives the mathematical expression of the mapping.

$$
\begin{aligned}
x &= \sum_{j=1}^{8} x_j N_j (u, v, w) \\
y &= \sum_{j=1}^{8} y_j N_j (u, v, w) \\
z &= \sum_{j=1}^{8} z_j N_j (u, v, w)
\end{aligned}
\tag{4.11}
$$

Where N_j's are nodal basis functions associated with the eight nodes. Equation (4.12) and (4.13) are the corresponding expressions of the eight nodal basis functions and twelve edge basis functions. It's trivial to verify that a 3-D hexahedral element shares the same properties as that of a 2-D quadrilateral element. Other types of elements exit, such as 2-D triangular elements and 3-D tetrahedral elements. They are also commonly used in edge based finite element analysis. Interested readers may refer to [62] and [74] for details.
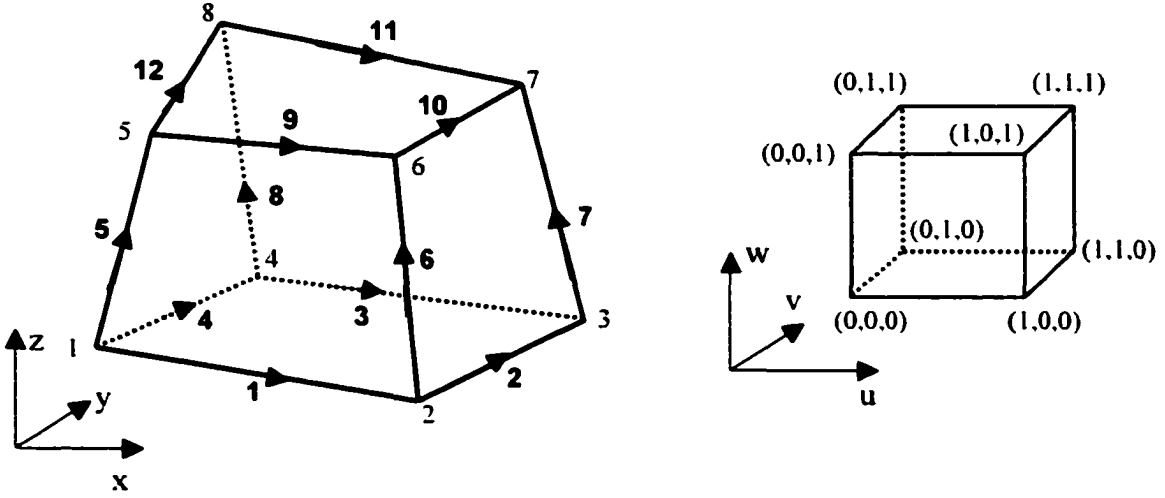
Fig 4.3 A 3-D hexahedral element

$$N_1(u,v,w) = (1-u)\cdot(1-v)\cdot(1-w)$$
$$N_2(u,v,w) = u\cdot(1-v)\cdot(1-w)$$
$$N_3(u,v,w) = u\cdot v\cdot(1-w)$$
$$N_4(u,v,w) = (1-u)\cdot v\cdot(1-w)$$
$$N_5(u,v,w) = (1-u)\cdot(1-v)\cdot w \tag{4.12}$$
$$N_6(u,v,w) = u\cdot(1-v)\cdot w$$
$$N_7(u,v,w) = u\cdot v\cdot w$$
$$N_8(u,v,w) = (1-u)\cdot v\cdot w$$

$$\bar{N}_1^e(u,v,w) = (1-v-w+v\cdot w)\cdot\nabla u$$
$$\bar{N}_2^e(u,v,w) = (u-w\cdot u)\cdot\nabla v$$
$$\bar{N}_3^e(u,v,w) = (v-v\cdot w)\cdot\nabla u$$
$$\bar{N}_4^e(u,v,w) = (1-w-u+w\cdot u)\cdot\nabla v$$
$$\bar{N}_5^e(u,v,w) = (1-u-v+u\cdot v)\cdot\nabla w$$
$$\bar{N}_6^e(u,v,w) = (u-u\cdot v)\cdot\nabla w$$
$$\bar{N}_7^e(u,v,w) = u\cdot v\cdot\nabla w \tag{4.13}$$
$$\bar{N}_8^e(u,v,w) = (v-u\cdot v)\cdot\nabla w$$
$$\bar{N}_9^e(u,v,w) = (w-w\cdot v)\cdot\nabla u$$
$$\bar{N}_{10}^e(u,v,w) = w\cdot u\cdot\nabla v$$
$$\bar{N}_{11}^e(u,v,w) = v\cdot w\cdot\nabla u$$
$$\bar{N}_{12}^e(u,v,w) = (w-w\cdot u)\cdot\nabla v$$

4.3 Magnetic Vector Potential Formulation for Eddy Current Problems

Magnetic vector potential formulation ($\bar{A}$ formulation) or modified $\bar{A}$ formulation was introduced in section 2.8. Considering the steady state case under sinusoidal excitation, the complete problem description with homogeneous Dirichlet boundary condition and inhomogeneous Neumann boundary condition is stated below

$$\nabla \times \frac{1}{\mu} \nabla \times \bar{A} + j\omega\sigma\bar{A} = \bar{J}_s \qquad \text{in } \Omega \qquad (4.14)$$

$$\bar{A} \times \hat{n} = 0 \qquad \text{on } S_1 \qquad (4.15)$$

$$\bar{H} \times \hat{n} = h \qquad \text{on } S_2 \qquad (4.16)$$

where $S_1 \cup S_2 = \partial\Omega$ and $S_1 \cap S_2 = 0$. Ω is the solution domain and $\partial\Omega$ is its boundary, which is divided into S_1 and S_2. A homogeneous Dirichlet boundary condition is imposed on S_1 and Neumann boundary condition is imposed on S_2. Since the magnetic vector potential $\bar{A}$ is not a directly measurable quantity, the physical sense of the Dirichlet condition is not clear from equation (4.15). Actually, equation (4.15) implies $\bar{B} \cdot \hat{n} = 0$ on S_1. To see this, note the following vector identity (The symbol $\bar{A}$ and $\bar{B}$ represent two arbitrary vectors. They don't have any physical meaning).

$$\bar{B} \cdot \nabla \times \bar{A} = \nabla \cdot (\bar{A} \times \bar{B}) + \bar{A} \cdot \nabla \times \bar{B} \qquad (4.17)$$

Apply this vector identity to $\bar{B} \cdot \hat{n}$.

$$\bar{B} \cdot \hat{n} = \hat{n} \cdot \nabla \times \bar{A} = \nabla \cdot (\bar{A} \times \hat{n}) + \bar{A} \cdot \nabla \times \hat{n}$$

Note $\nabla \times \hat{n} = 0$. Therefore, the Dirichlet condition (4.15) implies the vanishing normal component of magnetic flux density, while the Neumann condition specifies the tangential component of magnetic field intensity on S_2.

The weak form of the classical problem described by equations (4.14)-(4.16) is:

$$\iiint_{\Omega} \left(\nabla \times \frac{1}{\mu} \nabla \times \bar{A} \right) \cdot \bar{W} dV + \iiint_{\Omega} j\omega\sigma\bar{A} \cdot \bar{W} dV = \iiint_{\Omega} \bar{J}_s \cdot \bar{W} dV \qquad (4.18)$$

where $\bar{A}$ is a trial solution and $\bar{W}$ is an arbitrary test function. Both $\bar{A}$ and $\bar{W}$ are

sufficiently smooth, square integrable and satisfy the homogeneous Dirichlet boundary

condition (4.15). Invoking the vector identity (4.17) and divergence theorem, the first

integral in equation (4.18) becomes:

$$\iiint_{\Omega} \left(\nabla \times \frac{1}{\mu} \nabla \times \bar{A} \right) \cdot \bar{W} dV$$

$$= \iiint_{\Omega} \frac{1}{\mu} \nabla \times \bar{A} \cdot \nabla \times \bar{W} dV + \oiint_{\partial\Omega} \frac{1}{\mu} (\nabla \times \bar{A}) \times \bar{W} \cdot \hat{n} dS \qquad (4.19)$$

Note

$$\hat{n} \cdot \frac{1}{\mu} (\nabla \times \bar{A}) \times \bar{W} = \frac{1}{\mu} (\nabla \times \bar{A}) \cdot \bar{W} \times \hat{n} = \bar{W} \cdot \hat{n} \times \frac{1}{\mu} (\nabla \times \bar{A})$$

The surface integral in equation (4.19) becomes

$$\oiint_{\partial\Omega} \frac{1}{\mu} (\nabla \times \bar{A}) \times \bar{W} \cdot \hat{n} dS = \iint_{S_1} \frac{1}{\mu} \nabla \times \bar{A} \cdot \bar{W} \times \hat{n} dS + \iint_{S_2} \frac{1}{\mu} \nabla \times \bar{A} \times \hat{n} \cdot \bar{W} dS$$

Since the test function $\bar{W}$ satisfies the homogeneous Dirichlet condition (4.15) on S_1, the

first surface integral on the right hand side vanishes. The Neumann condition (4.16) can be

substituted into the second surface integral. Then the weak form reduces to:

$$\iiint_{\Omega} \left[(\nabla \times \bar{W}) \frac{1}{\mu} (\nabla \times \bar{A}) + j\omega\sigma\bar{W} \cdot \bar{A} \right] dV = \iiint_{\Omega} \bar{J}_s \cdot \bar{W} dV + \iint_{S_2} (\bar{H} \times \hat{n}) \bar{W} dS \quad (4.20)$$

Suppose the solution domain Ω is discretized using hexahedral elements.

Interpolating the vector field $\bar{A}$ with edge basis functions described in the last section and

letting $\bar{W} = \bar{N}_i^e$, $i = 1,2,...m$, where m is the number of edges in an element, results in the

following matrix equation:

$$\left[K^e\right]\cdot\left[A^e\right] = \left[S^e\right] \tag{4.21}$$

This is the finite element equation at the element level. The coefficients of the stiffness

matrix and the load vector are evaluated using the following relationships:

$$K_{ij}^e = \iiint_{\Omega^e}\left[\left(\nabla \times \bar{N}_i^e\right)\frac{1}{\mu}\left(\nabla \times \bar{N}_j^e\right) + j\omega\sigma\bar{N}_i^e\cdot\bar{N}_j^e\right]dV \tag{4.22}$$

$$S_i^e = \iiint_{\Omega^e}\bar{J}_s\cdot\bar{N}_i^e dV + \iint_{S_i^e}\left(\bar{H}\times\hat{n}\right)\cdot\bar{N}_i^e dS \tag{4.23}$$

$$i, j = 1,2,...m$$

The following global linear system is then obtained by assembling all the element level

systems.

$$\left[K\right]\cdot\left[A\right] = \left[S\right] \tag{4.24}$$

The above $\bar{A}$ formulation considers the homogeneous Dirichlet condition. The more

general inhomogeneous Dirichlet condition will be discussed in the next section. The $\bar{A}$

formulation is employed here for two reasons. First, with edge elements, the $\bar{A}$ formulation

is equivalent to $\bar{A}$-V or $\bar{A}$-V-ψ formulation but the number of unknowns is less [67];

Second, we will see later that the calculation of coil impedance in NDE applications is very

simple with $\bar{A}$ formulation implemented using edge elements.

4.4 The Gauge Condition for Edge Elements

In last section's $\bar{A}$ formulation, the curl of $\bar{A}$ is specified as the magnetic flux

density. According to Helmholtz's theorem, a vector field is uniquely determined only if

both its curl and divergence are specified. Consequently, the $\bar{A}$ formulation as denoted by equations (4.14)-(4.16) does not provide a unique solution. On the other hand, consider equation (4.14). In the non-conducting region, $\sigma = 0$. Consequently, the gradient of an arbitrary scalar function can be added freely to the vector potential $\bar{A}$ without affecting the equality between the left hand side and right hand side. This fact results in a singular stiffness matrix in equation (4.24). Thus, the rank of the stiffness matrix is less than the number of unknowns. The global linear system (4.24) is an underdetermined system, which usually possesses more than one solution. It's very difficult and computationally expensive to solve such a system. The best way to deal with the non-uniqueness problem is to introduce an appropriate gauge condition to fix the arbitrariness of $\bar{A}$.

The Coulomb gauge, $\nabla \cdot \bar{A} = 0$, introduced in section 2.7, can be employed to fix the additional degrees of freedom associated with the magnetic vector potential. This gauge condition is consistent with the spirit of node based finite elements. Recall the following vector identity,

$$\nabla \times \nabla \times \bar{A} = \nabla\left(\nabla \cdot \bar{A}\right) - \nabla^2 \bar{A}$$

By setting $\nabla \cdot \bar{A} = 0$, the curl-curl operator becomes the vector Laplacian (Piecewise constant magnetic permeability μ is assumed) and $\bar{A}$ is decomposed into its three Cartesian components. In this way, $\bar{A}$ is decomposed into three scalars. However, it is difficult to impose this gauge condition on edge elements.

A different type of gauge condition, which prescribes the vector component along the direction determined by an arbitrary vector field which does not possess any closed field

lines, has been used in association with the edge elements [24,67-69]. This component can be specified freely without affecting the physical problem. For simplicity, let

$$\bar{A} \cdot \bar{T} = 0 \tag{4.25}$$

where $\bar{T}$ is an arbitrary non-vanishing vector field which does not possess any closed field lines. With the help of tree and co-tree decomposition from graph theory, this gauge condition can be imposed in a natural way. Before we see this, it is necessary to discuss two concepts from graph theory first.

The first concept is the so-called tree and co-tree separation. A finite element mesh can be viewed as a connected graph, which is defined as a set of nodes and branches, denoted as $G(V, E)$, where V is the set of nodes and E is the set of branches or edges. A spanning tree of the graph G is a connecting subgraph $T \subset G$, which connects all the nodes but does not include any closed loops. A tree of G is denoted as $G^T(V, T)$, where T is the set of branches forming the tree. Once a tree is specified for a graph, all the remaining branches form a co-tree, denoted as $G^C(V_C, C)$, where C is the set of co-tree branches. Fig 4.4-(a) and (b) show a graph and a tree of the graph. (c) and (d) show a 3D finite element mesh and a tree of the mesh. Obviously, a graph may have more than one tree. So the decomposition of branches into tree and co-tree is not unique. Let N_V be the number of nodes in a graph $G(V, E)$, N_E be the number of edges, N_T be the number of tree branches, and N_C be the number of co-tree branches. From graph theory,

$$N_T = N_V - 1$$
$$N_C = N_E - N_V + 1 \tag{4.26}$$

The second concept from graph theory is the independent loop. Suppose a tree is identified for a graph. Then adding any co-tree branch to the tree forms a closed loop, in which there is only one co-tree edge and all other edges are tree branches. Given a tree, there exists one and only one such loop for every co-tree edge. This loop is called the independent loop. Fig 4.5 shows two examples of independent loops for the graph shown in Fig 4.4 (a). Interested readers may refer to [81] for details on graph theory. An algorithm was proposed by Hale to identify all the trees of a general graph [82]. This algorithm can be used to search a tree of a finite element mesh.

Now, consider the gauge condition (4.25). Since a finite element mesh can be viewed as a graph, the vector field $\bar{T}$ in equation (4.25) can be chosen as a vector which is along a tree of the finite element mesh. Then the requirement that $\bar{T}$ does not possess any closed field lines is satisfied. Suppose a tree has been specified for a finite element mesh. Let E be the set of all edges in the mesh and E has been divided into a set of tree edges T and a set of co-tree edges C. Then a vector field $\bar{A}$ is divided into the summation of a tree field and a co-tree field accordingly.

$$\bar{A} = \sum_e A_e \bar{N}_e$$
$$= \underbrace{\sum_{e \in T} A_e \bar{N}_e}_{\bar{A}_T} + \underbrace{\sum_{e \in C} A_e \bar{N}_e}_{\bar{A}_C} \tag{4.27}$$

The first term represents the field restricted only on the trees of the finite element mesh, called the tree field, denoted as $\bar{A}_T$. The second term is the co-tree field $\bar{A}_C$. Webb [62] showed that an arbitrary co-tree field has an interesting property: $\nabla \times \bar{A}_C \neq 0$ unless $\bar{A}_C$ is identically zero. $\bar{A}_C$ can be split into two parts:

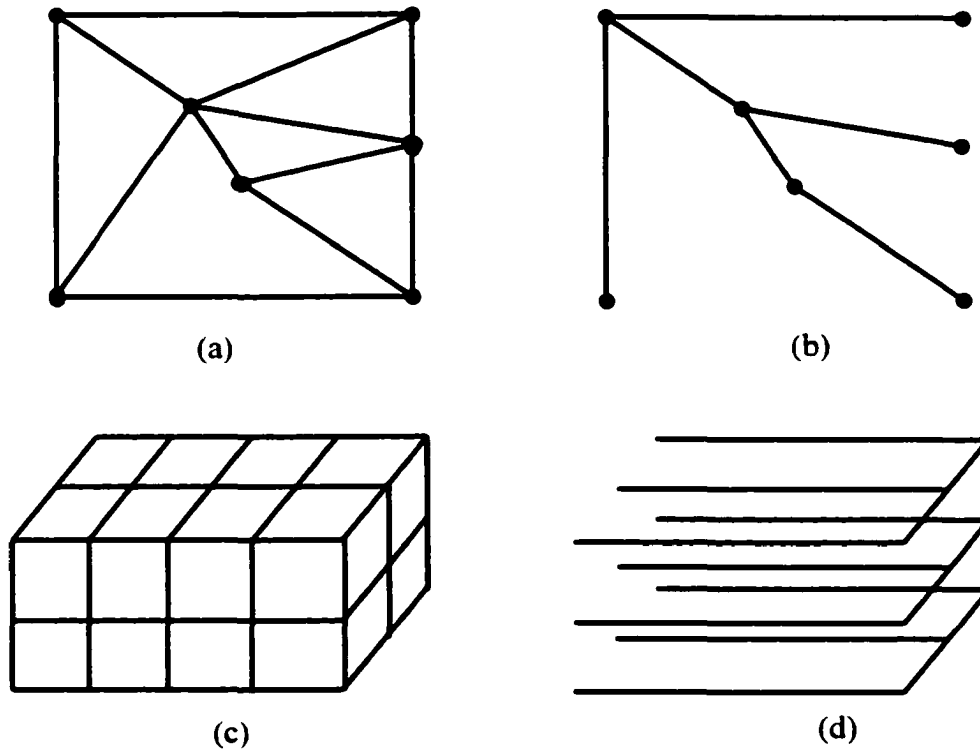Fig 4.4 Graphs and trees
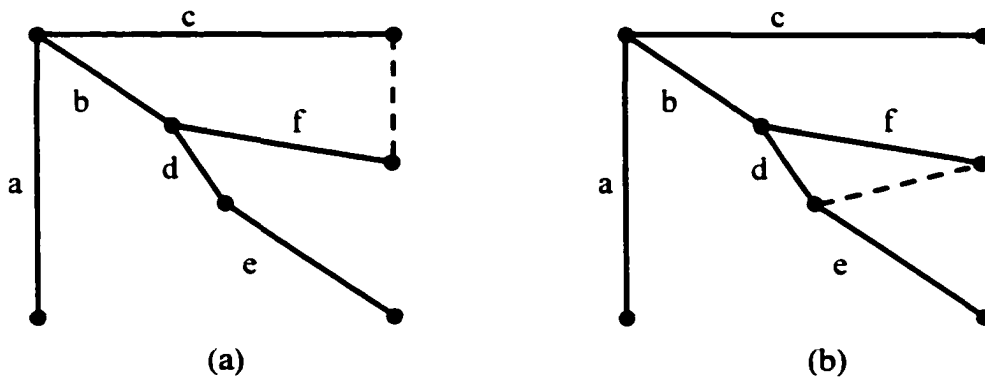(b) is a tree specified for the graph in (a). (d) is a tree specified for the graph in (c)

Fig 4.5 Independent loops
Edge a, b, c, d, e, and f is a tree of the graph shown in Fig 4.4 (a). The dashed edges are co-tree edges added to the tree. In (a), the added co-tree edge forms a closed loop with c, b, and f. In (b) the added co-tree edge forms a closed loop with f and d.

$$\bar{A}_C = \sum_{c \in C} A'_{1c} \bar{N}_c + \sum_{c \in C} A_{2c} \bar{N}_c$$

Substituting the above equation back to equation (4.27) results in

$$\bar{A} = \bar{A}_1 + \bar{A}_2 \tag{4.28}$$

$$\bar{A}_1 = \sum_{c \in T} A_{1c} \bar{N}_c + \sum_{c \in C} A'_{1c} \bar{N}_c \tag{4.29}$$

$$\bar{A}_2 = \sum_{c \in C} A_{2c} \bar{N}_c \tag{4.30}$$

where the A'_{1c} associated with each co-tree branch is determined so that $\nabla \times \bar{A}_1 = 0$.

Suppose k is a co-tree branch and L_k is its independent loop. A'_{1k} is simply determined by the following equation,

$$\oint_{L_k} \bar{A}_1 \cdot d\bar{l} = A'_{1k} + \sum_{c \in L_k} A_{1c} = 0 \tag{4.31}$$

Note: in L_k, the only co-tree branch is k and all other branches in this loop are tree branches. Equation (4.31) simply means that A'_{1k} is just the negative sum of the tree filed along the independent loop. Since there is one and only one such independent loop for every co-tree branch, A'_{1k} is uniquely determined by the A_{1c}'s. Therefore $\bar{A}_1$ is made curl free. It can, therefore, be expressed as the gradient of a scalar function. Then equation (4.28) becomes

$$\bar{A} = \bar{A}_2 + \nabla w \tag{4.32}$$

Actually, it has been shown that $\bar{A}_1$ is equivalent to ∇w, where $w \in W$ is an arbitrary scalar function [67] and W is the functional space spanned by the node basis functions, i.e.

$$W = \left\{ w \,\middle|\, w = \sum_{n \in V} w_n \bar{N}_n \right\}$$

Therefore, with the help of tree and co-tree decomposition, $\bar{A}$ is separated into a co-tree field

which satisfies $\nabla \times \bar{A}_2 \neq 0$ and the gradient of a scalar function.

In $\bar{A}$ formulation of eddy current problems, the magnetic vector potential $\bar{A}$ is arbitrary to within the gradient of a scalar function. Letting $\nabla w = 0$ in equation (4.32) eliminates the arbitrariness of $\bar{A}$. From the above analysis, setting $\nabla w = 0$ can be done by setting $\bar{A}_T = 0$. Suppose the stiffness matrix is partitioned according to the tree and co-tree separation,

$$\begin{bmatrix} K_{CC} & K_{CT} \\ K_{TC} & K_{TT} \end{bmatrix} \cdot \begin{bmatrix} A_C \\ A_T \end{bmatrix} = \begin{bmatrix} S_C \\ S_T \end{bmatrix} \tag{4.33}$$

Setting $\bar{A}_T = 0$, equation (4.33) becomes

$$[K_C] \cdot [A_C] = [S_C] \tag{4.34}$$

This equation has a unique solution, which is $\bar{A}_2$. Since $\bar{A}_1$ contributes nothing to the line integral of $\bar{A}$ along each of the independent loops, i.e.

$$\oint_{L_k} \bar{A} \cdot d\bar{l} = \oint_{L_k} \bar{A}_2 \cdot d\bar{l} = A_{2k}, \quad k = 1,2,\dots N_c \tag{4.35}$$

the kth component of $\bar{A}_2$ is actually the line integral of $\bar{A}$ along the kth independent loop. Note

$$\oint_{L_k} \bar{A} \cdot d\bar{l} = \sum_{c \in L_k} A_c$$

Substituting this equation back into Equation (4.35) gives a relation between the co-tree field $\bar{A}_C$ and the tree field $\bar{A}_T$. It can be expressed in matrix form,

$$[A_C] = [A_2] - [R] \cdot [A_T] \tag{4.36}$$

where matrix $[R]$ is a $N_C \times N_T$ incidence matrix. Its rows correspond to the N_C co-tree

branches and its columns correspond to the N_T tree branches. If a tree branch appears in the

k-th independent loop and its tangential direction is consistent with the circulation direction,

a "+1" appears in the corresponding column of k-th row. If the directions are opposite to

each other, then a "-1" appears. If a tree branch is not included in the independent loop at all,

a "0" appears in the position.

In summary, the global linear system (4.33) can be solved using the following

procedure:

1. Set $\bar{A}_T = 0$ and solve the linear system (4.34). The solution is $\bar{A}_2$.

2. Next, find out the relation between $[A_C]$ and $[A_r]$ using equation (4.36).

3. Substitute the relation into the system equation (4.33), solve the resulting linear

system and get the tree field $[A_T]$.

4. Substitute $[A_T]$ back to equation (4.36) to get $[A_C]$.

Once $\bar{A}$ is solved, the eddy current density can be obtained using the following formula

$$\bar{J} = -j\omega\bar{A} \qquad (4.37)$$

In many situations, not all the four steps are necessary. Sometimes, only step 1 is

needed. First, consider the magnetic flux density $\bar{B}$.

$$\bar{B} = \nabla \times \bar{A} = \nabla \times (\bar{A}_1 + \bar{A}_2) = \nabla \times \bar{A}_2 = \sum_k A_{2k}\nabla \times \bar{N}_k \qquad (4.38)$$

This shows that $\bar{B}$ can be calculated from $\bar{A}_2$ only, which is the solution of linear system

(4.34). Next, consider the coil impedance

$$Z = -j\omega\frac{\oint \bar{A}\cdot d\bar{l}}{I_s} = -j\omega\frac{\oint \bar{A}_1\cdot d\bar{l} + \oint \bar{A}_2\cdot d\bar{l}}{I_s} = -j\omega\frac{\oint \bar{A}_2\cdot d\bar{l}}{I_s}$$

The above formula exploits the fact $\nabla \times \bar{A}_1 = 0$; I_S is the current of the coil. We have

known from equation (4.10) that the unknowns of the global linear system are actually the

line integral of $\bar{A}$ along edges. The above formula, therefore, reduces to

$$Z = -j\omega \frac{\sum\limits_{k \in C} A_{2k}}{I_S} \qquad (4.39)$$

where C refers to the set of branches forming the coil. Actually, only co-tree branches in coil

C contributes to the summation in equation (4.39), because $\bar{A}_2$ is restricted to co-tree

branches only. Therefore, if we are just interested in the distribution of magnetic flux density

or coil impedances, then only equation (4.34) needs to be solved. For efficiency, all the tree

branches can be discarded at the assembly stage. This greatly reduces the storage

requirement and computation effort.

We know that the Dirichlet condition specifies the normal component of magnetic

flux density on boundary S_1. Albanese and Rubinacci [68] showed that the Dirichlet

conditions could be easily imposed with the help of tree and co-tree separation. Suppose

$\bar{B} \cdot \hat{n} = b$ is imposed on S_1. View S_1 as a subgraph of the finite element mesh. Select a tree

such that all the tree branches on S_1 forms a tree of the graph S_1. Then pick up an arbitrary

co-tree branch A_k^C from S_1. Its independent loop L_k must be on S_1. Perform the following

operation on L_k.

$$\oint_{L_k} \bar{A} \cdot d\bar{l} = \iint \bar{B} \cdot \hat{n} dS$$

Note

$$\oint_{L_k} \bar{A} \cdot d\bar{l} = \sum_{j \in L_k} A_j = A_k^C + \sum_{j \in L_k} A_j^T$$

$\bar{A}_T = 0$ has been set in step 1 of the solution process. This implies that all the degrees of

freedom associated with tree branches vanish. So A_k^C can be obtained from the formula,

$$A_k^C = \iint \bar{B} \cdot \hat{n} dS \qquad (4.40)$$

Therefore, the normal component of magnetic flux density on Dirichlet boundary is imposed

on the degrees of freedom associated with co-tree branches. This explains why this kind of

boundary condition is termed Dirichlet condition.

4.5 The Edge Element Model Verification

This section presents numerical results of three computation examples. The first two

examples are magnetostatic problems and the third one is an eddy current problem. Letting

the frequency $\omega = 0$, equation (4.14) reduces to

$$\nabla \times \frac{1}{\mu} \nabla \times \bar{A} = \bar{J}_s \qquad (4.41)$$

This is the governing equation for magnetostatic problems. Albanese and Rubinacci [68]

showed that equation (4.41), together with the gauge condition (4.25), has a unique solution.

Therefore, the developed $\bar{A}$ formulation can be used in magnetostatic problems simply by

setting $\omega = 0$.

Problem 1. Calculate the magnetic field generated by an infinitely long cylindrical

conductor carrying a DC current I_0. The radius of the conductor is $r = a$ and its magnetic

permeability is μ.

This is a magnetostatic problem. Fig 4.6 (a) shows the geometry of the problem. The

analytical solution can be obtained using Gauss's law. The magnetic field intensity is given

in cylindrical coordinate system

$$H_\varphi = \begin{cases} \dfrac{I_0 r}{2\pi a^2} & r \leq a \\ \dfrac{I_0}{2\pi r} & r > a \end{cases}$$

$$H_r = 0, \quad H_z = 0$$

The magnetic field does not have any components along the radial and axial directions. The

field line is along the circumferential direction. Within the conductor, the field value is

proportional to the radial distance r from the symmetric axis; and outside the conductor the

field value is inverse proportional to r, as shown in Fig 4.7.

Since the conductor is infinitely long, the problem can be formulated as a 2D problem

mathematically. Here it is solved as a 3D problem using the edge element code. The

solution domain is a cylindrical volume: $r \leq r_{max}$, and $z_{min} \leq z \leq z_{max}$. Fig 4.6 (b) shows an

axisymmetric plane of the solution domain. Because of the symmetry, only a quarter of the

entire domain is considered in numerical computation. Fig 4.8 (a) shows the discretized

solution domain (the finite element mesh). The parameters are:

$$a = 2\,mm, \quad r_{max} = 10\,mm, \quad z_{min} = 0\,mm, \quad z_{max} = 2\,mm$$

Fig 4.8 (b) shows a tree of the mesh. The distribution of the computed magnetic field

intensity in a plane $z = $ constant is demonstrated in Fig 4.9. It can be seen that the magnetic

field is in the circumferential direction. The error of the finite element solution is

characterized by the quantity:
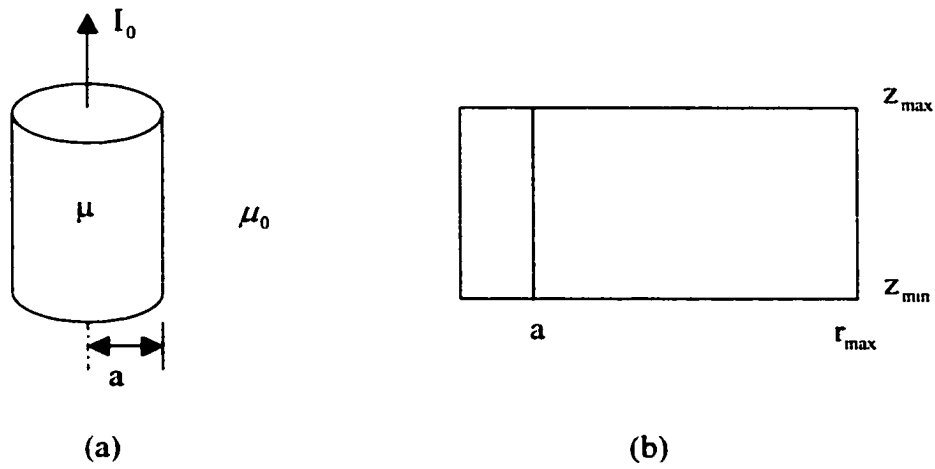
Fig 4.6 The geometry and solution domain of Problem 1
(a) shows the geometry and (b) shows an axisymmetric plane of the solution domain
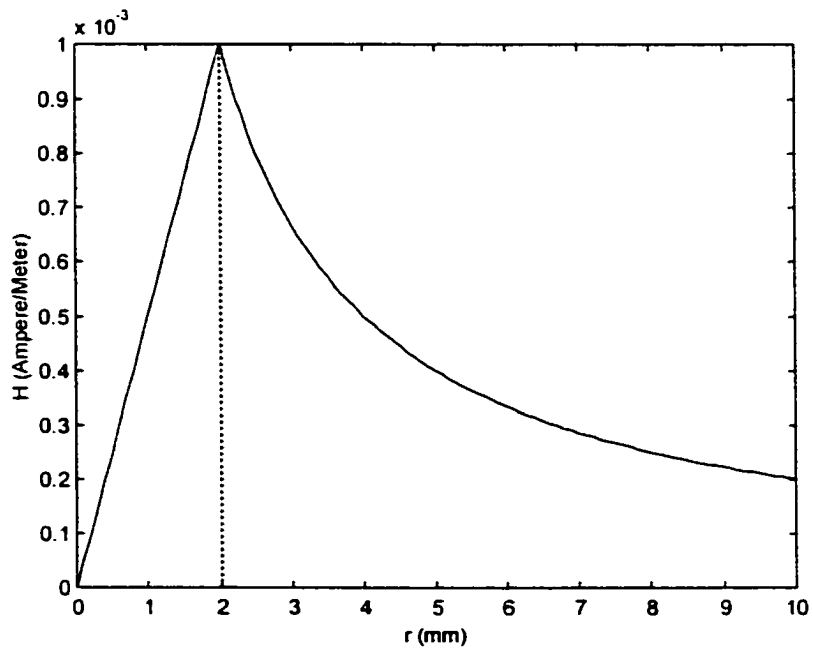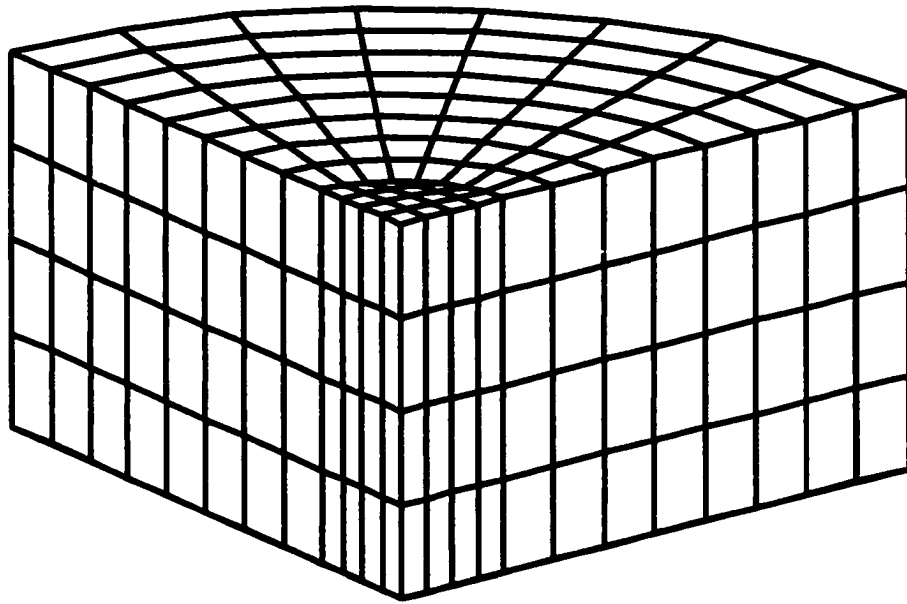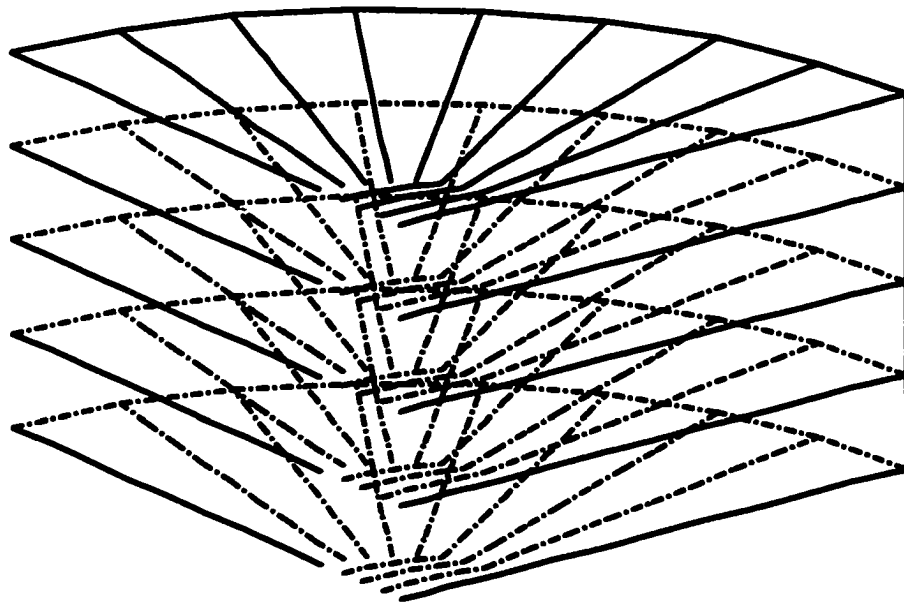

Fig 4.7 The Analytical Solution of H_φ in Problem 1

(a)

(b)

Fig 4.8 The finite element mesh of Problem 1 and a tree for it
(a) shows the finite element mesh of Problem 1 (front view). (b) shows a tree of the finite element mesh.

The Distribution of Magnetic Field Intensity
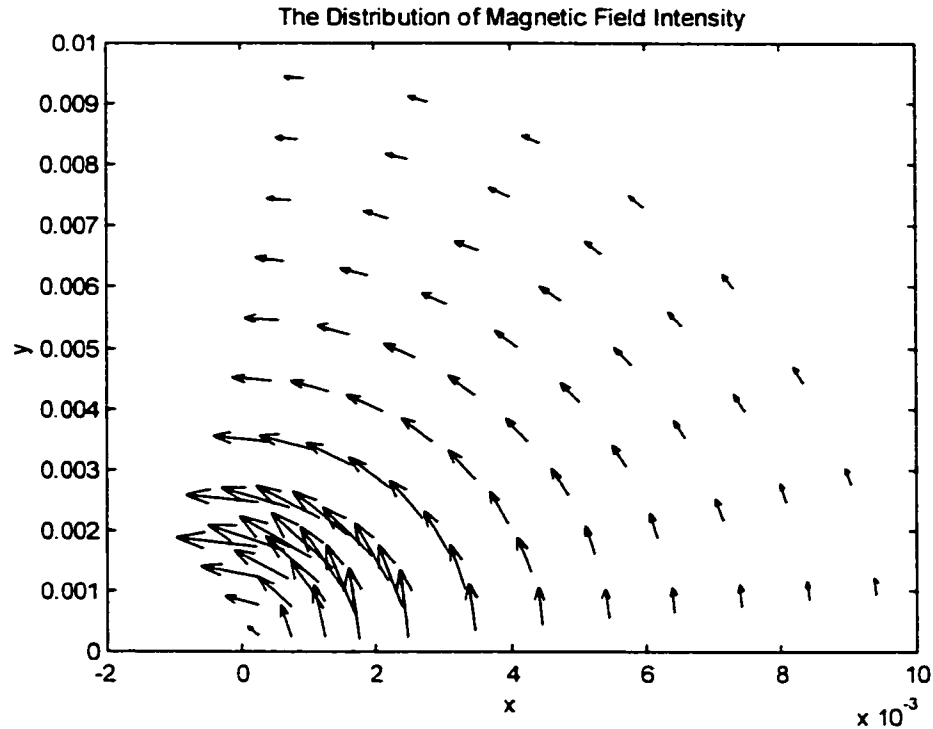
Fig 4.9 The distribution of $\bar{H}$ in a $z = \text{const}$ plane for Problem 1

$$\max_i \left\{ \left| \frac{H_\varphi^{(n)} - H_\varphi^{(0)}}{H_\varphi^{(0)}} \right|, i = 1,2,\ldots \text{NEL} \right\}$$

where NEL is the number of elements in the mesh. The superscript (n) denotes the numerical

solution while (0) denotes the analytical solution. It describes the maximum relative error of

the circumferential component compared with the analytical solution. The error values are

listed in table 4.1 for different mesh sizes. As the number of elements increases, the relative

error decreases.

Problem 2. Calculate the self-inductance per unit length of an infinitely long

solenoid.

For an infinitely long solenoid, the magnetic flux density inside the solenoid is

$B = \mu I n$

Table 4.1 Relative error of H_φ in Problem 1

Mesh		$\max\limits_i\left\{\left|\dfrac{H_\varphi^{(n)} - H_\varphi^{(0)}}{H_\varphi^{(0)}}\right|\right\}$
Number of Elements	Number of unknowns	
320	592	2.73%
1280	2304	1.90%
5120	9088	1.81%

where μ is the magnetic permeability of the material inside the solenoid, I is the current and n

is the number of turns per unit length. The direction of the magnetic field is along the axial

direction of the solenoid. Outside the solenoid, the magnetic filed is zero everywhere. The

self-inductance per unit length is

$$L_0 = \mu n^2 S,$$

where S is the cross-sectional area of the solenoid.

The inductance can be calculated using the formula

$$L = \frac{2W_m}{I^2}$$

where W_m is the magnetic energy stored in the magnetic field

$$W_m = \frac{1}{2}\int_\Omega \bar{B}\cdot\bar{H}dV = \frac{1}{2}\int_\Omega \frac{B^2}{\mu}dV$$

The magnetic flux density is calculated using the edge element code.

The other method to calculate the self-inductance involves using the formula

$$L = \frac{\Psi}{I} = \frac{n\oint_C \bar{A}\cdot d\bar{l}}{I} = \frac{n\sum\limits_{j\in C} A_j}{I}$$

where ψ is the flux linkage and C represents the coil. The dimensions of the solenoid are:

inner radius: 0.01m, outer radius: 0.0101m

number of turns: 200, permeability μ_r : 100

Then $L_0 = 1.5791 \times 10^{-3}$ H/m. The numerical results of L and the relative error compared

with L_0 are listed in Table 4.2. As the mesh size decreases, the numerical results approach

the analytical solution.

Table 4.2 Numerical values of the self-inductance L and its relative error

| Mesh		L	$\left\lvert \dfrac{L - L_0}{L_0} \right\rvert$
Number of Elements	Number of Unknowns		
640	844	1.5198×10^{-3}	3.75%
1408	1844	1.5627×10^{-3}	1.04%
3328	4324	1.5739×10^{-3}	0.33%
8704	11204	1.5768×10^{-3}	0.15%

Problem 3. The JSAEM (Japan Society for Applied Electromagnetics and

Mechanics) benchmark problem 1 [83,84] involves the calculation of the impedance change

of a pancake coil when placed over a circular conducting plate. Fig 4.10 shows the geometry

of the problem and the pancake coil. Other coil parameters are listed in Table 4.3. The

impedance change refers to the difference between the impedance of the coil over the

conducting plate and the impedance of the same coil in air.

$$\Delta Z = Z\big|_{\text{over the conducting plate}} - Z\big|_{\text{in air}}$$

The problem geometry possesses axisymmetry. It can be formulated as a 2-

dimensional problem mathematically. Here, it is solved as a 3-dimensional problem. Fig

4.11 is an axisymmetric plane of the solution domain. Table 4.4-4.7 compares the measured
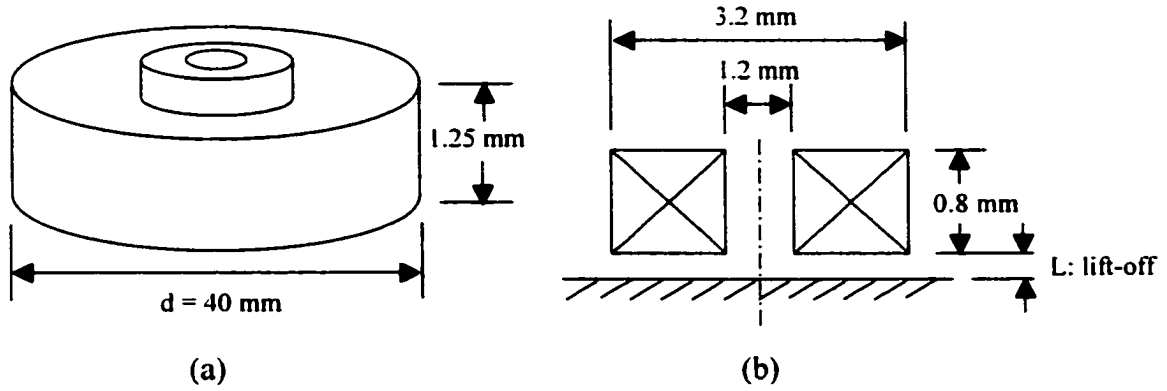
Fig 4.10 Problem 3 --- JSAEM benchmark problem No.1
(a) shows the geometry of the problem: a pancake type coil over a circular conducting plate. (b) shows the dimension of the pancake coil
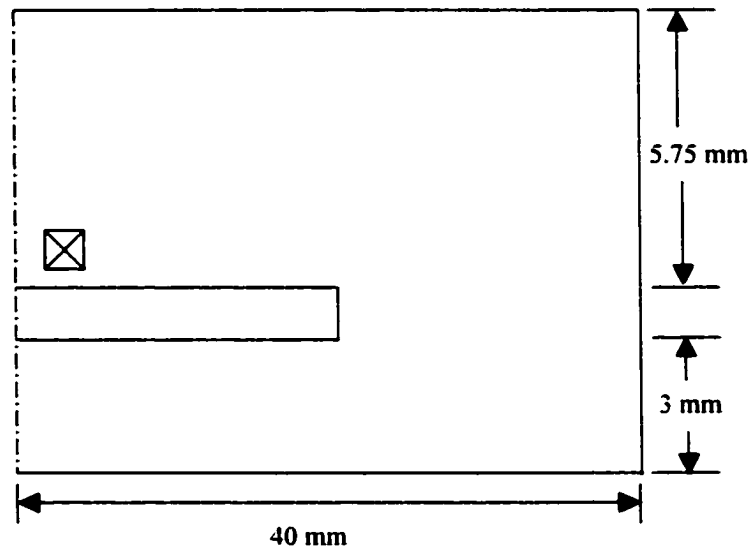
Fig 4.11 The solution domain of Problem 3 (An axisymmetric plane)

value of the real part of the impedance change ΔR, the imaginary part $\Delta \omega L$ and the

magnitude $|\Delta Z|$ with the corresponding numerical values under different combinations of

operating frequency and lift-off. In each table, the first row lists the experimental results

[85]. The second row lists the results from a finite difference code [86]. The third and fourth

rows list the results from a node based finite element code and an edge based finite element

code respectively [87]. The fifth, sixth and seventh row are the numerical results from the

edge element code obtained using three different mesh sizes. As the mesh size decreases, the

numerical results converge asymptotically. Comparing these results, it can be concluded that

these numerical results are basically comparable.

Table 4.3 Coil parameters for Problem 3

Current	$\frac{1}{140}$ A	
Number of Turns	140	
Frequency	150 kHz	300 kHz
Inner Diameter	1.2 mm	
Outer Diameter	3.2 mm	
Lift-off	0.5 mm	1.0 mm

4.6 Conclusions and Discussions

In summary, the $\bar{A}$ -formulation implemented with edge based finite elements has the

following advantages:

Table 4.4 Comparison of numerical and experimental results for Problem 3
Frequency: 150 kHz   Lift-off: 0.5 mm

		ΔR	ΔωL	ΔZ
Experiment (JSAEM)		1.0	-0.79	1.27
FDM (Technical Univ. of Szczecin)	Uniform Grid (Δr = Δz = 0.1mm)	1.154	-0.846	1.431
Node FEM (Univ. of Tokyo)		1.04	-0.83	1.33
Edge FEM (Tohoku Univ.)		1.05	-0.85	1.35
Edge FEM (Iowa State Univ.)	nel 2816 nunk 5329	0.985	-0.720	1.220
Edge FEM (Iowa State Univ.)	nel 6656 nunk 12641	1.026	-0.753	1.272
Edge FEM (Iowa State Univ.)	nel 13056 nunk 24913	1.045	-0.786	1.308

Table 4.5 Comparison of numerical and experimental results for Problem 3
Frequency: 300 kHz   Lift-off: 0.5 mm

		ΔR	ΔωL	ΔZ
Experiment (JSAEM)		2.22	-2.71	3.50
FDM (Technical Univ. of Szczecin)	Uniform Grid (Δr = Δz = 0.1mm)	2.671	-3.063	4.064
Node FEM (Univ. of Tokyo)		2.42	-2.83	3.72
Edge FEM (Tohoku Univ.)		2.42	-2.90	3.78
Edge FEM (Iowa State Univ.)	nel 2816 nunk 5329	2.334	-2.569	3.471
Edge FEM (Iowa State Univ.)	nel 6656 nunk 12641	2.426	-2.684	3.618
Edge FEM (Iowa State Univ.)	nel 13056 nunk 24913	2.456	-2.772	3.704

Table 4.6 Comparison of numerical and experimental results for Problem 3
Frequency: 150 kHz   Lift-off: 1.0 mm

		ΔR	$\Delta \omega L$	ΔZ
Experiment (JSAEM)		0.41	-0.48	0.63
FDM (Technical Univ. of Szczecin)	Uniform Grid ($\Delta r = \Delta z = 0.1$mm)	0.528	-0.469	0.706
Node FEM (Univ. of Tokyo)		0.48	-0.48	0.68
Edge FEM (Tohoku Univ.)		0.49	-0.49	0.69
Edge FEM (Iowa State Univ.)	nel 2816 nunk 5329	0.426	-0.380	0.571
Edge FEM (Iowa State Univ.)	nel 6656 nunk 12641	0.445	-0.397	0.596
Edge FEM (Iowa State Univ.)	nel 13056 nunk 24913	0.449	-0.404	0.604

Table 4.7 Comparison of numerical and experimental results for Problem 3
Frequency: 300 kHz   Lift-off: 1.0 mm

		ΔR	$\Delta \omega L$	ΔZ
Experiment (JSAEM)		0.94	-1.47	1.74
FDM (Technical Univ. of Szczecin)	Uniform Grid ($\Delta r = \Delta z = 0.1$mm)	1.106	-1.584	1.903
Node FEM (Univ. of Tokyo)		1.00	-1.48	1.79
Edge FEM (Tohoku Univ.)		1.00	-1.51	1.81
Edge FEM (Iowa State Univ.)	nel 2816 nunk 5329	0.898	-1.237	1.528
Edge FEM (Iowa State Univ.)	nel 6656 nunk 12641	0.937	-1.293	1.597
Edge FEM (Iowa State Univ.)	nel 13056 nunk 24913	0.944	-1.310	1.615

1. The $\bar{A}$-formulation implemented with edge elements is equivalent to $\bar{A}$-V

   formulation. The node based $\bar{A}$-formulation has difficulty in dealing with

   discontinuities in conductivity. Although the $\bar{A}$-V formulation can be employed to

   solve the problem (see section 2.8), the introduction of an additional variable

   increases the complexity. Kameari [67] pointed out that the $\bar{A}$-formulation

   implemented with edge elements is equivalent to $\bar{A}$-V formulation, since the gradient

   of the scalar potential ∇V is assimilated into $\bar{A}$. With the help of tree and co-tree

   decomposition, the magnetic vector potential $\bar{A}$ can be separated into the sum of the

   gradient of an arbitrary scalar function and the remaining part.

2. The edge based $\bar{A}$-formulation is computationally more efficient. First, the scalar

   potential V is no longer needed. Next, compared with node based $\bar{A}$-formulation,

   the number of unknowns is less. The number of unknowns in edge elements is the

   number of co-tree branches while the number of unknowns for node elements is the

   number of nodes times 3. Generally, the less the number of unknowns, the less the

   storage and CPU time required.

3. Uniform treatment of both magnetostatic and quasistatic problems is possible. As

   shown in the last section, both the magnetostatic and quasistatic problems can be

   solved using the same formulation.

The $\bar{A}$-formulation has the following disadvantages:

1. The tree and co-tree separation affects iterative solvers. Different choices of a

   tree of the finite element mesh affects the solution of magnetic vector potential

   and has no effect on the computation of magnetic flux density or the coil

impedance. However, this may affect the condition number of the stiffness matrix, which results in poor convergence when iterative solvers are used [24].

2. The $\bar{A}$-formulation implemented in edge elements is inefficient in calculating the distribution of induced eddy current density. As discussed in section 4.4, all four steps described on page 63 are necessary in this case.

CHAPTER 5 AN ADJOINT EQUATION BASED METHOD FOR EDDY CURRENT NDE SIGNAL INVERSION

5.1. Introduction

Inverse problems in eddy current NDE applications are generally concerned with the task of characterizing the size, shape, and location of defects based on information contained in eddy current probe signals. Most of the approaches used in industry use a combination of signal processing and pattern recognition methods to establish a relationship between the geometric parameters defining the defect and specific features of the signals. This chapter presents a phenomenological approach that makes use of an edge element based finite element model to simulate the underlying physical process and a gradient based minimization algorithm to minimize the objective function so that a material distribution that results in a signal matching the measured signal in the least square sense is reached.

The evaluation of the gradient plays a critical role in a gradient based minimization algorithm. To evaluate the gradient of the objective function, each of the partial derivatives must be evaluated. Common methods call for solving the governing linear system once to calculate each of the partial derivatives. This makes the computation time prohibitively long in multi-dimensional optimization problems. An adjoint equation based method is presented to address the problem. Using the method of Lagrangian multipliers, all the derivatives required by the optimization algorithm could be found by solving the governing linear system only once. The method reduces the computation time for gradient computation significantly. It is used to characterize flaws in heat exchanger tubes from eddy current probe signals. Since the gradient method is a local technique, it tends to converge to a poorer

local minimum and produce a solution that depends on the starting trial solution. The

method as well as limitations of the technique is discussed in this chapter.

5.2 An Iterative Signal Inversion Scheme

An iterative signal inversion scheme based on gradient search is shown in Fig 5.1. It

employs a finite element forward model to simulate the underlying physical phenomenon and

predict the eddy current probe signal. The predicted signal is then compared with an input

signal obtained from actual measurements. If the mean squared error between the predicted

and the measured signals is not sufficiently small, the initial defect profile is updated and

then fed to the forward model. The newly calculated probe response is compared with the

measured signal again. This process continues until a defect profile that results in a signal

matching the measured input signal in the least square sense is reached. Such a defect

characterization procedure can be formulated as an optimization problem. A typical

optimization problem consists of four ingredients:

1. a set of state variables φ ;

2. a set of design parameters X;

3. an objective function $J(\varphi, X)$;

4. constraint equations $F(\varphi, X) = 0$.

In a defect characterization problem, the design parameters X are the parameters used to

describe defect profiles. Fig 5.2 and Fig 5.3 show a method of representing defect profiles

using isoparametric elements [75]. In Fig 5.2, an arbitrary 2 dimensional defect profile can

be mapped from an 8-node quadrilateral element. Therefore, the coordinates of the 8 nodes,
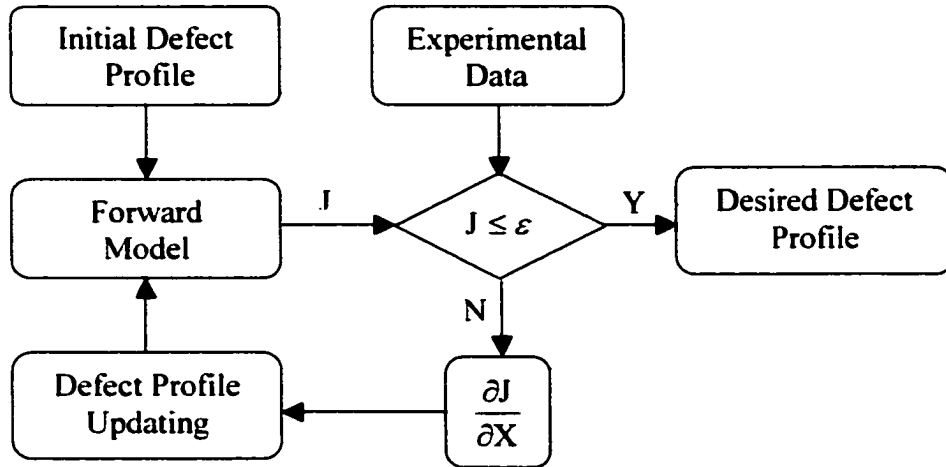
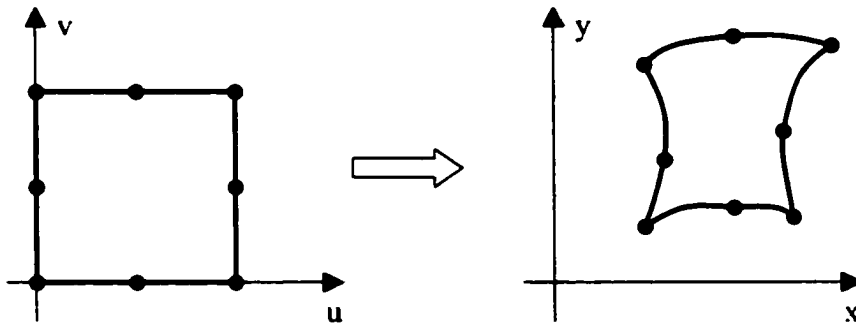Fig 5.1 An iterative signal inversion scheme based on gradient search

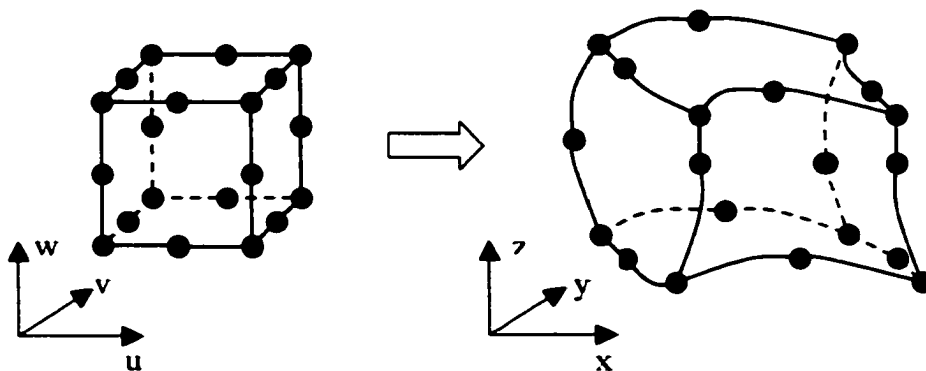Fig 5.2 An 8-node quadrilateral element representing a 2-D defect

Fig 5.3 A 20-node hexahedral element representing a 3-D defect

i.e. 16 parameters, uniquely determine a profile. Similarly, in Fig 5.3, a 3 dimensional defect

profile is represented with 20 nodes, or equivalently 60 parameters. These parameters can be

chosen as the defect characterization parameters. The choice of the state variable depends on

the forward model. The edge element based $\bar{A}$ formulation introduced in Chapter 4 is

employed to simulate the eddy current phenomenon in this work. Then the state variable φ

simply represents the (modified) magnetic vector potential. The constraint condition

imposed on the parameter set X and state variable φ is then the governing partial differential

equation (4.14). The discretized version, the finite element equation (4.24) is used here as

the constraint equation. The equation is written below with the unknown vector replaced by

the state variable φ,

$$F(\varphi, X) = [K] \cdot [\varphi] - [S] = 0 \tag{5.1}$$

The objective function should include the quantity that is minimized when the reconstructed

defect profile matches the desired one. Therefore the discrepancy between the predicted

signal and the measured signal should be reflected in the definition of the objective function.

Since the coil impedance is the most commonly measured test parameter in eddy current

problems, the objective function is defined as the least square error between the predicted

and desired impedances, as shown in the following equation:

$$J = \sum_{i=1}^{M} \left\| Z_i - Z_i^m \right\|^2 \tag{5.2}$$

where, M is the number of signal samples and the superscript m refers to the measured

impedance. Given the required four ingredients, the defect characterization problem can then

be stated as:

solve for a set of defect parameters X such that the objective function $J(\varphi, X)$ is

minimized, subject to the constraint equation $F(\varphi, X) = 0$.

Many approaches may be used to perform the minimization, or the updating of the forward

model. If the gradient of the objective function is available, it can be utilized to find a

minimum. In many cases, the gradient based method is possibly the most rapidly converging

approach. The procedure can be summarized as follows:

Starting with an initial defect parameter set $X^{(0)}$, for $n = 0,1,2,...$

1. Solve the constraint equation (5.1), and calculate the coil impedance and the
   objective function using equations (4.39) and (5.2) respectively.

2. Compute the gradient of the objective function ∇J and determine a step $\delta X^{(n)}$
   based on the gradient.

3. Update the defect parameters, $X^{(n+1)} = X^{(n)} + \delta X^{(n)}$.

This process relies on the gradient information to set the search direction and step. The

evaluation of the gradient is termed sensitivity analysis [58]. The performance as well as the

total computation effort depends heavily on the manner in which the gradient is computed.

The following section devotes attention to sensitivity analysis since it has a major impact on

the computation burden.

5.3 The Adjoint Equation Based Method

The gradient of the objective function with respect to the defect parameters ∇J can

be calculated from the constraint equation (5.1) and equation (5.2).

Let X be the set of defect characterization parameters and let its cardinality be m.

$$X = [x_1, x_2, \cdots, x_m]^T$$

$$\nabla J = \left[\frac{\partial J}{\partial x_1}, \frac{\partial J}{\partial x_2}, \cdots, \frac{\partial J}{\partial x_m} \right]^T$$

Using the chain rule,

$$\frac{\partial J}{\partial x_k} = \sum_j \frac{\partial J}{\partial \varphi_j} \cdot \frac{\partial \varphi_j}{\partial x_k} = \left[\frac{\partial J}{\partial \varphi} \right]^T \cdot \left[\frac{\partial \varphi}{\partial x_k} \right]$$

$$k = 1, 2, \cdots, m \qquad\qquad (5.3)$$

where,

$$\left[\frac{\partial J}{\partial \varphi} \right] = \left[\frac{\partial J}{\partial \varphi_1}, \frac{\partial J}{\partial \varphi_2}, \cdots, \frac{\partial J}{\partial \varphi_n} \right]^T$$

Since the objective function is a direct function of the coil impedance as given in equation

(5.2) and the impedance depends directly on the state variables (see equation (4.39)), the first

term in equation (5.3) is easy to calculate. The second term could be obtained by

differentiating equation (5.1), which results in the following equation,

$$[K] \cdot \left[\frac{\partial \varphi}{\partial x_k} \right] = - \left[\frac{\partial K}{\partial x_k} \right] \cdot [\varphi] \qquad\qquad (5.4)$$

To find the derivative of the state variable with respect to each of the defect parameters,

equation (5.4) has to be solved once for every component of the parameter set X. Since the

number of the parameters is large and the procedure needs to be carried out repeatedly, the

computational effort becomes excessive despite the fact that the coefficient matrix in

equation (5.4) remains the same for all parameters. Besides the above method, the finite

difference method represents another option for calculating the gradient approximately.

However, it suffers from problems due to round off error and the amount of computation is huge.

To perform the sensitivity analysis efficiently, an adjoint equation based method is used [56,64], which significantly reduces the computation time for calculating the gradient. Using the method of Lagrangian multipliers to enforce the constraint equation (5.1), the Lagrangian function is defined as,

$$L(\varphi, X, \Lambda) = J(\varphi, X) - \langle F(\varphi, X), \Lambda \rangle \tag{5.5}$$

where Λ is the set of Lagrangian multipliers. The stationary conditions of $L(\varphi, X, \Lambda)$ results in the following three equations:

$$\frac{\partial L}{\partial \Lambda} = 0 \Rightarrow F(\varphi, X) = 0 \tag{5.6}$$

$$\frac{\partial L}{\partial X} = 0 \Rightarrow \left[\frac{\partial F}{\partial X}\right] \cdot [\Lambda] = \left[\frac{\partial J}{\partial X}\right] \tag{5.7}$$

$$\frac{\partial L}{\partial \varphi} = 0 \Rightarrow [K]^\Gamma \cdot [\Lambda] = \left[\frac{\partial J}{\partial \varphi}\right] \tag{5.8}$$

Equation (5.6) is actually the constraint equation (5.1); Equation (5.7) is the optimality equation and equation (5.8) is the adjoint equation. Substituting the adjoint equation (5.8) and equation (5.4) into equation (5.5) results in the following formula for the evaluation of derivatives of the objective function.

$$\frac{\partial J}{\partial x_k} = [\Lambda]^\Gamma \cdot [K] \cdot \left[\frac{\partial \varphi}{\partial x_k}\right] = -[\Lambda]^\Gamma \cdot \left[\frac{\partial K}{\partial x_k}\right] \cdot [\varphi]$$

$$k = 1, 2, \cdots, m \tag{5.9}$$

In the above equation, the derivative of the stiffness matrix is calculated from the finite

element formulation, and the state variable φ is obtained by solving the constraint equation

(5.1). The set of Lagrangian multipliers $[\Lambda]$ is computed by solving the adjoint equation

(5.8). The left hand side of the adjoint equation is the transpose of the stiffness matrix, which

is a symmetric matrix. Consequently only a back substitution is needed to compute $[\Lambda]$ since

the stiffness matrix has been factorized in solving the constraint equation. More importantly,

once $[\Lambda]$ is solved, all the required derivatives can be calculated using the above formula

regardless of the number of defect parameters.

5.4 Defect Characterization In Heat Exchanger Tubes

Eddy current testing is widely used for inspecting heat exchanger tubes. Fig 5.4

shows the configuration of a typical application. A differential probe is used because of its

inherent simplicity and modest instrumentation requirements. It consists of two identical

coils. The output of a differential probe is the difference between the impedances of the two

coils. In Fig 5.4, the differential probe is stepped forward along the pipe and measurements

are taken at each step. If no defects exist inside the pipe wall, the impedances of the two

coils are identical and thus the differential probe output is zero. If a defect is present, the

impedances of the two coils are perturbed differently, since their positions relative to the

defect are different. When the probe passes by the defect area, a signal is generated. Fig 5.5

shows the impedance of the two coils and the probe output. The probe output signal contains

the information about the defect, such as its location, size and shape. The task of defect

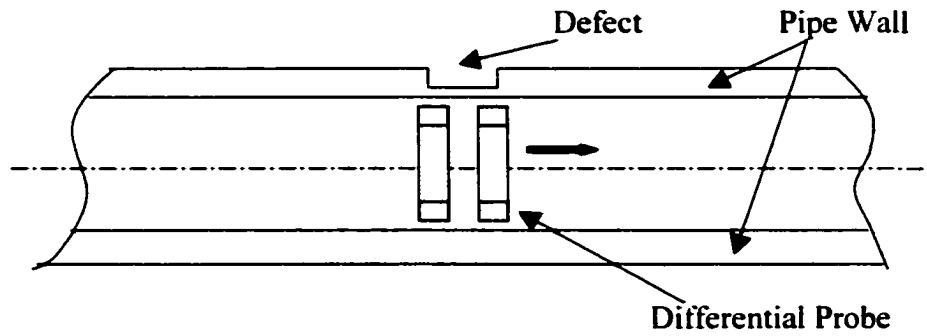characterization is to determine the defect information by analyzing the probe output.

Fig 5.4 A differential probe scanning a heat exchanger tube with a defect
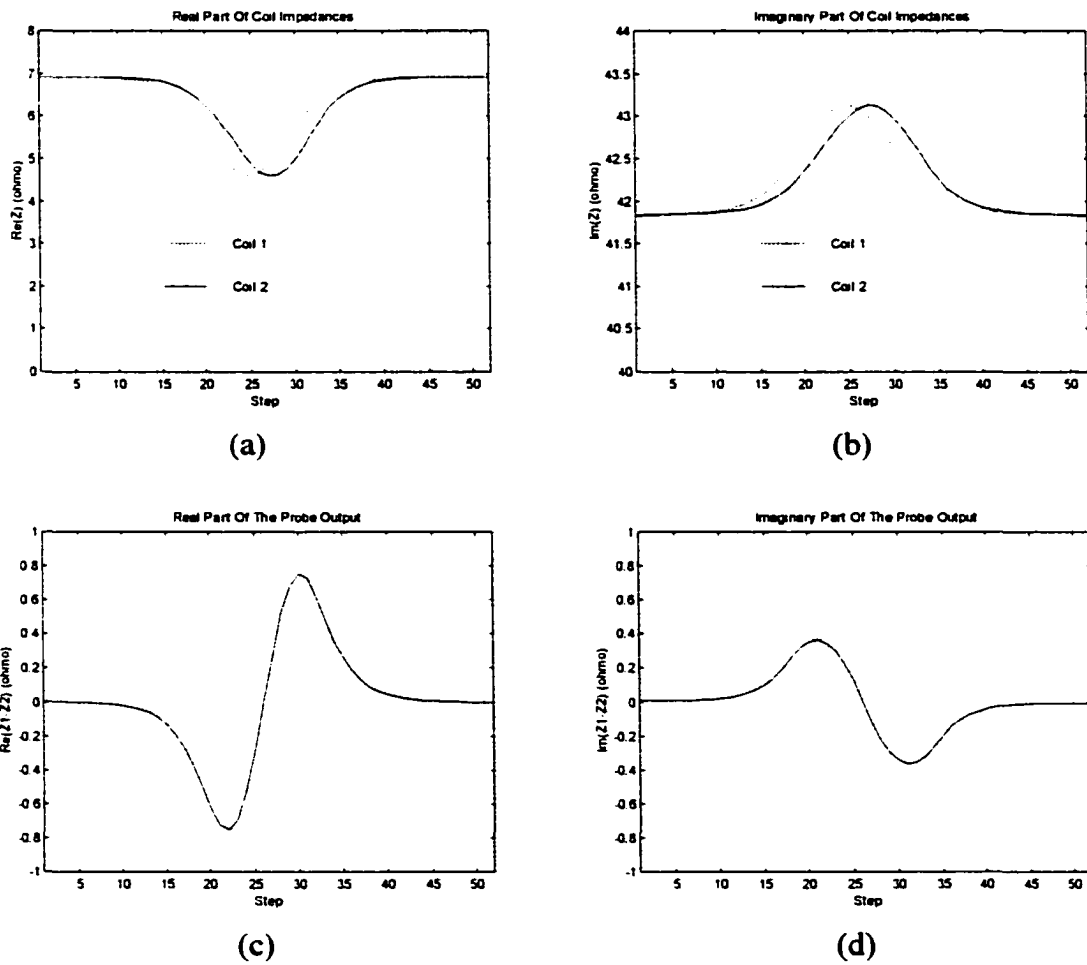inner diameter: 19.7mm, outer diameter: 22.2mm, tube wall material: inconel

Fig 5.5 Coil impedances and probe output of a differential probe
(a) and (b) are the real and imaginary parts of impedances of the two coils. (c) and (d)
are the real and imaginary parts of the probe output

Suppose 20 measurements are taken and the defect is represented by a 20-node

hexahedral element as shown in Fig 5.3. Then the cardinality of the defect characterization

parameter set is 60. If the conventional method introduced in the last section is used, the

number of back substitutions needed is 20×61 (1 for solving the constraint equation and 60

for the sensitivity analysis). If the adjoint equation based method is employed, the

corresponding number is 20×2 (1 for solving the constraint equation and 1 for solving the

adjoint equation). In the ideal case, the speed up is therefore 30.5. The actual speed up is

near 29 because of additional overhead. Consequently, the adjoint equation based method

reduces the amount of computation significantly for sensitivity analysis.

Since the differential probe is incapable of localizing a defect in the circumferential

direction, we limit our problem to one of estimating the depth profile of defects. Fig 5.6

shows an example of such a defect. In this case, the dimension and shape of the defect along

the circumferential and radial directions are fixed and the depth is a function of the axial

position. The defect profile is characterized by three depths at three axial positions: d_1 and

d_2 at the ends and d_3 at the midpoint. The gradient with respect to the 60 parameters can be

transformed into the gradient with respect to d_1, d_2, and d_3. The Broyden-Fletcher-

Goldfarb-Shanno (BFGS) algorithm is used to search for the minimum point of the objective

function [88]. Fig 5.7 shows six test cases. In each case, the initial guess, desired profile,

and reconstructed profile are shown in (i), and the value of the objective function vs. iteration

number is shown in (ii). The input signals are generated using the same forward model. The

algorithm reconstructs the depth profile with very good accuracy. A minimum is found
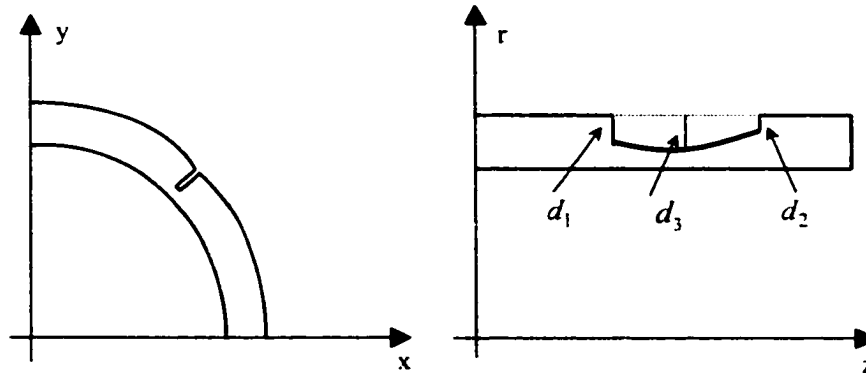
within 15 iterations.

Fig 5.6 A test defect geometry represented with 3 depths

5.5 Conclusions and Discussions

In the last section, a gradient based BFGS algorithm was used successfully to address

a simple eddy current signal inversion problem. We now, consider a relatively more

complex defect geometry shown in Fig 5.8. The defect profile is represented with 5 depths:

d_1, d_2, d_3, d_4, and d_5 in contrast to the previous example which had 3 depths. The same

minimization algorithm is applied to this case. The algorithm fails to reach an acceptable

minimum mean square error value. The procedure stops at a high value of the objective

function. When different initial profiles are used, the algorithm does not converge to a

unique minimum. Check the points where the procedure stops. The magnitude of the

gradient of the objective function at these stopping points is very low. Consequently, these

stopping points can be viewed as either stationary points or saddle points. In this case, the

minimization algorithm converges to either a local minimum or a saddle point. This is one of

the disadvantages associated with gradient search method. Hoole et al reported similar

problems [55]. The existence of multiple local minima is identified in their work too.
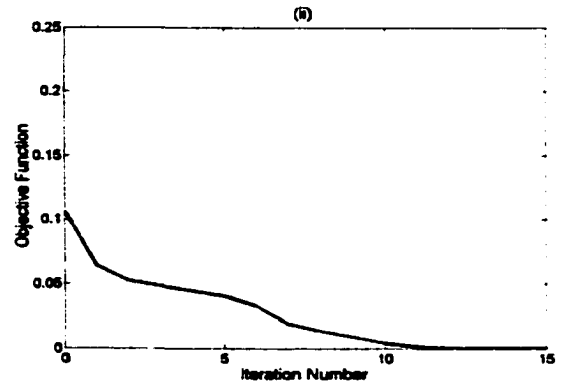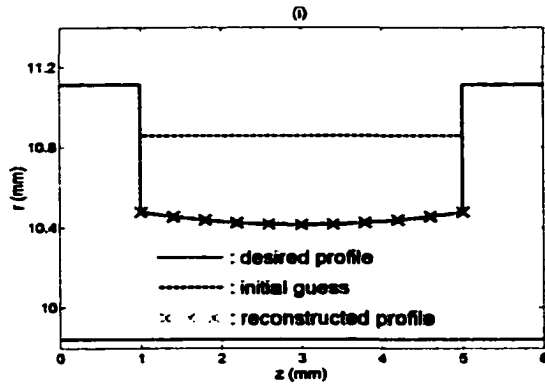
(a) $d_1 = 50\%$, $d_2 = 50\%$, $d_3 = 55\%$
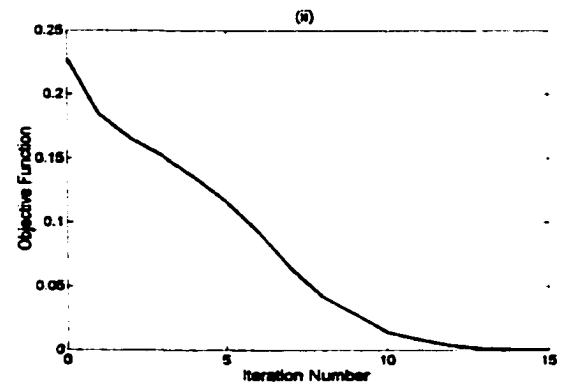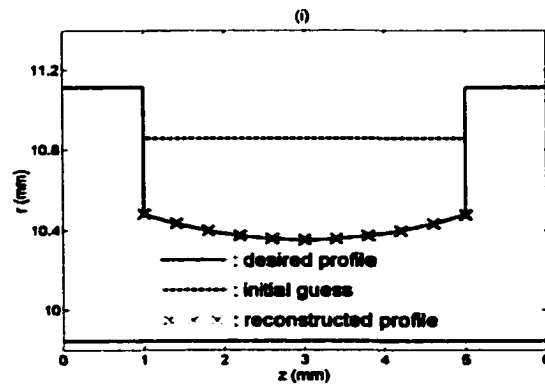
(b) $d_1 = 50\%$, $d_2 = 50\%$, $d_3 = 60\%$
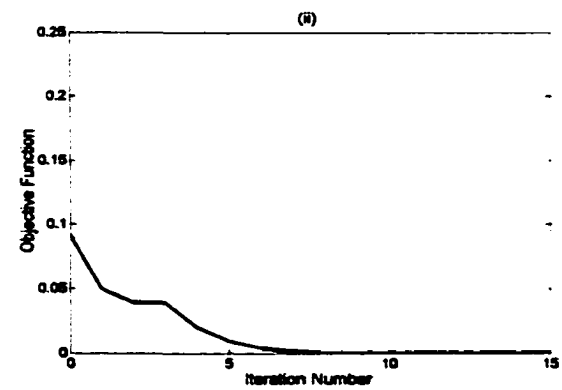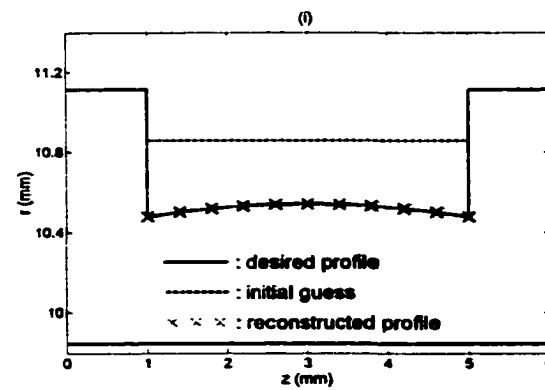
(c) $d_1 = 50\%$, $d_2 = 50\%$, $d_3 = 45\%$
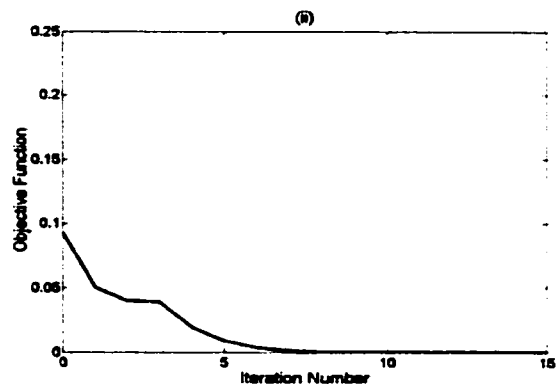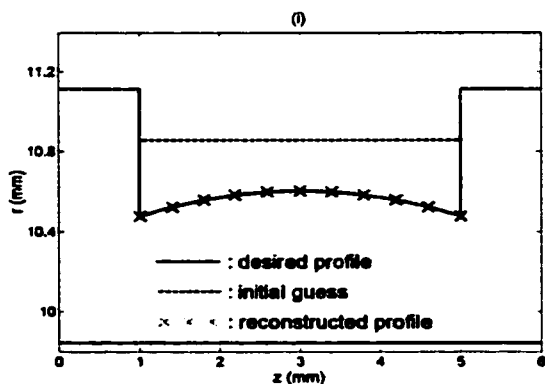
(d) $d_1 = 50\%$, $d_2 = 50\%$, $d_3 = 40\%$
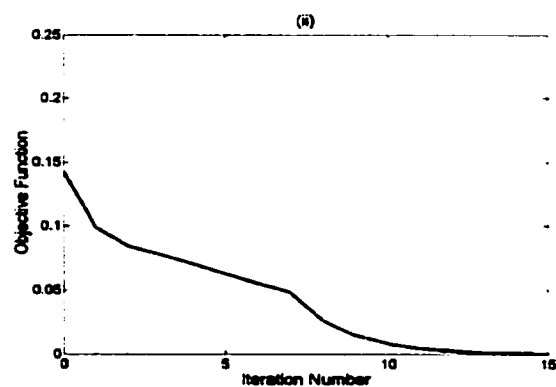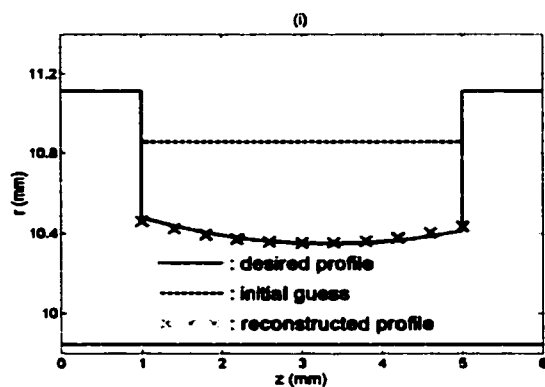
(e) $d_1 = 50\%$, $d_2 = 55\%$, $d_3 = 60\%$
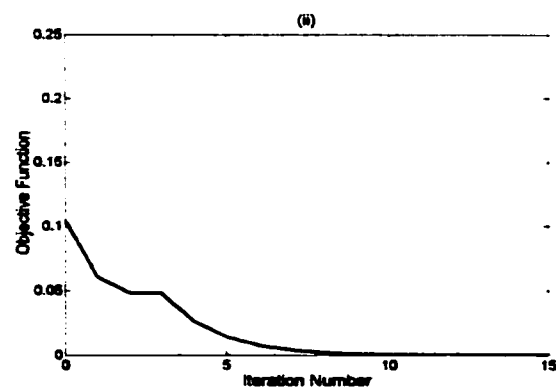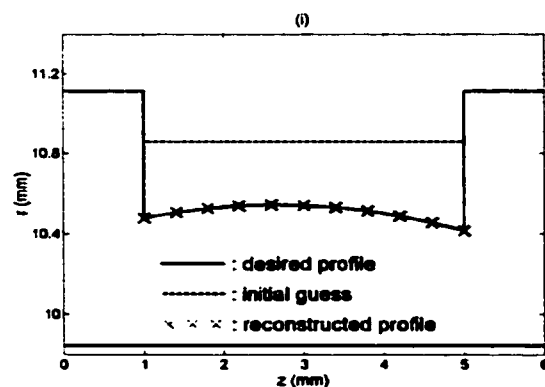
(f) $d_1 = 50\%$, $d_2 = 55\%$, $d_3 = 45\%$

Fig 5.7 Six defect characterization examples using gradient based method
In each case, (i) shows the desired profile, initial guess, and reconstructed profile. (ii) shows the convergence performance.
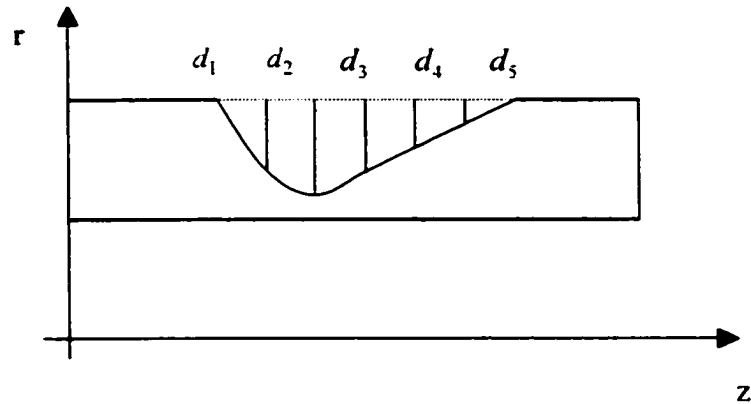
Fig 5.8 A defect geometry represented with 5 depths

The problem of multiple local minima can be partially solved by choosing a set of different initial profiles. The gradient search algorithm is then used to find out some of the local minima. A 'global' minimum is picked from these local minima according to the value of the objective function. However, such a scheme is not efficient, especially when numerous local minima are present. On the other hand, such a procedure would not be able to distinguish between stationary points and saddle points. Consequently, a global technique, which does not rely on the local property of the objective function, is more suitable for minimizing a function with multiple stationary and saddle points. Stochastic methods, discussed in the next chapter, are employed to address the problem.

CHAPTER 6 STOCHASTIC METHODS FOR EDDY CURRENT NDE SIGNAL INVERSION

6.1 Introduction

In the last chapter, a defect characterization method based on a gradient search

minimization algorithm is discussed. The method utilizes the local property (gradient) of the

objective function to speed the search process. Such methods tend to converge to a local

minimum. Compared with the gradient search method, stochastic methods do not rely on the

local properties of the function being minimized. They work well even for nondifferentiable

or discontinuous functions. Since they are based on stochastic assumptions, there is a

nonzero probability that a global minimum will be reached.

Genetic algorithms and simulated annealing methods are two of the common

stochastic optimization methods. Although these methods are relatively new, they have been

used successfully for addressing many optimization applications. The fact that these

methods are capable of finding a global or quasi-global minimum among multiple local

minima is particularly attractive. These methods can be viewed as an analogy to natural

processes that occur in nature. A genetic algorithm mimics Darwin's natural selection

process. A simulated annealing algorithm models the annealing process of a thermodynamic

system consisting of multiple particles. The principles of the two methods and their

performance as a global minimization technique in eddy current NDE signal inversion are

discussed in the following sections.

6.2 Concepts and Terminology of Genetic Algorithms

A genetic algorithm (GA) mimics the process of natural selection. It begins with a group of potential solutions. Each of the individual solutions is evaluated and assigned a fitness figure. Through the process of selection and reproduction, highly fitting characteristics are passed on to the next group of trial solutions while poorly fitting individuals are discarded. The selection and reproduction criterion is based on the fitness figure of each individual. The key terminology and concepts of GAs are borrowed from the theory of Darwin's natural selection. A brief introduction follows.

Genes and Chromosomes. Genes in a GA represent the coding of optimization parameters. A string of genes forms a chromosome. A specific chromosome pattern is simply the coded representation of a trial solution.

Populations and Generations. Individual chromosomes are gathered to form a group of trial solutions, which is termed a population. A GA is an iterative algorithm. Each iteration is termed a generation. During the selection and reproduction process, a new generation is created and used to replace the previous generation. Highly fit characteristics are inherited by the new generation with high probability. The process continues after one generation by one generation causing a drift of the population toward a global optimum.

Fitness. The fitness is a merit of figure to evaluate each individual chromosome. Usually, the objective function defining the optimization goal acts as the fitness figure. The effect of fitness is exerted on each generation through the selection and reproduction process.

Parents and Children. During the selection and reproduction process, a pair or pairs of individual chromosomes are chosen to produce offspring, i.e. more copies of the selected chromosomes. The selected pair or pairs are termed parents. Their offspring are termed

children. In a generation, each chromosome has a fitness associated with it. The selection is performed such that individual chromosomes with better fitness have higher probability of being chosen as parents. Children are reproduced by applying genetic operators to the selected parents. They are placed back in the original population to replace selected individuals with poorer fitness. The modified population replaces the original one as the new generation. In this way, highly fit characteristics of individual chromosomes are passed on to next generations and the poorly fit chromosomes are discarded.

Genetic Operators. The genetic operators are stochastic operators applied on selected parents to produce offspring. Common operators are crossover and mutation. A crossover operation involves the random selection of a crossover point. The gene strings of a selected pair break at the crossover point and the pair exchanges the gene substring following the crossover point to produce two children. Obviously, the children produced contain a recombined set of genes from their parents and thus share the characteristics of their parents. Crossover is the most important genetic operator and occurs with high probability, typically in the range of 0.6-0.8. A mutation introduces new genetic material into chromosomes. In a mutation, genes of selected individuals are randomly picked and replaced with randomly generated genes. So, a mutation serves as a mechanism to introduce underrepresented chromosome patterns to a population. Mutation occurs with a much lower probability, typically in the range of 0.01 to 0.1.

In summary, a GA involves the following processes:

1. Coded representation of optimization parameters and trial solutions. Design parameters are coded as genes to form chromosomes.

2. Creation of an initial population. A group of chromosomes, representing potential solutions are generated, usually in a randomized manner.

3. Evaluation of the individual fitness. The objective function is evaluated and assigned to each individual as its fitness.

4. Evolution. Probabilistic selection is performed to choose parents and poorly fitted individuals. Reproduction operations, are performed on parents to produce children, which replace the poorly fitted individuals.

The details on implementing a GA are introduced in the next section.

6.3 A Genetic Algorithm For Defect Characterization

To minimize an objective function using a GA, the optimization parameters must be first encoded as genes. In a defect characterization problem, these parameters describe the defect profiles. Fig 6.1 shows a defect profile representation expressed in terms of 8 depths: d_1, d_2, d_3, d_4, d_5, d_6, d_7, and d_8. A simple way to encode the parameters is to quantize the depth as the product of an integer and a quantization unit, i.e.

$$d_i = c_i \cdot \Delta d , \quad i = 1, 2, \cdots 8$$

The c_i's are the coded form of d_i's, i.e. genes. Then a specific defect profile is encoded as a string of integers, i.e. chromosomes.

A population consists of individual chromosomes. An initial population could be formed by a pseudo-random number generator, which generates the required c_i's for each chromosome. A chromosome can be decoded into a defect profile. The forward model introduced in chapter 4 is employed to evaluate its associated fitness, which is defined to be
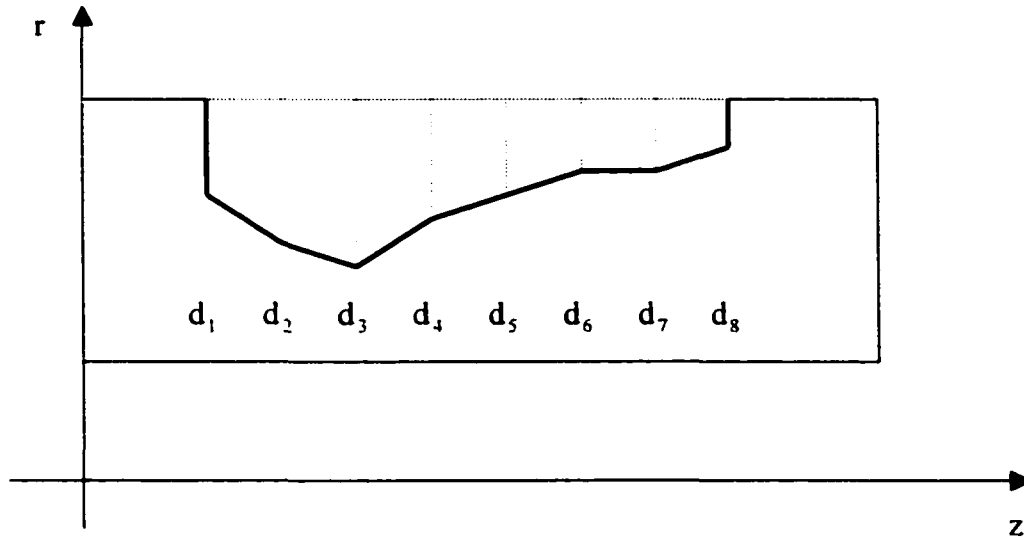
Fig 6.1 A 8 depth defect profile representation

the value of the objective function.

The evolution process consists of selection and reproduction. A selection mechanism must ensure that the relatively more fit individuals have a higher probability to be chosen as parents and the poorly fit individuals have a higher probability to be replaced by new children. The following selection mechanism is employed. Let N be the dimension of the initial population and assume it's a constant throughout the entire evolution. Let f_i be the fitness associated with each chromosome. Perform the following operations on f_i,

$$f_{max} = \max_i\{f_i\} \qquad i = 1, 2, \cdots N.$$

$$r_i = f_{max} - f_i$$

$$q_i = \frac{r_i}{\sum_{k=1}^{N} r_k}$$

$$p_i = \sum_{k=1}^{i} q_k, \qquad p_0 = 0.$$

Obviously, the following relation between q_i and p_i exists.

$$q_i = p_i - p_{i-1}, \quad i = 1, 2, \cdots N.$$

A relatively fit individual has a lower value of fitness f_i and thus a higher value of r_i. q_i is

the normalized value of r_i, scaled to be within 0 and 1. To see the sense of p_i 's, arrange

them in a one-dimensional coordinate system, as shown in Fig 6.2. Generate a random

number p, uniformly distributed in the interval $(0,1)$. Then the probability that p is

between p_{i-1} and p_i is q_i, i.e.

$$\text{Prob}(p_{i-1} \le p \le p_i) = q_i$$

This relation suggests a selection mechanism:

Generate a random number p, uniformly distributed in the unit interval $(0,1)$, then

Chromosome i with fitness f_i is selected, if p satisfies $p_{i-1} \le p \le p_i$.

The probability that Chromosome i is selected is q_i. The above mechanism ensures that the

less an individual's fitness f_i, the more probable it is selected.

Define the following series,

$$f_{min} = \min_i \{f_i\}$$

$$r_i = f_i - f_{min}$$

$$q_i = \frac{r_i}{\sum_{k=1}^{N} r_k}$$

$$p_i = \sum_{k=1}^{i} q_k, \quad p_0 = 0$$

A similar mechanism is established to select poorly fit individuals with the property that if

the fitness of an individual is high, it is selected with a higher probability.

Once a pair of parents is selected, crossover or mutation may be performed to

produce a pair of children. Fig 6.3 illustrates a single-point crossover operation on a pair of

1 2 3 - - - N-1 N

$p_0 = 0$ p_1 p_2 p_3 - - - p_{N-1} $p_N = 1$
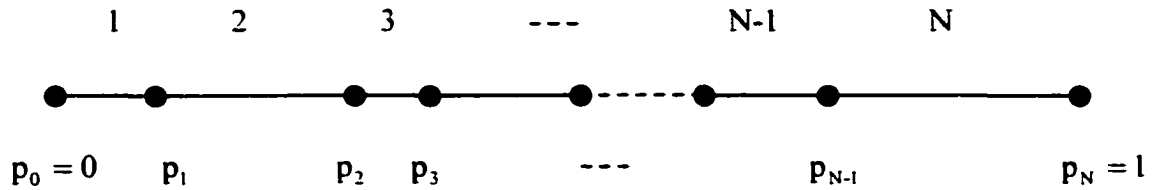
Fig 6.2 Geometrical representation of a GA selection mechanism
Individual i is selected if a randomly generated number p, uniformly distributed in
(0, 1), falls in the interval (p_{i-1}, p_i). The probability of its selection is q_i .

chromosomes. Its actual effect on the defect profiles is shown in Fig 6.4. The crossover

operation is actually a recombination of the genes of the selected chromosomes. In Fig 6.3

and Fig 6.4, only one crossover point is randomly picked. This kind of crossover is termed

single-point crossover. A child cannot possess both the first several and the last several

genes of its parents simultaneously in a single-point crossover, which may cause important

characteristics to be lost. To overcome this deficiency, two-point crossover is introduced to

replace the simple single-point crossover. In a two-point crossover, two locations are

randomly picked and the genes between the two locations are exchanged to produce two

children. Fig 6.5 and Fig 6.6 illustrates the two-point crossover operation and its effect on

defect profiles. Since highly fit individuals have a higher probability of being selected as

parents, their characteristics are passed on to their children through crossover.

A mutation operation on a chromosome is illustrated in Fig 6.7. A location in a

selected chromosome is randomly picked and the corresponding gene is replaced with a

randomly generated gene. Its effect on a defect profile is shown in Fig 6.8. Such an

operation is capable of creating a new chromosome pattern and thus introduces

underrepresented characteristics into a generation. Both crossover and mutation are
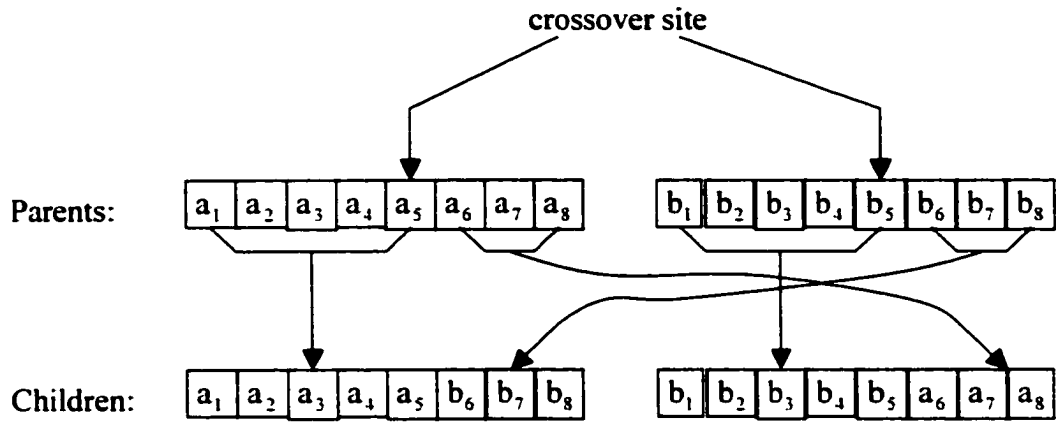
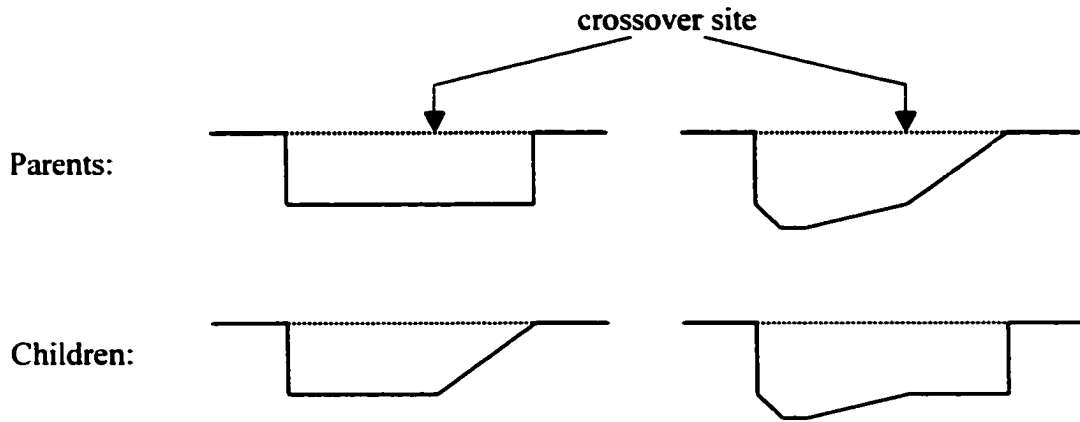Fig 6.3 A single-point crossover operation

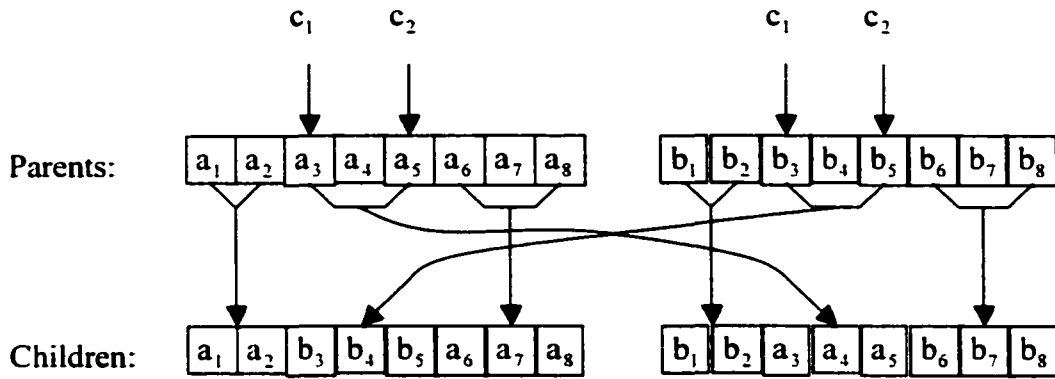Fig 6.4 The effect of single-point crossover on defect profiles

Fig 6.5 A two-point crossover operation
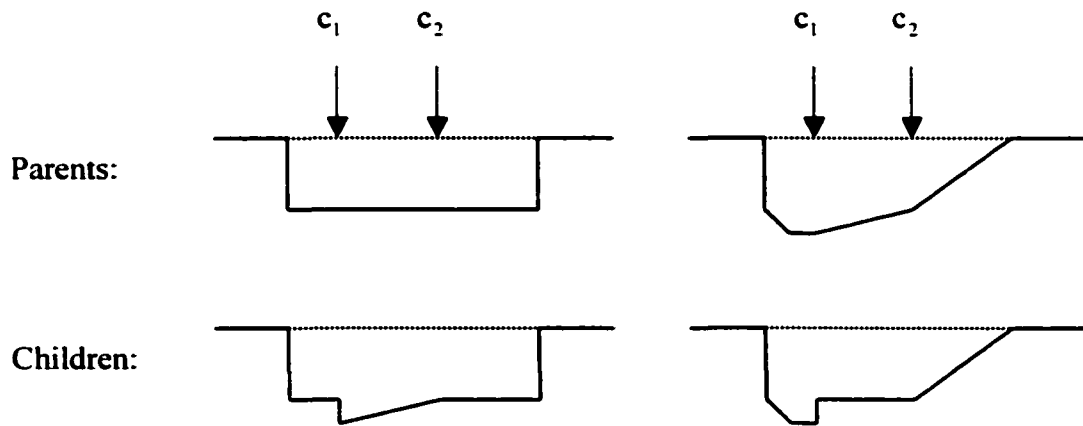

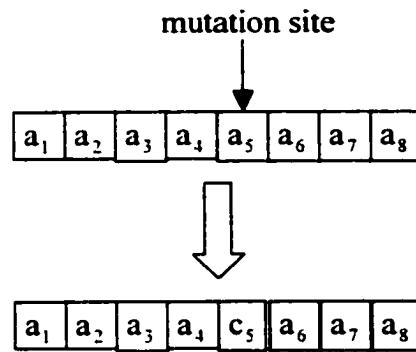Fig 6.6 The effect of two-point crossover on defect profiles

mutation site

a₁ | a₂ | a₃ | a₄ | a₅ | a₆ | a₇ | a₈

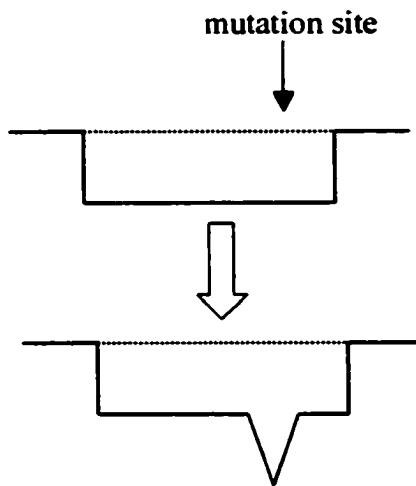a₁ | a₂ | a₃ | a₄ | c₅ | a₆ | a₇ | a₈

Fig 6.7 A mutation operation

mutation site

Fig 6.8 The effect of a mutation operation on defect profile

probabilistic operations. The probabilities, p_{cross} and p_{mute}, are assigned before the evolution

process. A random number generator, which generates random numbers, uniformly

distributed between 0 and 1, is employed to choose which operation needs to be performed.

If the random number p is less than p_{mute}, mutation is performed. If p is greater than p_{mute}

but less than $(p_{mute} + p_{cross})$, crossover is performed. If p is larger than $(p_{mute} + p_{cross})$, the

chromosome patterns of the selected parents are passed on to the children without any

changes. The generated children are used to replace two poorly fit individuals of the original

generation. A new generation is then created.

A genetic algorithm is illustrated by the flow chart shown in Fig 6.9. It first creates

an initial population by randomly generating a group of chromosome patterns and calls for

the forward model to evaluate the fitness of each chromosome. Then the selection

mechanism described above is employed to select a pair of parents and a pair of poorly fit

individuals. Next, crossover, mutation, or a direct copy is performed in a probabilistic

manner. The newly generated children then replace the two selected poorly fit individuals to

create the next generation. A stopping criterion is invoked to determine when to stop the

evolutionary process. The average fitness of a generation can be one of the possible stopping

criteria. Whenever the average fitness is sufficiently small, the evolution stops. This

algorithm is applied to eddy current NDE signal inversion. Results obtained using this

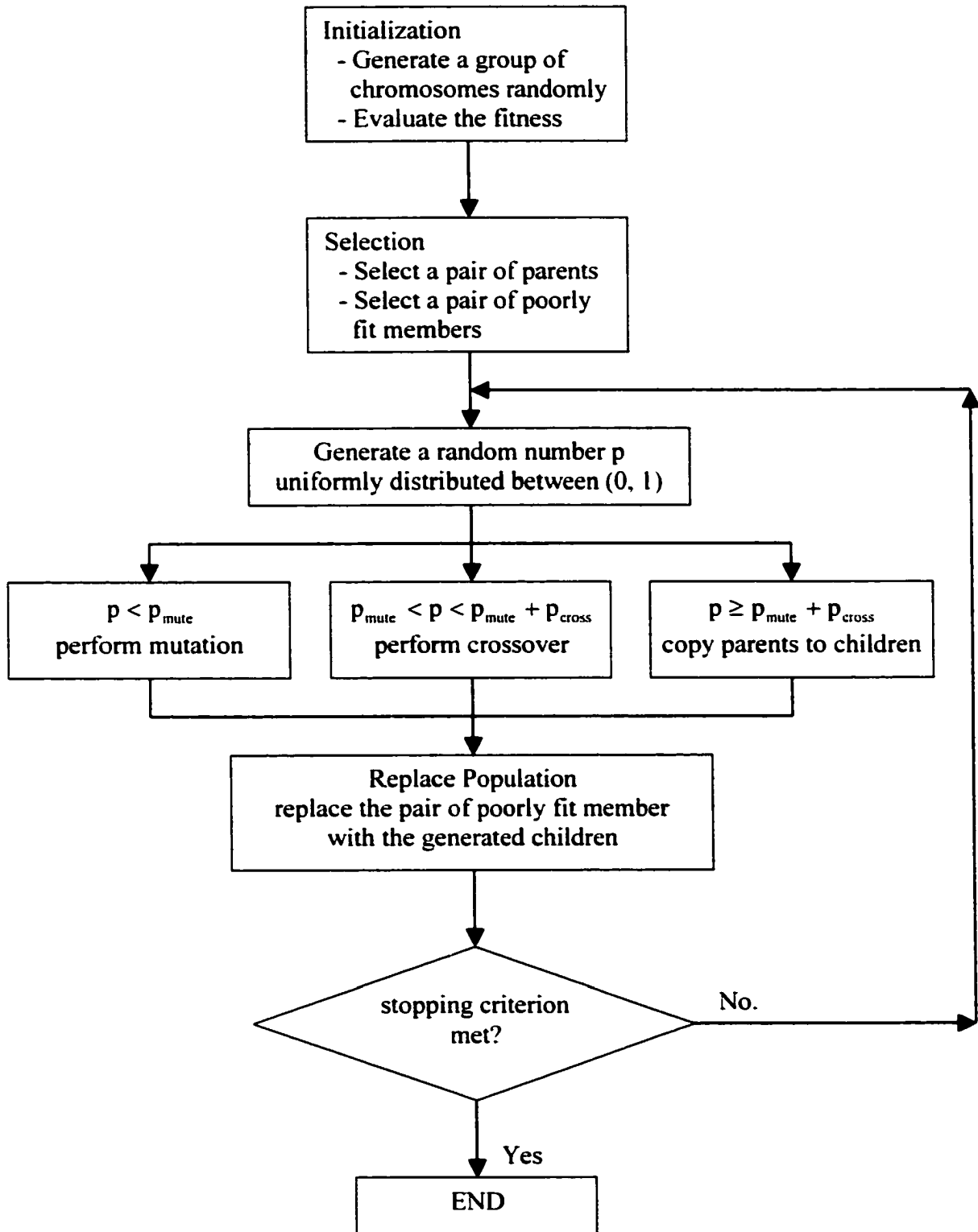approach are presented in the following section.

```
┌─────────────────────────────────┐
│ Initialization                  │
│ - Generate a group of           │
│   chromosomes randomly          │
│ - Evaluate the fitness          │
└─────────────────────────────────┘
                │
                ▼
┌─────────────────────────────────┐
│ Selection                       │
│ - Select a pair of parents      │
│ - Select a pair of poorly       │
│   fit members                   │
└─────────────────────────────────┘
                │
                ▼
┌─────────────────────────────────┐
│ Generate a random number p      │
│ uniformly distributed between (0, 1 ) │
└─────────────────────────────────┘
```

$p < P_{mute}$
perform mutation

$P_{mute} < p < P_{mute} + P_{cross}$
perform crossover

$p \geq P_{mute} + P_{cross}$
copy parents to children

Replace Population
replace the pair of poorly fit member
with the generated children

stopping criterion met?

No.

Yes

END

Fig 6.9 The flow chart of a genetic algorithm

6.4 Defect Characterization In Heat Exchanger Tubes

Section 5.4 presents an eddy current NDE system that employs a differential pair of probes to scan a heat exchanger tube. The probe response is calculated using the edge element forward model introduced in Chapter 4. A gradient-based minimization algorithm is employed to minimize the objective function. As discussed in section 5.5, the gradient search scheme tends to converge to a poorer local minimum and suffers from bad convergence. In this section, the genetic algorithm introduced in the last section is employed to minimize the objective function. The eddy current NDE problem described in the proceeding chapter is used for evaluating the approach. The defect profile is described using 8 depths, as shown in Fig 6.1. Fig 6.9 shows the flow chart of the algorithm. The dimension of the population is fixed during evolution. Each generation, up to 10% of the chromosomes are selected to produce next generation. So, the entire population does not need to be reevaluated for the fitness. Only the new members (up to 10%) need to be evaluated. Since evaluating each chromosome calls for the forward model once, this could partially reduce the computation burden.

Fig 6.10 shows a GA reconstructed defect profile. The desired profile has a rectangular shape. In Fig 6.10, (a), (b), and (c), the desired profiles are represented with solid lines. The cross signs represent the reconstructed optimization parameters (i.e. genes). The horizontal axis represents the axial direction in inch and the vertical axis represents the radial direction in inch. The result shown in (a) is obtained with the dimension of the GA population $N = 20$. The results shown in (b) and (c) correspond to $N = 50$ and $N = 100$ respectively. The effect of the dimension of the population is illustrated in Fig 6.10 (d), which shows the average fitness of the population vs. the iteration number. The value of the

(a)

(b)

(c)

(d)
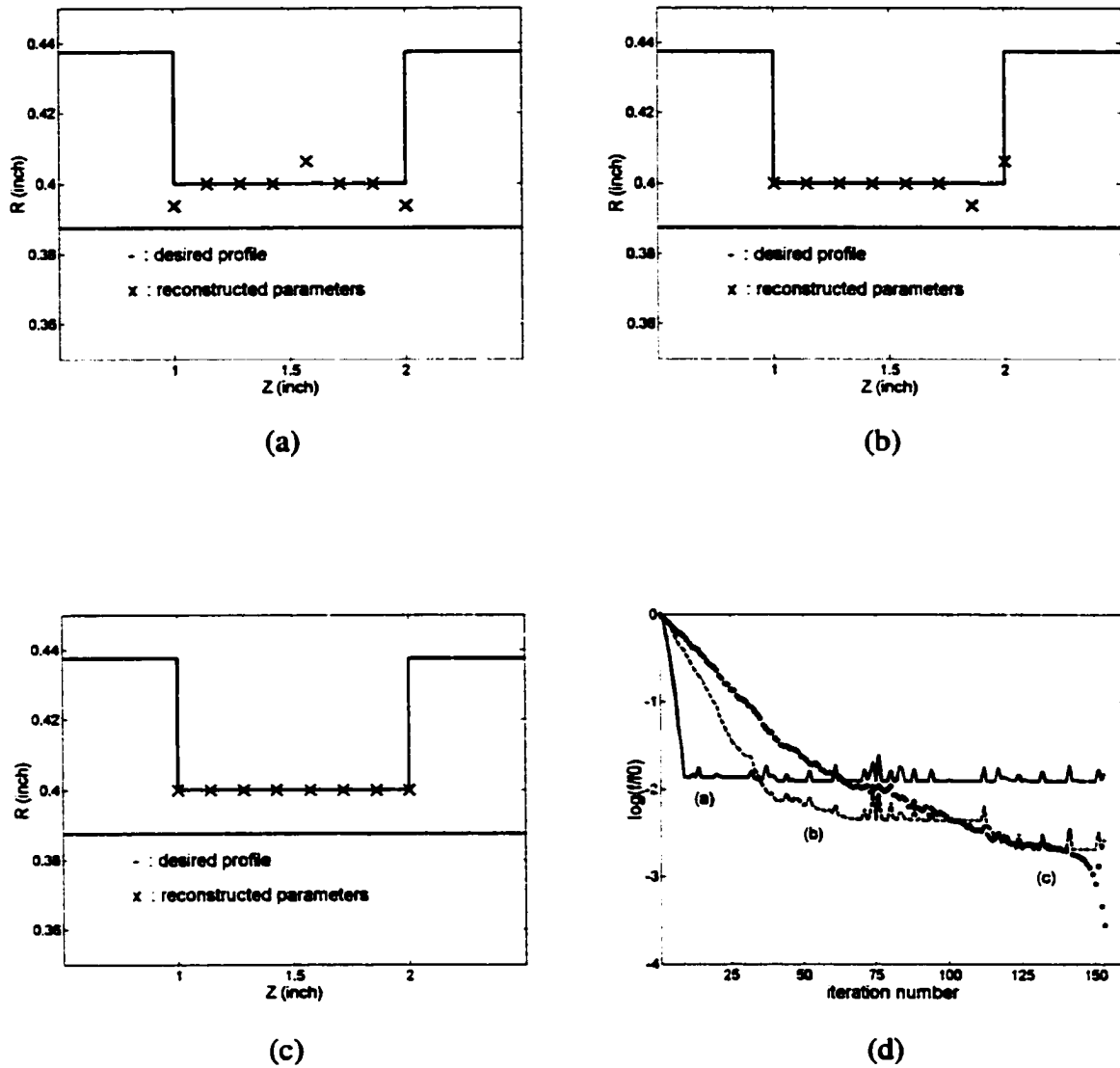
Fig 6.10 GA defect characterization Case 1

(a), (b), and (c) show the desired defect profiles (solid line) and the reconstructed parameters (cross sign) with the dimension of the population being N=20, N=50 and N=100 respectively. The horizontal axis represents the axial direction in inch and the vertical axis represents the radial direction in inch. (d) shows the normalized average fitness vs. iteration number.

average fitness, f, is normalized with respect to the average fitness of the initial population, f0, and expressed in logarithm scale. When $N = 20$, the average fitness is reduced 90 times after approximately 10 iterations and stabilizes at that level. When $N = 50$, the average fitness is reduced 120 times after approximately 120 iterations. When $N = 100$, the average fitness is reduced nearly 10,000 times after 150 iterations. As the dimension sizes increases, the GA converges to a better minimum at the expense of increased computation time.

One common problem with genetic algorithms is the so called "premature convergence", which means the population matures at an early stage of the evolution resulting in the average fitness stabilizing at a poorer value. Mutation operations may be able to make the GA "jump" out of the local minimum. However, the probability of mutation is usually so low that increasing the number of iterations does not help too much. This phenomenon is observed in the case $N = 20$ and $N = 50$ as shown in Fig 6.10 (a) and (b). When a GA matures, all chromosomes in the population often contain the similar patterns. Consequently, it is very difficult for the population to drift to a better minimum. This phenomenon is caused by the fact that the dimension of the population is usually much smaller compared to the dimension of the search space. Therefore, it is impossible for the initial population to represent all the possible chromosome patterns. The "premature convergence" problem can be improved by increasing the dimension size so that the population represents more chromosome patterns, as shown in Fig 6.10 (c).

More test results on defect characterization are shown in Fig 6.11 – Fig 6.17. These results are obtained with the dimension of the population being 100. In most cases, the GA reduces the value of the objective function approximately 100 times after 150 iterations. The GA works well for a large number of defect profiles. Although we see evidence of

"premature convergence" in some cases, the reconstructed profiles are already very close to

the desired ones. These examples indicate the effectiveness of genetic algorithms and show

that it can be viewed as a powerful tool for NDE signal inversion.

6.5 Noise Effect on Defect Characterization

The defect characterization results presented in the last section is obtained with the

input signal generated by the finite element forward model. In an actual defect

characterization application, the input signal is the measured output of the probes. Various

kinds of noise are inevitable in such signals. This section discusses the effect of signal noise

on the genetic algorithm in defect characterization. Fig 6.18 shows a typical output signal

from a differential probe and the signal added with noise. The signal (solid line) is generated

using the edge element forward model. White noise is added to the signal to illustrate the

effect of noise. The noise level is 20% with respect to the magnitude of the generated signal.

To see the effect of noise on GA defect characterization algorithm, the input signals

to the GA, generated by the forward model, are added with random noise. Two noise levels,

10% and 20%, are tested. The defect reconstruction results on case 1, case 2, case 7 and case

8 are shown in Fig 6.19 – 6.22 for comparison. The results indicate that the GA is very

sensitive to noise. Even 10% can disturb the reconstructed defect profile significantly.

Recall that the defect profile is represented by 8 depths and each depth is quantized to one of

8 levels, which may be too coarse for a real application. More quantization level is needed to

improve the space resolution. However, that usually requires much more computation
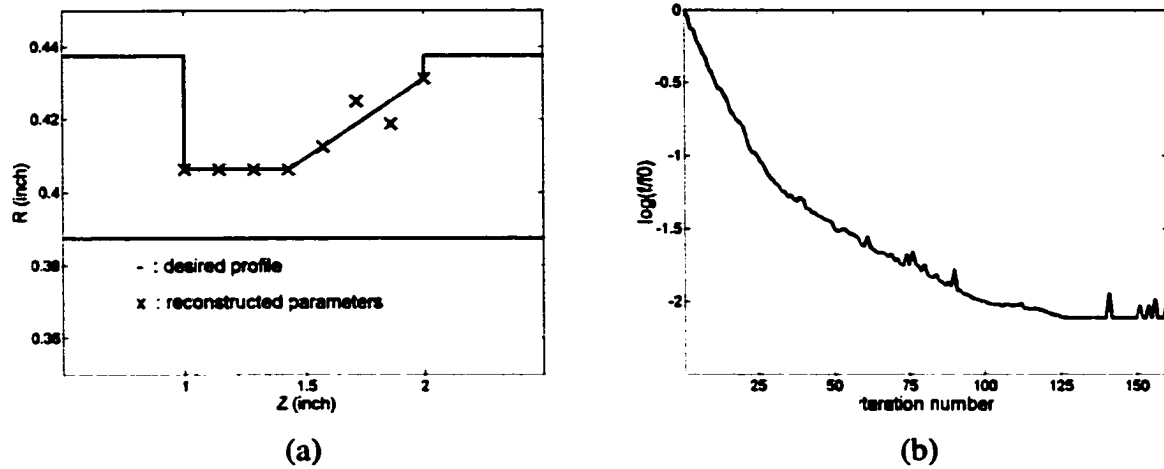
resources.

Fig 6.11 GA defect characterization Case 2

(a) shows the desired defect profile (solid line) and the reconstructed parameters (cross sign) with the dimension of the population being N=100. (b) shows the normalized average fitness vs. iteration number.
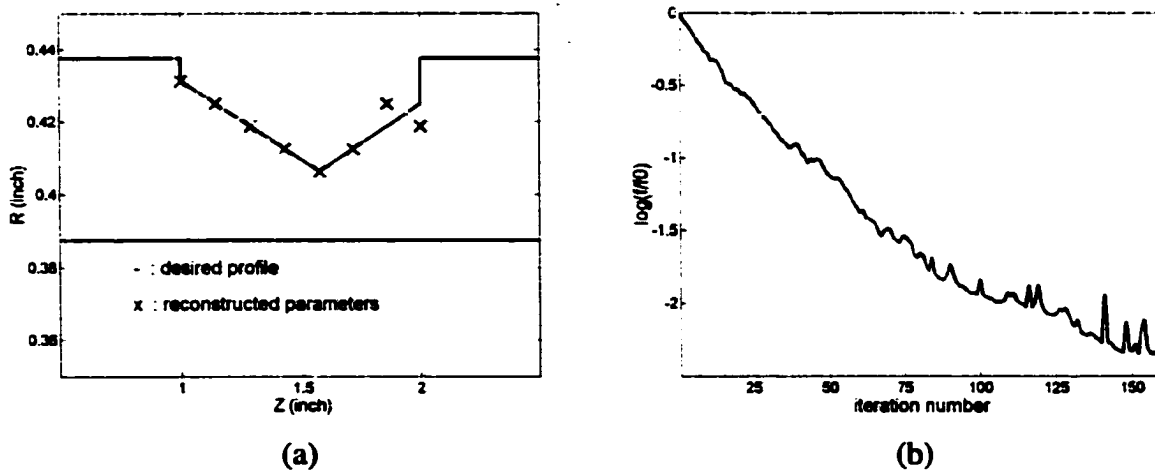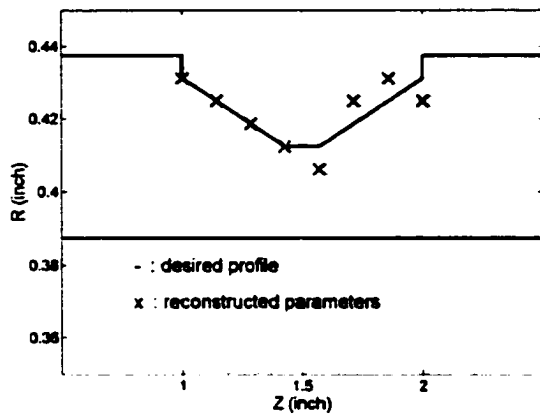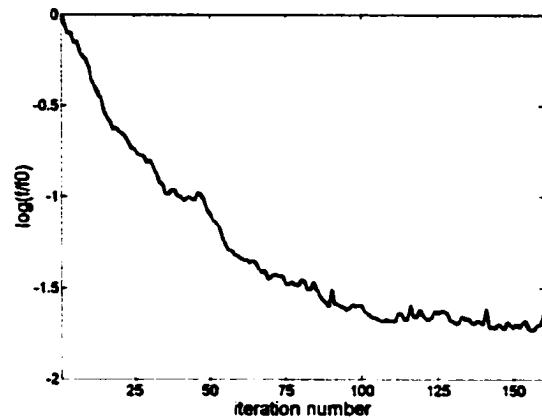

Fig 6.12 GA defect characterization Case 3

(a) shows the desired defect profile (solid line) and the reconstructed parameters (cross sign) with the dimension of the population being N=100. (b) shows the normalized average fitness vs. iteration number.
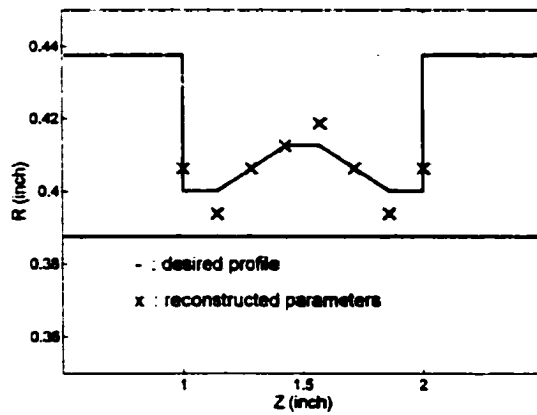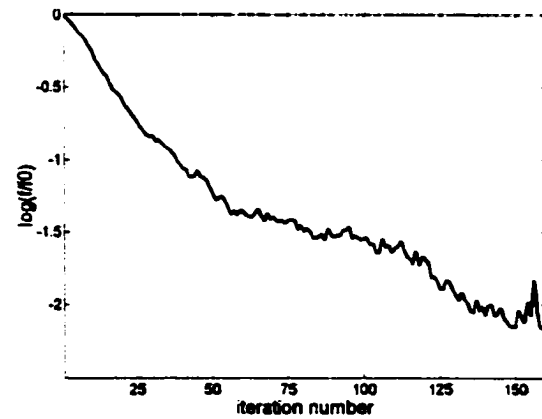
(a)

(b)

Fig 6.13 GA defect characterization Case 4
(a) shows the desired defect profile (solid line) and the reconstructed parameters (cross sign) with the dimension of the population being N=100. (b) shows the normalized average fitness vs. iteration number.

(a)

(b)

Fig 6.14 GA defect characterization Case 5
(a) shows the desired defect profile (solid line) and the reconstructed parameters (cross sign) with the dimension of the population being N=100. (b) shows the normalized average fitness vs. iteration number.
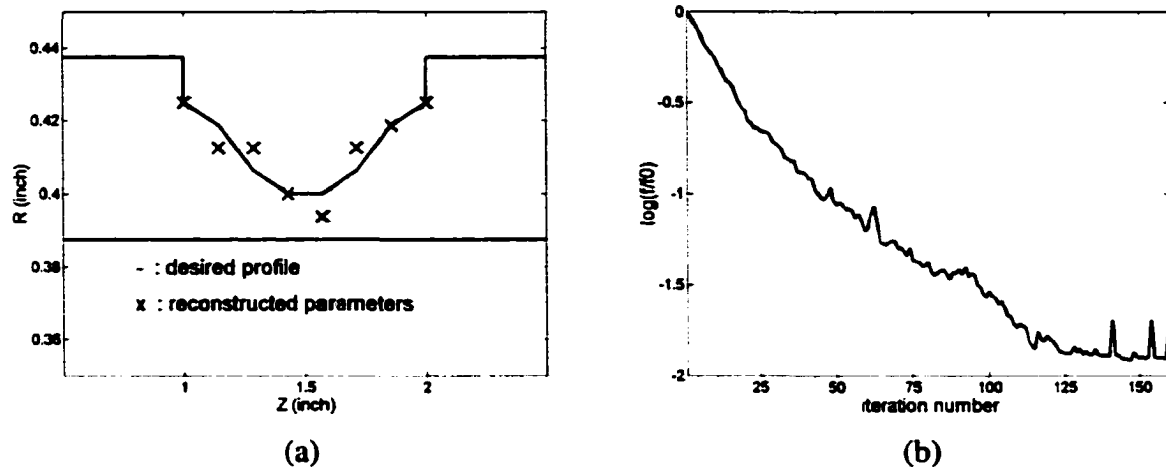
(a)

(b)

Fig 6.15 GA defect characterization Case 6
(a) shows the desired defect profile (solid line) and the reconstructed parameters (cross sign) with the dimension of the population being N=100. (b) shows the normalized average fitness vs. iteration number.
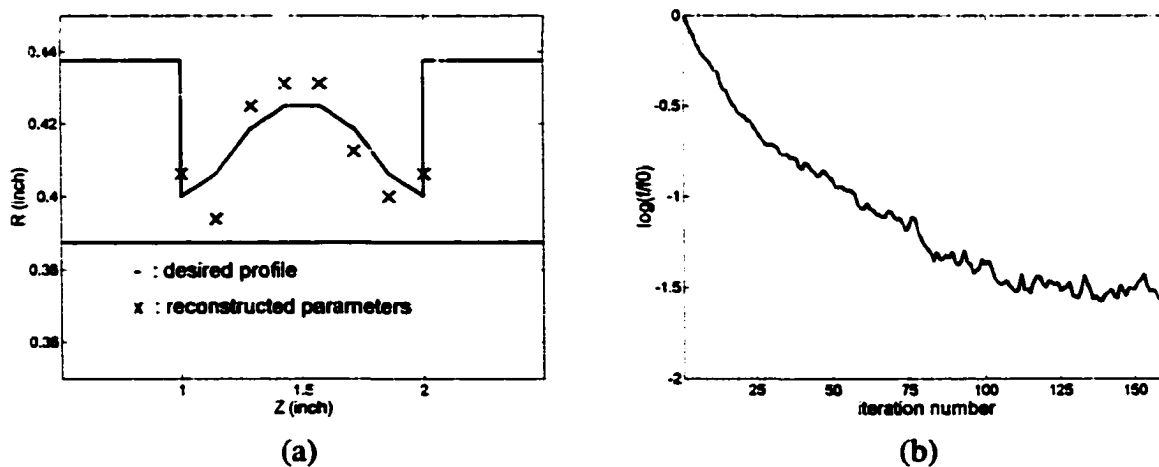

(a)

(b)

Fig 6.16 GA defect characterization Case 7
(a) shows the desired defect profile (solid line) and the reconstructed parameters (cross sign) with the dimension of the population being N=100. (b) shows the normalized average fitness vs. iteration number.

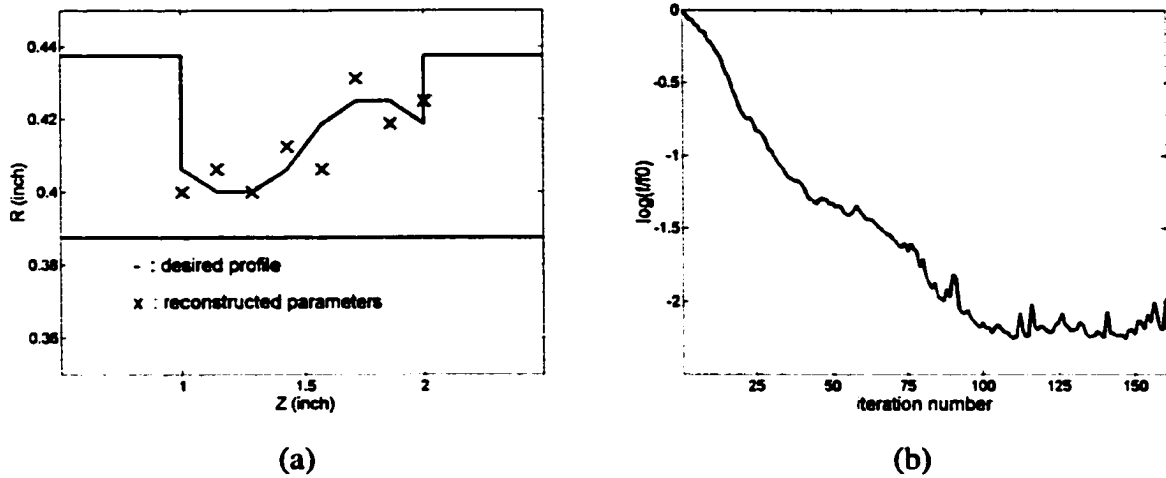(a) (b)

Fig 6.17 GA defect characterization Case 8
(a) shows the desired defect profile (solid line) and the reconstructed parameters (cross sign) with the dimension of the population being N=100. (b) shows the normalized average fitness vs. iteration number.
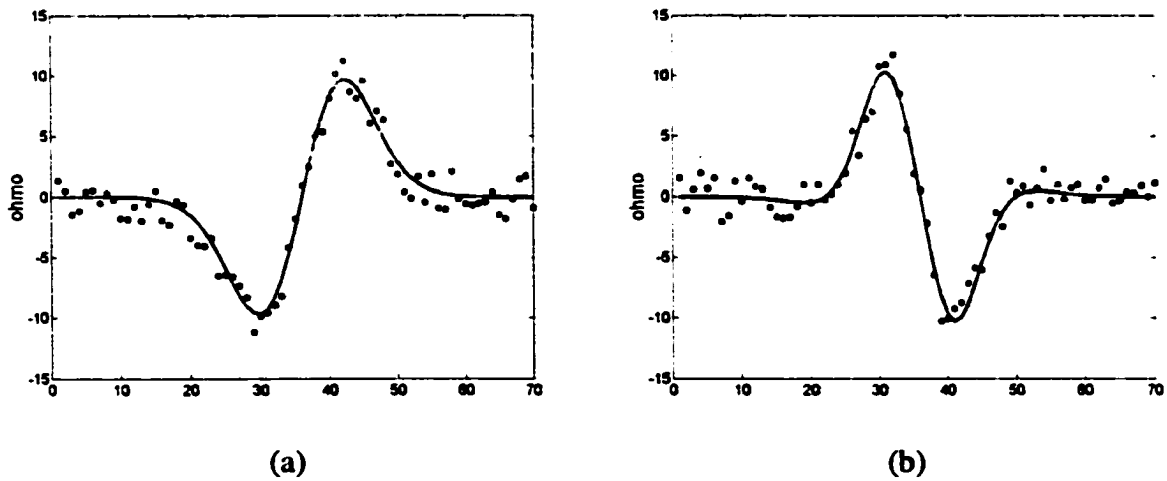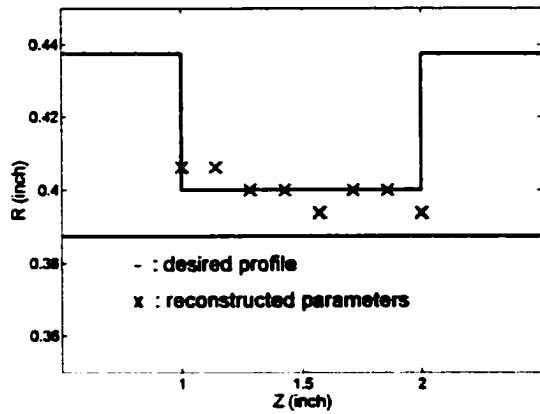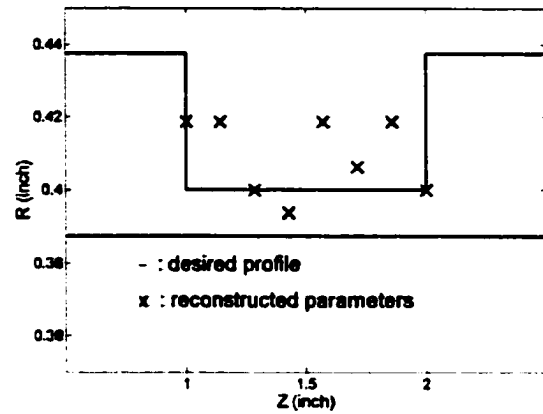

(a) (b)

Fig 6.18 A typical probe signal added with white noise
(a) shows real part of a differential probe signal (solid line) and the signal added with 20% white noise (dot sign). (b) shows the imaginary part of the signal (solid line) and the signal with 20% white noise (dot sign).

(a)

(b)

Fig 6.19 Noise effect on GA defect characterization Case 1
(a) shows the reconstructed parameters obtained with noised signal (noise level 10%)
(b) shows the reconstructed parameters obtained with noised signal (noise level 20%)

(a)

(b)

Fig 6.20 Noise effect on GA defect characterization Case 2
(a) shows the reconstructed parameters obtained with noised signal (noise level 10%)
(b) shows the reconstructed parameters obtained with noised signal (noise level 20%)

(a)   (b)

Fig 6.21 Noise effect on GA defect characterization Case 7
(a) shows the reconstructed parameters obtained with noised signal (noise level 10%)
(b) shows the reconstructed parameters obtained with noised signal (noise level 20%)
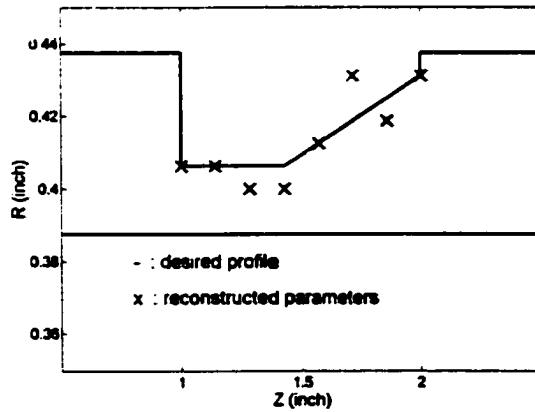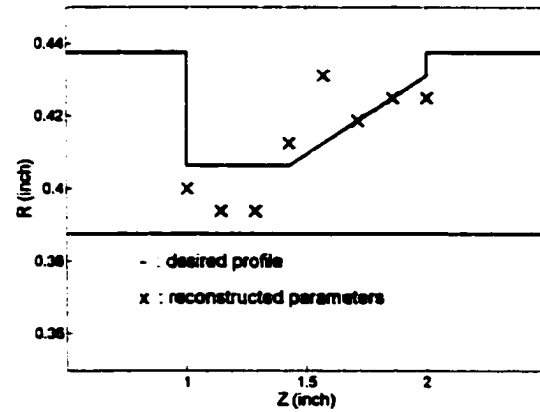

(a)   (b)

Fig 6.22 Noise effect on GA defect characterization Case 8
(a) shows the reconstructed parameters obtained with noised signal (noise level 10%)
(b) shows the reconstructed parameters obtained with noised signal (noise level 20%)
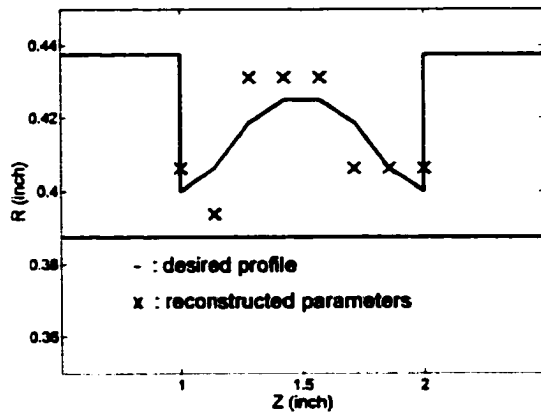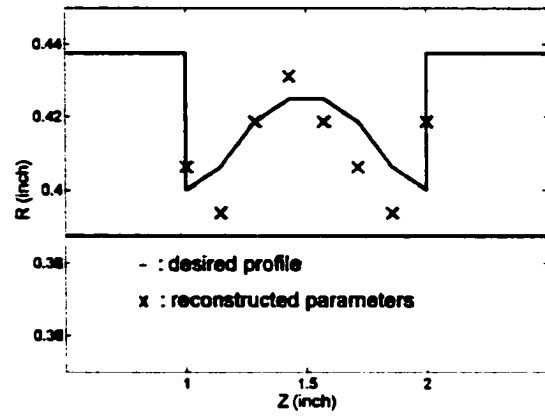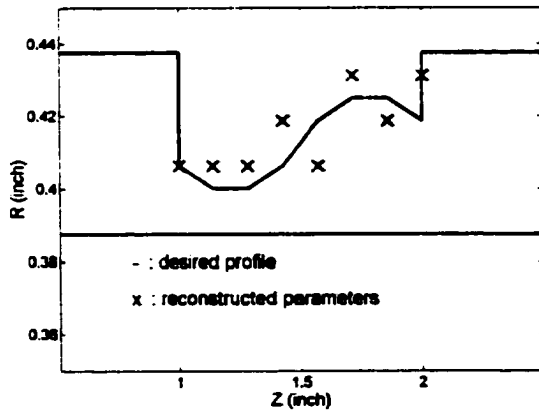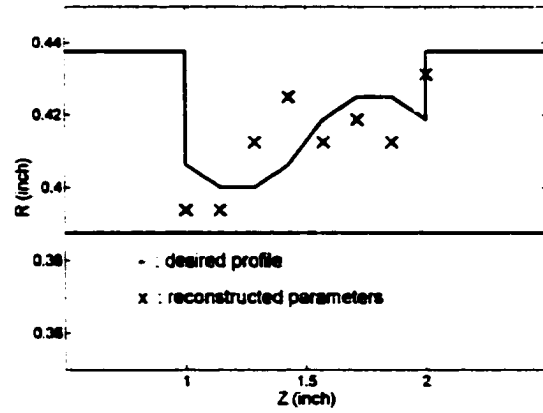
6.6 The Simulated Annealing Method

Like genetic algorithms, the simulated annealing method has attracted a significant

degree of attention as a global optimization technique. The basic principle underlying the

simulated annealing algorithm is related to the cooling process of a thermodynamic system.

Consider a thermodynamic system consisting of multiple particles. At high temperature,

these particles move freely. As the system cools slowly, the particles tend to line themselves

up to reach a state of minimum energy for the system. The amazing fact is that this

minimum energy state is reached automatically for a slowly cooling system.

We draw an analogy between a minimization problem and the thermodynamic

multiple particle system to gain an understanding of the optimization procedure. The

parameters being estimated correspond to the configuration of the thermodynamic system

(the relative positions of the particles). The objective function, the minimization goal,

corresponds to the energy of the system. To mimic the cooling process of the

thermodynamic system, a control variable is introduced, which corresponds to the

temperature. The movement of the particles is modeled as the random change of the

minimization parameters. Suppose a random movement changes the configuration from a

state with energy E_1 to a state with energy E_2. The transition from E_1 to E_2 is accepted

with the probability

$$p = e^{-\frac{E_2 - E_1}{kT}}$$

where k is the Boltzmann's constant and T is the control variable (temperature). If E_2 is less

than E_1, then p is greater than 1. In this case, p is assigned the value 1 and state E_2 is

always accepted as the next configuration. If E_2 is greater than E_1, state E_2 is accepted in a

probabilistic manner. Obviously, both the downhill and the uphill movement are allowed for

a system. But as the control variable decreases, the probability for uphill movement

decreases too. Therefore, a control variable reduction mechanism must be included in a

simulated annealing algorithm to reduce the value of the control variable after certain

changes of the system configuration. This mechanism is termed cooling schedule.

In summary, a simulated annealing algorithm proceeds as follows:

1. Begins with an initial system configuration and calculates its energy; Assigns an

   initial value to the control variable T.

2. Makes a random perturbation of the system configuration and calculates its

   energy.

3. Decides whether to accept or reject the new configuration according to the

   Boltzmann's probability distribution equation.

4. If the system configuration changes significantly, reduce the value of the control

   variable according to the cooling schedule. Or, return to step 2.

5. If the system energy is sufficiently small, then stop. Or, return to step 2.

The initial value of the control variable and the cooling schedule are very critical for a

successful implementation of the above algorithm. For a specific problem, they must be

empirically tuned. The initial value of the control variable usually ensures that all possible

transitions are accepted, i.e.

$$p = e^{-\frac{\Delta E}{kT_0}} \approx 1$$

This corresponds to a thermodynamic system at high temperature. All particles move freely.

A cooling schedule models a physical annealing process, the essence of which is infinitely

slow. So, the control variable is reduced gradually, the following cooling schedule is often

employed,

$$T_{k+1} = \alpha \cdot T_k$$

where α is an empirically tuned constant, generally in the range 0.8-0.99.

Unlike genetic algorithms, a simulated annealing algorithm does not rely on a

selection mechanism. Instead it rather relies on a rejection mechanism. Therefore, a huge

number of random perturbations are necessary. The computation burden for evaluating the

energy associated with each possible configuration is much heavier than that for a genetic

algorithm.

Fig 6.23 shows four defect reconstruction examples obtained using the simulated

annealing method. For comparison, case 1, case 2, case 6 and case 8, used in testing the

genetic algorithm, are addressed again using the simulated annealing method. Acceptable

solutions are reached after evaluating the objective function approximately 5000 times.

While for the genetic algorithm discussed in the last two sections, each generation produces

up to 10 new chromosomes. An 150 iteration evolution process requires evaluating the

objective function 1500 times.

6.7 Conclusions and Discussions

The effectiveness of the genetic algorithm and the simulated annealing method has

been demonstrated. These methods do not rely on any local properties of the function being

minimized. Unlike gradient based minimization algorithms, they work well even in the case

of nondifferentiable or discontinuous functions. It has been shown that these stochastic

methods reach a global minimum with a nonzero probability.
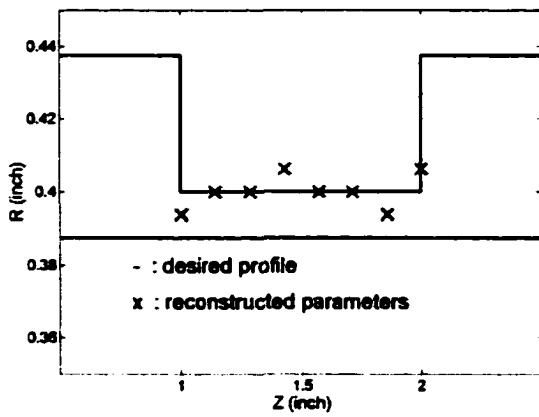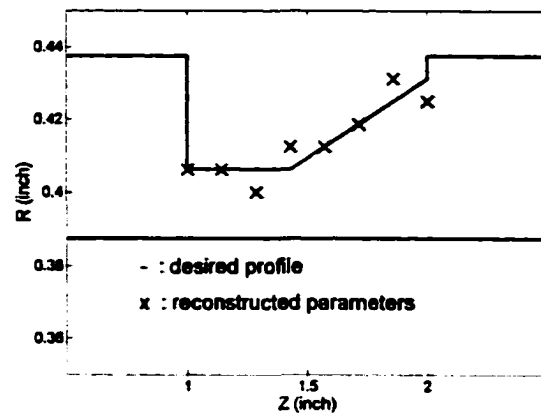
Fig 6.23 Simulated annealing defect characterization examples
(a) shows the reconstructed parameters (cross sign) obtained from the simulated
annealing method for Case 1, used in section 6.4. (b), (c) and (d) show the results for
Case 2, Case 6, and Case 8 respectively.

The mechanism for the genetic algorithm and the simulated annealing algorithm is quite different. The genetic algorithm begins with a group of trial solutions. A global or a quasi-global solution is reached through the process of selection and reproduction, in which highly fit 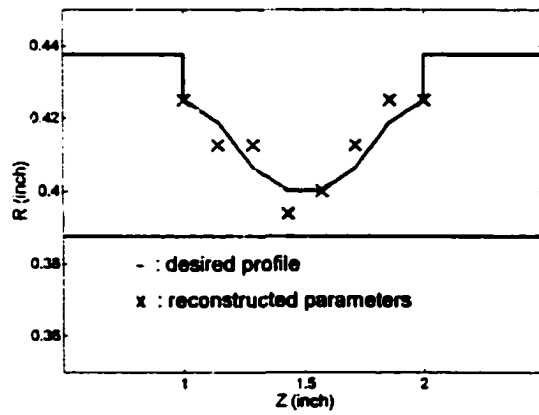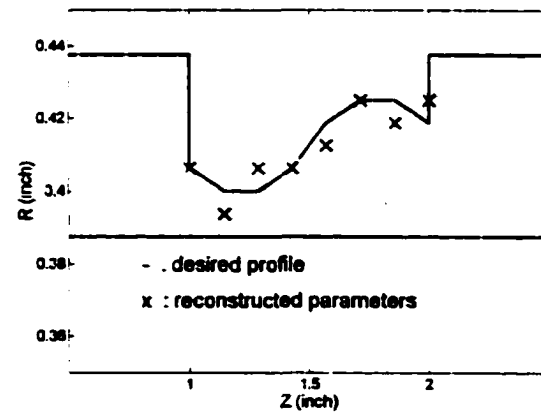characteristics are passed on and poorly fit ones are discarded. It suffers from the problem of "premature convergence". Its performance can be improved by increasing the dimension of the population or employing advanced evolution techniques. The simulated annealing algorithm begins with a single trial solution. A global minimum is reached by randomly perturbing the trial solution and selectively rejecting the unwanted solutions. It does not suffer from problems such as "premature convergence". However, the method requires a large amount of computation effort in evaluating these trial solutions.

The main problem associated with stochastic methods is the heavy computation burden involved in evaluating the objective functions repeatedly. Take the genetic algorithm as an example. In each iteration, usually 10% of the total population is updated. Suppose the dimension of the population is 100. Then the forward model is called ten times to evaluate their fitness. Suppose 150 iterations are needed to reach an acceptable minimum. This requires the governing linear system to be solved 1500 times. The number is even larger for the simulated annealing algorithm. To reduce the computation time to a reasonable level, a special technique based on Woodsbury's technique is employed in this work [89]. Consider the finite element mesh of the geometry shown in Fig 6.24 (a). For different defect profiles, only a small part of the mesh, i.e. the defect region, is different. This suggests a way to reduce the computational effort, which requires numbering the branches such that those branches located outside the defect region are numbered first and those inside the defect region are numbered last. We then partition the stiffness matrix as shown in Fig 6.24 (b).

(a)
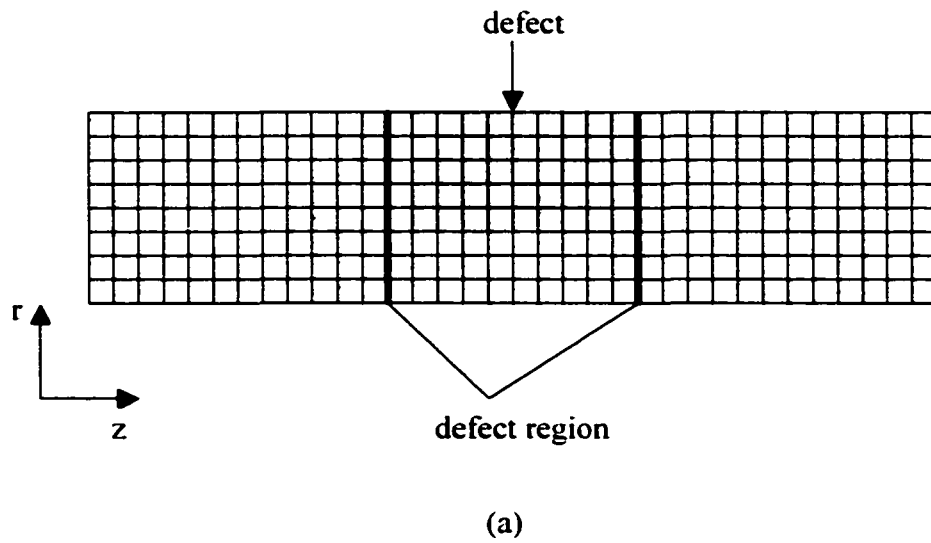
(b)

Fig 6.24 The finite element mesh of a tube with a defect and its partitioned stiffness matrix (a) shows an axisymmetric plane of the finite element mesh of a tube with the defect elements darkend. (b) shows the stiffness matrix partitioned in accordance with the mesh.

Matrix C_{00} corresponds to the unknowns associated with the branches outside the defect

region, and thus remains constant throughout the entire signal inversion process. Matrix C_{11}

corresponds to the unknowns associated with those branches inside the defect region.

Whenever the defect profile is different, it must be updated accordingly. The fact that the

linear system needs to be solved thousands of times suggests the use of a direct linear solver,

such as the LU factorization method. Matrix C_{00} needs to be factorized just once. Each time

the defect profile is changed, matrix C_{11} is updated and factorized. Since the dimension of

C_{11} is much smaller than that of C_{00}, a significant amount of computation is saved. With the

rapid development in computation facilities and techniques, parallel computation becomes

cheaper and open to a lot of research and application areas. The algorithms in this

dissertation are implemented in a SGI origin 2000 super computer, which has 16Gbits

memory and 16 processors. With 4 processors, a speedup of 2.5 is reached.

CHAPTER 7 CONCLUDING REMARKS AND FUTURE WORK

The gradient based minimization method works well for 'well-behaved' functions. It relies on the gradient of the function to find an optimum search direction and usually goes greedily along that direction as far as possible. This makes the gradient based method converge very fast. In many applications, the gradient computation is often costly. NDE signal inversion is one of such case. Since multiple minimization parameters are involved, the forward model usually needs to be solved repeatedly to calculate the required partial derivatives. In this dissertation, an adjoint equation based method is presented to reduce the amount of gradient computation. Using the method of Lagrangian multipliers, the gradient of the objective function is expressed in terms of the Lagrangian multipliers, which can be obtained by solving the forward model only once. This reduces the computation effort significantly. However, the gradient based minimization method suffers from problems of multiple local minima and poor convergence. The greediness of the gradient based method often leads to a local minimum and results in a solution that is dependent on the initial trial solution. This limits the application of the method to simple cases.

Unlike the gradient based method, stochastic methods do not rely on any local properties of the function being minimized. They work well even for nondifferentiable or discontinuous functions. Their stochastic property makes them suitable in many minimization applications, where the gradient based method is problematic. This is especially true in situations where a global minimum is hidden among multiple poorer local minima. This dissertation demonstrates the effectiveness of the genetic algorithm and the simulated annealing method for eddy current NDE signal inversion. The main problem with

stochastic methods is that they require the evaluation of the objective function a large number

of times. A fast forward model is a prerequisite for using such methods for NDE signal

inversion. This dissertation employs a direct linear solver implemented using Woodbury's

algorithm, which significantly saves the amount of computation. Parallel computational

techniques are also utilized to reduce the entire computation effort.

A lot of work has already been done in reconstructing two dimensional defect

profiles. Three dimensional signal inversion will attract more and more attention in the

future. The edge based finite element forward model presented in this dissertation is capable

of simulating a 3D defect. However, the output signal from a differential probe employed in

this work is not very sensitive to the perturbation of defect profiles in the circumferential

direction. The advantage of using a differential probe is that it offers the benefit of low

computational effort since the finite element mesh remains the same as the probe moves

inside the tube. This implies that the stiffness matrix remains constant. To simulate a 3D

defect, the forward model must be modified such that it is capable of simulating other types

of probes, such as pancake probes. Three dimensional defect reconstruction demands

significant computational resources when stochastic minimization algorithms are employed.

Consider the defect profile characterized at 8 different points as shown in Fig 6.1. If the

quantization level of the defect depth is 8, then the search space is very large involving 8^8

candidates. If we consider a 3D defect characterization application, the number of candidates

increases to 8^{64}. In this case, parallel computing is no longer a luxury but a necessity.

REFERENCES

1. Louis Cartz, *Nondestructive Testing*, ASM International, 1995

2. M. Sadiku, *Elements of Electromagnetics*, 2nd ed., Oxford University Press, 1995.

3. C. Balanis, *Advanced Engineering Electromagnetics*, John Wiley & Sons, 1989

4. J. Lameraner and M. Stafl, *Eddy Currents*, Ilife, London, 1968

5. R. Stoll, *The Analysis of Eddy Currents*, Clarendon Press, Oxford, 1974

6. J. Tegopoulos and M. Kriezis, *Eddy Currents in Linear Conducting Media*, Elsevier, Amsterdam, 1985

7. W. Muller, "A New Iteration Technique for Solving Stationary Eddy Current Problem Using the Method of Finite Difference, " *IEEE Trans. Magn.*, Vol. 18, 1982, 588-593

8. S. Wiak and K. Zakrzewski, "Numerical Calculation of Transients in Electrical Circuits with Nonlinear Eddy Current Skin Effect" *IEE Proceedings*, Vol. 134, Part A, 1987, 741-746

9. M. Chari, "Finite Element Solution of the Eddy Current Problem in Magnetic Structures," *IEEE Trans. Power App. Syst.*, Vol. 93, 1974, 62-72

10. C. Carpenter, "Finite Element Models and Their Application to the Eddy Current Problems," *Proc. Inst. Elec. Eng.*, Vol. 122, 1975, 455-462

11. P. Silvester and R. Ferrari, *Finite Elements for Electrical Engineers*, Cambridge University Press, 1970

12. A. Bossavit and J. C. Verite, "A Fixed FEM-BIEM Method to Solve 3D Eddy Current Problems," *IEEE Trans. Magn.*, Vol. 18, No. 2, 1982, 431-437

13. S. Salon and J. Peng, "3-D Eddy Current Using a Four Component Finite Element Formulation," *IEEE Trans. Magn.*, Vol. 20, 1984, 1992-1994

14. T. Preston and A. Reece, "Solution of 3-Dimensional Eddy Current Problems: The T-Ω Method", *IEEE Trans. on Magnetics*, Vol. 18, No. 2, 1982, 486-491

15. D. Rodger and A. Eastham, "A Formulation for Low Frequency Eddy Current Solutions" *IEEE Trans. Magn.*, Vol.19, No. 6, 1983, 2443-2446

16. P. Leonard and D. Rodger, "Finite Element Scheme For Transient 3D Eddy Currents", *IEEE Trans. on Magnetics*, Vol. 24, No. 1, 1988, 90-93

17. C. Biddlecombe, E. Heighwar, J. Simkin, and C. Trowbridge, "Methods For Eddy Current Computation in Three Dimensions", *IEEE Trans. On Magnetics*, Vol. 18, No. 2, 1982, 492-497

18. C. Emson and J. Simkin, "An Optimal Method For 3D Eddy Currents", IEEE Trans. On Magnetics, Vol. 19, No. 6, 1983, 2450-2452

19. O. Biro and K. Preis, "Finite Element Analysis of 3-D Eddy Currents," *IEEE Trans. Magn.*, Vol. 26, 1990, 418-423

20. Z. Ren, F. Bouillault, A. Pazek, A. Bossavit, and J. Verite, "A New Hybrid Model Using Electric Field Formulation for 3-D Eddy Current Problems," *IEEE Trans. Magn.*, Vol. 26, 1990, 470-473

21. Z. Ren and A. Razek, "New Technique for Solving 3-D Multiply Connected Eddy Current Problems," *Proc. Inst. Elec. Eng.*, Pt. A, Vol. 137, No.3, 1990, 135-140

22. S. Wong and Z. Cendes, "Combined Finite Element Modal Solution of 3-D Eddy Current Problems," *IEEE Trans. Magn.*, Vol. 24, 1988, 2685-2687

23. S. Wong and Z. Cendes, "Numerical Stable Finite Element Methods for the Galerkin Solution of Eddy Current Problems," *IEEE Trans. Magn.*, Vol. 25, 1989, 3019-3021

24. R. Albanese and G. Rubinacci, "Finite Element Methods for the Solution of 3D Eddy Current Problems", *Advances in Imaging and Electron Physics*, Vol. 102, pp.1-86, 1997

25. A. Kameari, "Three Dimensional Eddy Current Calculation Using Finite Element Method With A-V in Conductor and Ω in Vacuum", *IEEE Trans. on Magnetics*, Vol. 24, No.1, 1988, 118-121

26. A. Kameari, "Calculation of Transient 3-D Eddy Currents Using Edge Elements," *IEEE Trans. Magn.*, Vol. 26, 1990, 466-469

27. T. Nakata, N. Takahashi, K. Fujiwara, and Y. Okada, "Improvements of the T-Ω Method for 3-D Eddy Current Analysis," *IEEE Trans. Magn.*, Vol. 24, 1988, 94-97

28. T. Nakata, N. Takahashi, K. Fujiwara, and Y. Shiraki, "Comparison of Different Finite Elements for 3-D Eddy Current Analysis," *IEEE Trans. Magn.*, Vol. 26, 1990, 434-437

29. J. Salon and J. Schneider, "A Comparison of Boundary Integral and Finite Element Formulations of the Eddy Current Problems," *IEEE Trans. Power App. Syst.*, Vol. 100, 1981, 1473-1479

30. A. Kost, "Calculation of Three-Dimensional Nonlinear Eddy Currents in an Electrical Machine by the Boundary Element Method," in *Boundary Element Techniques: Application in Engineering.* (ed. C. Brebbia and N. Zamani), Computational Mechanic Publication, Southampton.

31. W. Rucker and K. Richter, "A BEM Code for 3-D Eddy Current Calculations," *IEEE Trans. Magn.*, Vol. 26, 1990, 462-465

32. H. Tsuboi and T. Misaki, "Three Dimensional Analysis of Eddy Current Distribution by the Boundary Element Method," *IEEE Trans. Magn.*, Vol. 23, 1987, 3044-3046

33. S. Salon and J. Schneider, "A Hybrid Finite Element Boundary Integral Formulation of the Eddy Current Problem," *IEEE Trans. Magn.*, Vol. 18, 1982, 461-464

34. E. Kriezis, T. Tsiboukis, S. Panas, and J. Tegopoulos, "Eddy Currents: Theory and Applications," *Proc. IEEE*, Vol. 80, 1992, 1559-1589

35. H. Hrenikoff, "Solution of Problems in Elasticity by the Framework Method," Journal of Applied Mechanics, *Trans. ASME*, Vol. 8, 1941, 169-175

36. R. Courant, "Variational Methods for the Solution of Problems of Equilibrium and Vibration," *Bulletin of the American Mathematical Society*, Vol. 49, 1943, 1-43

37. D. McHenry, "A Lattice Analogy for the Solution of Plane Stress Problems," *Journal of the Institute of Civil Engineering*, Vol. 21, 1943, 59-82

38. S. Levy, "Structural Analysis and Influence Coefficients for Dalta Wings," *Journal of Aeronautical Sciences*, Vol. 20, 1953, 449-454

39. R. Clough, "The Finite Element Method in Plane Stress Analysis," *Proceedings of the American Society of Civil Engineering*, Vol. 87, 1960, 345-378

40. M. Burrows, *Theory of Eddy Current Flaw Detection*, Ph.D. Dissertation, University of Michigan, 1964

41. C. Dodd and W. Deeds, "Analytical Solutions to Eddy Current Probe-Coil Problems," *Journal of Applied Physics*, Vol. 39, 1968, 2829

42. W. Lord and R. Palanisamy, "Development of Theoretical Models for Nondestructive Testing Eddy Current Phenomenon," in *Eddy Current Characterization of Materials and Structures*, ASTM STP-722, G. Birnbaum and G. Free Eds., 1981, 5-21

43. R. Palanisamy and W. Lord, "Finite Element Modeling of Electromagnetic NDT Phenomenon," *IEEE Trans. Magn.*, Vol. 15, 1979, 1479-1481

44. R. Palanisamy and W. Lord, "Prediction of Eddy Current Probe Signal Trajectories," *IEEE Trans. Magn.*, Vol. 16, 1980, 1083-1085

45. T. Nehl and N. Demerdash, "Application of Finite Element Eddy Current Analysis To Nondestructive Detection of Flaws in Metallic Structures," *IEEE Trans. Magn.*, Vol. 16, 1980, 1080-1082

46. S. Hoole, "Artificial Neural Networks in the Solution of Inverse Electromagnetic Field Problems," *IEEE Trans. Magn.*, Vol. 29, 1993, 1931-1934

47. L. Udpa and S. Udpa, "Application of Signal Processing and Pattern Recognition Techniques to Inverse Problems in NDE," *International Journal of Applied Electromagnetics and Mechanics*, Vol. 8, 1997, 99-117

48. Z. Badics, Y. Matsumoto, S. Kojima, Y. Usui, K. Aoki, F. Nakayasu, "Rapid Flaw Reconstruction Scheme for Three-Dimensional Inverse Problems in Eddy Current NDE," in *Electromagnetic Nondestructive Evaluation*, T. Takagi et al. eds., IOS Press, 1997, 303-309

49. R. Popa and K. Miya, "A Data Processing and Neural Network Approach for Inverse Problems in ECT," in *Electromagnetic Nondestructive Evaluation (II)*, R. Albanese et al. eds., IOS Press, 1998, 297-305

128

50. R. Sikora, T. Chady, and J. Sikora, "Neural Network Approach to Crack Identification," *International Journal of Applied Electromagnetics and Mechanics*, Vol. 9, 1997, 391-398

51. G. Rubinacci, A. Tamburrino, S. Ventre, and F. Villone, "Reconstruction of Interacting Cracks in Conductive Materials by a Communicative Theory Approach," in *Electromagnetic Nondestructive Evaluation (IV)*, S. Udpa et al. eds., IOS Press, 2000, 151-158

52. D. Ioan and A. Duca, "Use of MTANN Systems to Solve Inverse ENDE Problems," in *Electromagnetic Nondestructive Evaluation (IV)*, S. Udpa et al. eds., IOS Press, 2000, 159-166

53. M. Oristaglio and M. Worthington, "Inversion of Surface and Borehole Electromagnetic Data for 2D Electrical Conductivity Model", *Geophysical Prospecting*, Vol. 28, 1980, 633

54. S. Salon and B. Istfan, "Inverse Nonlinear Finite Element Problems," *IEEE Trans. Magn.*, Vol. 22, 1986, 817-818

55. S. Hoole, S. Subramaniam, R. Saldanha, and J. Coulomb, "Inverse Problem Methoddology and Finite Elements in the Identification of Cracks, Sources, Materials, and their Geomtry in Inaccessible Locations", *IEEE Trans. on Magnetics*, Vol. 27, No.3, 1991, 3433-3443

56. S. Norton and J. Bowler, "Theory of ECT Inversion," *Journal of Applied Physics*, Vol. 73, 1993, 501

57. J. Bowler, "Inversion of Eddy Current Data to Reconstruct Flaws by an Optimization Process," *International Journal of Applied Electromagnetics and Mechanics*, Vol. 4, 1994, 277-284

58. P. Neittaanmaki, M. Rudnicki, and A. Savini, *Inverse Problems and Optimal Design in Electricity and Magnetism*, Oxford University Press, 1996

59. M. Yan, M. Afzal, S. Udpa, S. Mandayam, Y. Sun, L. Udpa and P. Sacks, "Iterative Algorithms for Electromagnetic NDE Signal Inversion", in *Electromagnetic Nondestructive Evaluation (II)*, R. Albanese et al. eds., IOS Press, 1998, 287-296

60. G. Liu, Y. Li, Y. Sun, P. Sacks, and S. Udpa, "An Iterative Algorithm For Eddy Current Signal Inversion", *Review of Progress in Quantitative Nondestructive Evaluation*, Vol. 19A, 2000, 497-504

61. R. Albanese, G. Rubinacci, and F. Villone, "An Integral Computational Model for Crack Simulation and Detection via Eddy Currents", *Journal of Computational Physics*, Vol. 152, 1999, 736-755

62. J. P. Webb, "Edge Elements and What They Can Do for You", *IEEE Trans. on Magnetics*, Vol. 29, No. 2, 1993, 1460-1465

63. K. H. Ng, *Eddy Current NDE Signal Inversion*, Master's Thesis, Iowa State University, 1999

64. M. Gunzburger, "Adjoint equation based methods for control problems in incompressible viscous flows". *Design Optimal et MDO*, Centre de Recherche en Calcul Applique, Montreal, 1998, 1-25.

65. J. C. Nedlec, "Mixed Finite Elements in R^3", *Numer. Math.*, Vol. 35, 1980, 315-334

66. A. Bossavit, "A Rationale For Edge Elements", *IEEE Trans. on Magnetics*, Vol. 24, No. 1, 1988, 74-79

67. A. Kameari, "Three Dimensional Eddy Current Calculation Using Edge Elements for Magnetic Vector Potential", *Applied Electromagnetics in Materials*, Pergamon Press, 1986, 225-236

68. R. Albanese and G. Rubinacci, "Magnetostatic Field Computations In Terms Of Two Component Vector Potentials", *International Journal For Numerical Methods In Engineering*, Vol. 29, 1990, 515-532

69. R. Albanese and G. Rubinacci, "Analysis of Three-Dimensional Electromagnetic Fields Using Edge Elements", *Journal of Computational Physics*, Vol. 108, 1993, 236-245

70. V. Isakov, "Uniqueness and Stability in Multi-Dimensional Inverse Problems", *Inverse Problems*, Vol. 12, 1996, 267-278

71. F. Kojima, "Computational Method for Crack Shape Reconstruction Using Hybrid FEM-BEM Scheme Based on A-Φ Method", in *Electromagnetic Nondestructive Evaluation, (I)*, IOS Press, 1997, 279-286

72. H. Fukutomi, T. Takagi, J. Tani, and F. Kojima, "Crack Shape Characterization in Eddy Current Testing", in *Electromagnetic Nondestructive Evaluation (II)*, IOS Press, 1998, 305-312

73. P. Silvester and R. Ferrari, *Finite Elements for Electrical Engineers*, 3rd ed., Cambridge University Press, 1996

74. J. Jin, *The Finite Element Method in Electromagnetics*, Jon Wiley & Sons, 1993

75. K. Huebner and E. Thornton, *The Finite Element Method for Engineers*, 2nd ed., John Wiley & Sons, 1982

76. W. Bickford, *A First Course in The Finite Element Method*, Richard D. Irwin INC., 1994

77. A. George and J. Liu, *Computer Solution of Large Sparse Definite Systems*, Prentice-Hall, 1981

78. Y. Saad, *Iterative Methods for Sparse Linear Systems*, PWS Publishing Company, 1996

79. C. F. Gerald and P. O. Wheatley, *Applied Numerical Analysis*, Addison-Wesley Publishing Company, 1994

80. J. S. Van Welij, "Calculation of Eddy Current in terms of H on Hexahedron", *IEEE Trans. on Magnetics*, Vol. 21, 1985, 2239-2241

81. A. Gibbons, *Algorithmic Graph Theory*, Cambridge University Press, 1985

82. H. W. Hale, "A Logic for Identifying the Trees of A Graph", *Tran. AIEE (Power Apparatus and Systems)*, Vol. 80, 195-198

83. T. Takagi et al., "Benchmark Models of Eddy Current Testing for Steam Generator Tube: Experiment and Numerical Analysis", *International Journal of Applied Electromagnetics and Materials*, Vol. 5, 1994, 149-162

84. T. Takagi et al., "ECT Research Activities in JSAEM – Benchmark Models of Eddy Current Testing for Steam Generator Tube – (Part 1)", *Nondestructive Testing of Materials*, R. Collins et al. (Eds.), IOS Press, 1995, 253-264

85. Y. Harada, E. Okano, and R. Murakami, "3D Benchmark Models and Experiment of Eddy Current Testing", *Journal of Japan Society of Applied Electromagnetics*, Vol. 3, 1995, 91-100

86. M. Angeli, P. Burrascano, E. Cardelli, S. Resteghini, and R. Sikora, "Numerical Analysis of Eddy Current Nondestructive Testing (JSAEM Benchmark Problem #1 – Circular Plate) ", in *Electromagnetic Nondestructive Evaluation (II)*, R. Albanese et al. eds., IOS Press, 1998, 331-336

87. T. Takagi and H. Fukutomi, "Benchmark Activities of Eddy Current Testing for Steam Generator Tubes", in *Electromagnetic Nondestructive Evaluation (IV)*, S. Udpa et al. eds, IOS Press, 2000, 235-252

88. J. E. Dennis Jr. and R. B. Schnabel, *Numerical Methods For Unconstrained Optimization and Nonlinear Equations*, 194-217, Prentice-Hall, 1983

89. A. S. Housholder, *The Theory of Matrix in Numerical Analysis*, Dover, New York, 1975

ACKNOWLEDGEMENTS